Striosomes Target Nigral Dopamine-Containing Neurons via Direct-D1 and Indirect-D2 Pathways Paralleling Classic Direct-Indirect Basal Ganglia Systems

Iakovos Lazaridis[1*], Jill R. Crittenden[1], Gun Ahn[1], Kojiro Hirokane[1], Tomoko Yoshida[1], Ara Mahar[1], Vasiliki Skara[2], Konstantinos Meletis[2], Johnny H. Loftus[1], Krishna Parvataneni[1], Jonathan T. Ting[3,4], Emily Hueske[1], Ayano Matsushima[1], Ann M. Graybiel[1*]

[1]McGovern Institute for Brain Research and Department of Brain and Cognitive Sciences, Massachusetts Institute of Technology, Cambridge, MA 02139, USA
[2]Karolinska Institutet, Stockholm, SE
[3]Human Cell Types Dept, Allen Institute for Brain Science, Seattle WA 98109, USA
[4]Department of Physiology and Biophysics, University of Washington, Seattle WA 98195, USA
*Correspondence: graybiel@mit.edu and iaklaz@mit.edu

Acknowledgements

We thank Samitha Venu and the Swanson Biotechnology Center at the MIT Koch Institute for expert assistance in generating the N172 mouse line; Ximena OptizAraya for cloning of enhancer AAV vectors; Allen Institute Viral Core team for enhancer AAV virus production; Bargavi Thyagarajan for Allen Institute project management support. This research was supported by NIH/NIMH R01 MH060379 (AMG), NIH/NIMH P50 MH119467 (AMG), the Saks-Kavanaugh Foundation (AMG), the William N and Bernice, E. Bumpus Foundation (AMG, AM), the Hock E. Tan and K. Lisa Yang Center for Autism Research (AMG), Mr. Robert Buxton, the Simons Foundation grant to the Simons Center for the Social Brain at MIT (AMG), the CHDI Foundation (AMG), Jim & Joan Schattinger (AMG), Ellen Schapiro & Gerald Axelbaum Investigator BBRF Young Investigator Grant (IL), and NIH BRAIN Armamentarium Grant UF1MH128339 (JTT).

Author Contributions

JRC and AMG conceived and designed the initial experiments demonstrating anatomically the striosomal direct and indirect pathways; IL designed and implemented the rabies experiments and demonstrated the throughput from S-D2 cells to cGPe to SNpc; JRC, TY, IL, ArM and JHL collected anatomical data; IL, JRC, EH, TY, ArM and AMG performed image analysis interpretation and cell counting; IL, ArM collected behavioral and functional data; IL, GA, KH, KP performed behavioral and signal analysis; GA developed and employed analytic pipelines and used multiple models to analyze the functional data in relation to the neural data; GA and IL

performed the statistical analyses; KM, JTT designed and generated viral reagents; JRC and AMG wrote the initial draft and AMG and IL wrote the full draft with edits by EH, AyM, and JRC.

HIGHLIGHTS

- Direct-D1 and Indirect-D2 striosomal pathways (S-D1, S-D2) target SNpc dopamine cells
- The S-D2 circuit targets a distinct central zone of the external pallidum (cGPe)
- Stimulation of S-D2 increases, of S-D1 decreases, striatal dopamine and movement
- Activity of S-D1 increases, of S-D2 decreases, at outcome; S-D1 activity brackets task

ABSTRACT

The classic output pathways of the basal ganglia are known as the direct-D1 and indirect-D2, or "Go/No-Go", pathways. Balance of the activity in these canonical direct-indirect pathways is considered a core requirement for normal movement control, and their imbalance is a major etiologic factor in movement disorders including Parkinson's disease. We present evidence for a conceptually equivalent parallel system of direct-D1 and indirect-D2 pathways that arise from striatal projection neurons (SPNs) of the striosome compartment rather than from the matrix. These striosomal direct (S-D1) and indirect (S-D2) pathways, as a pair, target dopamine-containing neurons of the substantia nigra (SNpc) instead of the motor output nuclei of the basal ganglia. The novel anatomically and functionally distinct indirect-D2 striosomal pathway targets dopaminergic SNpc cells indirectly via a core region of the external pallidum (GPe). We demonstrate that these S-D1 and S-D2 pathways oppositely modulate striatal dopamine release in freely behaving mice under open-field conditions and oppositely modulate locomotor and other movements. These S-D1 and S-D2 pathways further exhibit different, time-dependent responses during performance of a probabilistic decision-making maze task and respond differently to rewarding and aversive stimuli. These contrasts depend on mediolateral and anteroposterior striatal locations of the SPNs as are the classic direct and indirect pathways. The effects of S-D1 and S-D2 stimulation on striatal dopamine release and voluntary locomotion are nearly opposite. The parallelism of the direct-indirect circuit design motifs of the striosomal S-D and S-D2 circuits and canonical matrix M-D1 and M-D2, and their contrasting behavioral effects, call for a major reformulation of the classic direct-indirect pathway model of basal ganglia function. Given that some striosomes receive limbic and association cortical inputs, the S-D1 and S-D2 circuits likely influence motivation for action and behavioral learning, complementing and possibly reorienting the motoric activities of the canonical matrix pathways. At a fundamental level, these findings

suggest a unifying framework for aligning two sets of circuits that share the organizational motif of opponent D1 and D2 regulation, but that have different outputs and can even have opposite polarities in their targets and effects, albeit conditioned by striatal topography. Our findings further delineate a potentially therapeutically important set of pathways influencing dopamine, including a D2 receptor-linked S-D2 pathway likely unknowingly targeted by administration of many therapeutic drugs including those for Parkinson's disease. The novel parallel pathway model that we propose here could help to account for the normally integrated modulatory influence of the basal ganglia on motivation for actions as well as the actions themselves.

INTRODUCTION

The striatum, the largest nucleus of the basal ganglia, powerfully modulates movement and mood under normal conditions and enables reinforcement-driven plasticity to shape behavior. Massive loss of striatal dopamine occurs in Parkinson's disease, and massive degeneration of striatal projection neurons (SPNs) occurs in Huntington's disease. Thus, the striatum and its output pathways are a central focus in attempts to combat these and related basal ganglia disorders, and increasingly to combat neuropsychiatric conditions. Under normal conditions, the neural modulation of mood and movement by the basal ganglia is thought to be the result of a push-pull control system deploying opposing yet coordinated interactions between two canonical basal ganglia pathways originating in the striatal SPNs [1–8]. These classic circuits, the so-called direct and indirect pathways, target the basal ganglia output nuclei either monosynaptically (the direct pathway) or via intermediary connectivity (the indirect pathway). In the simplest formulation of the direct-indirect model, dopamine increases direct pathway "Go" activity via D1 dopamine receptors expressed on direct-pathway SPNs in the striatal matrix and decreases "No-Go" activity of the indirect pathway via D2 dopamine receptors on indirect-pathway SPNs in the matrix. These actions of the receptors are referable to their opposite regulation of intracellular pathways [9–11]. As a result, the circuits can favor or impede intended movements, including promoting one intended movement sequence while inhibiting others [6,12–15]. In the classic model, the direct and indirect pathways arise from different ensembles of direct-pathway and indirect-pathway SPNs, they target different output nuclei (pallidal segments and substantia nigra), and they, in turn, differentially influence effector circuits that ultimately modulate cortical, brainstem and spinal processing for movement control. Important amendments to this model allow for cooperative direct-indirect pathway operation, and for extensive collateral pathway crosstalk and other neuromodulatory and oscillatory effects [8,16–22]; but the direct-indirect model has been the cornerstone of clinical and basic science fields alike for nearly half a century.

An outlier in this model has been the strong output of some SPNs to the dopamine-containing neurons of the substantia nigra pars compacta (SNpc)—the very origin of the nigrostriatal tract that severely degenerates in Parkinson's disease. These SPNs mainly, though not exclusively, lie in the so-called striosomes of the striatum. Striosomes are neurochemically distinct macroscopic compartments of the striatum distributed through much of the large extra-striosomal matrix from which the classical direct-indirect pathways arise. Despite the potential power of this striatonigral feedback circuit as a regulator of dopamine neuron activity, and despite the prominence of striosomes in the human striatum, as originally demonstrated [23], the striosomal pathway has never been integrated into the canonical view of the direct and indirect pathways other than that it arises from D1-expressing SPNs. Nor has it been fully characterized.

Here we demonstrate that striosomes not only give rise to a direct D1 pathway to the SNpc, but also to an indirect pathway originating in D2-expressing striosomal SPNs that target a central, largely overlooked subdivision of the external pallidum (GPe) that itself innervates nigral dopamine-containing neurons. This discovery suggests that the classic motor output pathways of the basal ganglia have twins emerging from striosomes that can affect the activity of the dopamine-containing nigral neurons that, in turn, modulate mood and movement through their actions on intraneuronal circuits, on inputs from the neocortex and striatum, and on circuits exiting from the SPNs themselves. We used and engineered multiple transgenic mouse lines, employed rabies viral tracing, optogenetics and novel striosome- and matrix-preferring ATAC-seq-based enhancers in experiments to examine these pathways.

We demonstrate, first, an anatomical double dissociation between the striosomal direct (S-D1) and indirect (S-D2) pathways and the classic direct (M-D1) and indirect (M-D2) pathways of the matrix (M). By simultaneous monitoring of ensemble striatal activity and dopamine release, and by selective optogenetic manipulation of striosomal D1 and D2 SPNs in engineered mice, we further demonstrate that these identified S-D1 and S-D2 striosomal pathways are also functionally dissociable, even opposite, both in their effects on dopamine release in the striatum and on their differential encoding of behaviors involving self-initiated, value-based decision-making, motivation and engagement.

These effects of the S-D1 and S-D2 circuits on striatal dopamine release and locomotor behavior appear to be opposite to those of the classic direct D1 and indirectly D2 pathways insofar as we have tested for them, with the S-D2 circuit promoting locomotion and the S-D1 pathway reducing such movements. These findings call for a deep revision of the classic model of basal ganglia function, wherein these and other effects of the striosomal circuits can be incorporated.

Our findings suggest a parallel between basal ganglia pathways that share the motif of direct and indirect output components, yet radically differ in their targets and potential effects on behavior, with the classic pathways targeting motor pallidal and nigral output nuclei of the basal ganglia, and the striosomal pathways targeting the nigral dopamine system. We suggest that the fundamental parallelism of the direct and indirect striosomal and matrix circuits is likely to underlie equally fundamental differences in their parallel functions in motivation and movement control across states of health and illness.

RESULTS

Striosomes and matrix have different projections to the substantia nigra

We began by using retrograde rabies tracing to compare the projections of the striosomes and matrix, based on prior evidence that striosomes, and specifically the D-1 expressing striosomes, project to the dopamine-containing SNpc, whereas the matrix projects primarily to the substantia nigra pars reticulata (SNpr). We used PV-Cre mice for tracing presumptive connections to the SNpr (**Figure 1, Supplementary Figure 1**; caudoputamen (CP): n = 1434 neurons, 12 sections, 3 PV-Cre mice; GPe: n = 305 neurons, 11 sections, 3 PV-Cre mice), and DAT-Cre mice (**Figure 2, Supplementary Figure 2**; CP: n = 1544 neurons, 15 sections, 4 DAT-Cre mice; GPe: n = 658 neurons, 6 sections, 3 DAT-Cre mice) for tracking presumptive striosomal connections.

GPe projection neurons have multiple targets including the SNpr, SNpc, endopeduncular nucleus, subthalamic nucleus, striatum and cerebral cortex [24–29]. Of these, we focused on a selective trans-neuronal rabies labeling method [30]) to examine the distribution of GPe neurons that target either the dopamine-containing neurons of the SNpc (**Figure 2, Supplementary Figure 2**) or the output neurons of the SNpr, which are known to express parvalbumin (PV) (**Figure 1, Supplementary Figure 1**). In the same brains, we analyzed distributions of the rabies-labeled cells within striosome or matrix compartments.

We injected Cre-dependent rabies helper viruses [30–32] into the SNpc of DAT-Cre or SNpr of PV-Cre transgenic mice (**Table 1**) and then 21 days later injected EnvA-pseudotyped rabies virus (RVΔG-EGFP or RVΔG-mCherry) at the sites of helper-virus injection to produce EGFP- or mCherry-expressing rabies in 'starter neurons' that could retrogradely spread the virus to their presynaptic partners [30–32]. One week after the rabies injections, we prepared the brains for histology.

In the DAT-Cre mice, engineered to have Cre expression in dopamine-containing nigral neurons, we found that rabies-expressing retrogradely labeled neurons were enriched in striosomes within the striatum (**Figure 2B, D and F**) and even more sharply so within a central

zone of GPe (**Figure 2B, E and F**). This zone corresponded to the same central GPe region that we found to receive inputs from striosomal SPNs and that could be defined as a MOR1-rich/CDGI-poor GPe zone (**Figure 2E**).

In the PV-Cre mice, with selective retrograde viral tracing from the PV-positive SNpr neurons, we found a complementary distribution of labeled SPNs both in the striatum, and in the GPe (**Figure 1, Supplementary Figure 1**). In the striatum, the retrogradely labeled SPNs targeting SNpr were largely distributed in the extra-striosomal matrix, mainly avoiding the striosomes (**Figure 1B, D and F, Supplementary Figure 1**); and within the GPe, they were distributed largely in the MOR1-poor/CDGI-rich outer peripheral zone of the GPe (pGPe) (**Figure 1E and F, Supplementary Figure 1**)—the same territory receiving projections from the matrix (**Supplementary Figure 3**). These patterns of connectivity suggest that there are S-D1 SPNs that preferentially target dopamine-containing neurons in the SNpc but have relatively minimal synaptic contact with PV neurons of the SNpr as detected by the transneuronal viral method that we used. These visual impressions were confirmed by cell counts: in the PV-Cre mice, fewer than 10% of the retrogradely labeled striatal SPNs appeared in striosomes, and fewer than 20% in the central part of the GPe (**Figure 1F**). In the DAT-Cre mice, however, in which the inputs to the dopamine-containing SNpc were assessed, most striatal neurons labeled were in striosomes in a topographically distributed dorsal region (nearly 80 %), and within the GPe, the labeled neurons were concentrated in the core of the GPe (~80%), leaving its peripheral zones only sparsely labeled (**Figure 2F**).

These anatomical experiments confirmed a strong distinction between the striosomal and matrix projection patterns in the SNpc and SNpr, and further demonstrated an equally sharp distinction between a central core of the GPe (here called the cGPe) that projects to the dopamine-containing SNpc and a peripheral surrounding part of the GPe (here called the pGPe) that projects to the PV-expressing nigral neurons of the SNpr. The cGPe defined by our experiments resembles the GPe zone noted in previous anatomical work [33,34]. A GPe-to-SNpc connection has been demonstrated electrophysiologically, without specification of its topographic origins within GPe [35,36]. The clarity of the GPe core-periphery distinction found here and in these previous studies is particularly notable given the high degree of collateralization of striatal projections to the GPe [7,21,25,29,37–41].

Identification of S-D1 and S-D2 striatal output pathways by the use of engineered mouse lines

We and others have shown that both D1 and D2 receptor-expressing SPNs lie in striosomes, with different gradients of topographic expression to be present in striosomes [42] (**Supplementary**

Figure 4A-D). We therefore searched for mouse lines that could selectively label either the S-D1 or S-D2 striosomal populations.

We identified four lines of mice with striosome-enriched fluorophore expression, and one line with matrix-enriched fluorophore expression (**Table 1**). We verified the compartmentally biased labeling in three of the lines: striosomal MOR1-mCherry, matrix CalDAG-GEFI-GFP (**Supplementary Figure 3A and B, Supplementary Figure 5**) and striosomal P172-mCitrine (**Supplementary Figure 3D, Supplementary Figure 6**) [42–45]. We further showed striosome enrichment for two additional lines: AT1-tdTomato lines 14 and F, a newly generated transgenic line carrying a partial BAC for AT1 (angiotensin II receptor type 1) (**Supplementary Figure 3C** and 7 Fi line), and a prepronociceptin-Cre line (Pnoc-Cre) developed by Bruchas and colleagues [46] (**Figure 3A, C and E, Supplementary Figure 4**) [158]. Finally, we found enriched striosomal expression in a neurotensin-Cre line (Nts-Cre) when crossed with a Cre-dependent tdTomato reporter line (Ai14) [47,48] (**Figure 3B, D and E, Supplementary Figure 8**).

We tested whether the SPN transgene reporters in these lines were expressed in D1 and D2 SPNs in the striosomes by generating double-transgenic mice with either D1 or D2 BAC reporter mouse lines and then counted single- and double-labeled SPNs at anterior, mid-level and posterior sections through the striatum (**Supplementary Figure 4**). The P172-mCitrine and AT1-tdTomato lines drove reporter expression in both D1 and D2 sSPNs, Pnoc-Cre and MOR1-mCherry labeled D1 SPNs, and a single line, the Nts-Cre;Ai14 reporter cross, drove expression selectively in D2 SPNs with striosome-enrichment. For completeness, we re-examined the matrix immunomarker CalDAG-GEFI, already known to be expressed in both D1 and D2 SPNs [49,50] as was GFP in the CalDAG-GEFI-GFP BAC line [51]. Finally, we tested for each line whether the main striosomal projection to the SN was to the SNpc, a hallmark characteristic of S-D1 cells. The overwhelming evidence from this survey was that S-D1 and S-D2 SPNs can be distinguished in varying topographic, gradient distributions within the striatum.

Of the striosome-enriched lines, the Pnoc-Cre line (**Figure 3A, C and E, Supplementary Figure 4K-Q**) was the most selective and complete in marking striosomes, and we used this line for functional studies. For the S-D2 identification, the D2-selective expression of the Nts-Cre line was a crucial finding for much of this work, as it was the sole S-D2 reporter line. For both Pnoc-Cre and Nts-Cre lines, we generated crosses with a LSL-FlpO mouse line[153] (Pnoc;Flp and Nts;Flp respectively) to confer stable recombinase (Flp) expression in adulthood as both lines are suspected or confirmed to have greater expression during development. We also used these Cre lines in combination with the Ai14 tdTomato reporter mouse line to confer stable tdTomato expression in Pnoc and Nts populations. The Nts-Cre;Ai14-positive SPNs were vividly clustered

in striosomes, but were also scattered through a crescent-shaped dorso-anterior region of what appeared to be matrix but which overlapped the calbindin-poor extra-striosomal zone [52] and Aldh1a1/Anxa1-positive fiber rich zone,[53,54] previously reported, and shown here in **Figure 3B, D** and **E** and **Supplementary Figure 8**. These dispersed Nts-targeted SPNs appeared to comprise a small minority of SPNs in the crescent, which we deem to be is a neurochemically specialized region of the mouse striatum, given its overlap with the Aldh1A1-rich, calbindin-poor dorsolateral zones previously noted [53–55]. These two characteristics, calbindin-negativity and Aldh1A1-positivity, mark this region as potentially having characteristics of striosomes though lacking the clustered architecture. This zone may correspond in part to the so called 'compartment-free space' of Miyamoto and colleagues [56].

We further asked whether the Nts-Cre;Ai14 line, despite its apparent D2 selectivity, nevertheless exhibited the D1 property of projecting to the striosome-dendron bouquets of the ventral SNpc, a hallmark of D1 SPNs [42]. It did not (**Figure 3E**) and there was a clear double dissociation between the reporter lines with expression in S-D1 SPNs and the Nts-Cre;Ai14 (S-D2)-expressing line. All lines with D1 expression exhibited typical entwinement of their axonal terminals with the dendrites of the dopaminergic bouquet dendrons, whereas in the Nts;Ai14 line, there was no fluorophore labeling of axons within the striosome-dendron bouquets (**Figure 3D**, see **Figure 3C** for comparison to Pnoc).

These findings with seven differential markers of striosomal and matrix SPNs (**Table 1**) compared to findings with the more global markers for D1 and D2 SPNs indicate that striosomal SPNs selectively target a central zone of the GPe that is largely avoided by the classical matrix SPN axons.

Striosomal SPNs target cGPe neurons that themselves target dopamine-containing nigral neurons

To further probe the possibility that there is direct connectivity from striosomes to the cells in cGPe that project to the SNpc, we labeled striosomal input fibers within GPe by their expression of N172, which labels both D1 and D2 striosomal neurons but is a strong marker of dorsal striosomes, in combination with RV tracing of SNpc dopamine neurons in DAT-Cre/N172-tdTomato mice. This protocol resulted in rabies-expressing SNpc-DA-targeting GPe neurons being in close proximity to striosomal N172-labeled striosomal input fibers and putative endings in the cGPe zone (**Figure 4, Supplementary Figure 9**). By then using synaptophysin targeting to synaptic terminals of the SPN inputs to the cGPe (**Figure 4D-F**) combined with the SNpc retrograde rabies tracing, we confirmed this potential synaptic terminal association of the

striosomal inputs and GPe output cells projecting to the SNpc neurons (**Figure 4F**): putative synaptic boutons of N172 striosomal axons were in contact, as seen at light microscopic levels, both with the cell bodies and the proximal dendrites of SNpc-DA-targeting cGPe neurons (**Figure 4F**). Approximately 80% of the N172 buttons, identified by shape and size (Imaris software) and colocalized with synaptophysin, were found in close proximity to RV-labeled dopamine-projecting cell bodies or processes in the cGPe zone. The majority of the synaptophysin-positive N172 terminals were located on the dendrites of the dopamine-projecting neurons, compared to the cell bodies (4 sections from 1 animal, average 228.5 ±52.21 sd N172-positive/SYP-positive/RVnegative dendrites, average 36.75 ±10.72 sd N172-positive/SYP-positive/RV-negative cell bodies).

Rasa3 reporter line highlights cGPe zone

We looked for markers that would label cGPe selectively to facilitate definition of striosome-cGPe connectivity and throughput to the SN. GPe projection neurons have been distinguished according to multiple markers including parvalbumin (PV), somatostatin, Lhx6, Npas1, and FoxP2 [24–29,57–59]. None of these markers, individually, defined a cell type that was differentially enriched in the central GPe (cGPe), nor in the surrounding peripheral region around it (pGPe), according to examination of immunohistochemical labeling for Lhx6 or PV, or by detection of tdTomato reporter in Lhx6-Cre;Ai14, PV-Cre;Ai14 and Npas1-Cre;Ai14 mice. These findings (not illustrated) are consistent with those from comprehensive spatial mapping of these GPe neuronal markers [24–29]. We therefore searched for new genetic markers of GPe cell subtypes in a single-cell sequencing data set [60] and then looked to see whether any of those genes showed differential expression in the central GPe, based on Gensat reporter mice [43]. We made a manual search and identified one GFP reporter, in the Rasa3-GFP BAC transgenic mouse, with strikingly enriched expression in the central GPe (**Supplementary Figure 10A**). These neurons targeted by retrograde tracing experiments in DAT-Cre/N172-tdTomato mice colocalized with Rasa3/Lhx6; and in separate experiments, we found that such neurons were negative for PV (**Supplementary Figure 10B**). We could not, however, use Rasa3 in further experiments, because in the brains of mature mice, what became clear was that Rasa3 detected was actually the reporter of the gene, which had been down-regulated in the GP. Rasa3 3 by this analysis was not selective for the central GPe and was expressed equally in both Lhx6 and PV neurons (**Supplementary Figure 10G and J**). It is likely that the Rasa3-GFP BAC mouse reports genomic control elements that do define the central GPe neurons, but that Rasa3 expression in adults is not itself exclusive to this population. The augmented labeling in the Rasa3-GFP BAC mouse nevertheless provides

evidence that the cGPe harbors a molecularly distinct cell type differentially enriched relative to the surrounding peripheral (pGPe) regions. This could well become important in future experiments on development, as Rasa3 is a transcription factor associated with the immune system [61–63].

Demonstration of novel striatal enhancers preferentially expressed in striosomes or matrix: confirmation of striosomal direct and indirect pathways.

We tested several enhancers developed at the Allen Institute. The most promising of those tested were DLX2.0-SYFP2 and 452h-mTFP1, illustrated in **Supplementary Figure. 13**. DLX2.0-SYFP2 exhibited enhanced expression in striosomes. Cell density analysis indicated a higher density of labeled cells in striosomes than in the matrix (**Supplementary Figure. 13F**). We compared the expression patterns of the striosomal enhancer DLX2.0-SYFP2 and the matrix-specific enhancer 452h-mTFP1 in Nts;Ai14 mice. The striosomal enhancer DLX2.0-SYFP2 showed an overlay of expression with Nts;Ai14 in striosomes (**Supplementary Figure. 13B**). The matrix-specific enhancer 452h-mTFP1 exhibited a distinct expression pattern in the matrix regions relative to the Nts;Ai14 SPNs (**Supplementary Figure. 13C**).

We further investigated the targeted expression in D1 or D2 striosomal SPNs in A2a-Cre mice. Intrastriatal injection of AAV-DLX2.0-minBG-FIPO-WPRE3-BGHpA followed by intersectional viruses (Cre-On/Flp-On-EYFP for striosomal D2 and Cre-Off/Flp-On-mCherry for striosomal D1) resulted in the selective labeling of striosomal D1-SPNs with mCherry (red) and striosomal D2-SPNs with EYFP (green) within the striatum. The axonal projections of both D1 and D2 striosomal neurons highlighted dense terminal zones of S-D2 in the cGPe and the continuation of D1 striosomal neuron axons downstream to the GPi and substantia nigra (**Supplementary Figure. 13D**).

Specific targeting of striosomal D2 SPNs in A2a-Cre mice was confirmed following an injection of the Cre-dependent striosomal enhancer virus DLX2.0-DIO-SYFP2, with green fluorescence marking the expression of the enhancer virus and red immunostaining for MOR1 confirming striosome specificity (**Supplementary Figure. 13E**).

These findings suggest that the enhancers will be highly useful reagents for further work, especially because of the clarity of their differential labeling of the cGPe. Here, they provided important confirmatory evidence for a central region of the cGPe having differentially strong input from the S-D2 pathway and the S-D1 pathway, but far less input from the M-D1 or M-D2 pathways, as detected by our methods.

Interim summary

These multiple sets of experiment demonstrate that, in parallel with the canonical matrix D2 projection to the GPe, the origin of the classical indirect pathway of the basal ganglia, there is a non-canonical S-D2 pathway targeting a GP region embedded in, but separate from, the classical GPe-indirect pathway pallidum. The findings further confirm that the S-D2 indirect pathway innervates the dopamine-containing ventral tier of the SNpc, with no detectable labeling of the SNpr. By contrast, the matrix M-D2 pathway directly targets PV neurons of the SNpr. Thus, we here demonstrate the existence of D1-preferring and D2-preferring striosomal pathways that share the direct-indirect split organization of the canonical pathways, but not their output destinations. Instead, they target the dopamine-containing neurons of the SNpc. We next asked whether we could identify functional characteristics of these S-D1 and S-D2 direct-indirect pathways.

Functional differentiation of the striosomal direct and indirect pathways: *Contrasting effects on striatal dopamine release of the S-D1- and S-D2 enriched populations*

It has not been feasible with previous techniques to record selectively the D2 populations of striosomal neurons in awake behaving animals. Nor has such dual recording been possible with simultaneous recordings of dopamine release. Given our anatomical findings, we attempted to do this by initiating a series of tests based on behavioral performance of engineered mice. We anticipated that, given their targeting of dopamine-containing neurons in the striatum in the SNpc ventral tier, the S-D1 and S-D2 pathways might each have identifiable effects on dopamine release in the striatum.

We recorded striatal dopamine release in 9 Pnoc;Flp (S-D1 proxy) and 11 Nts;Flp (S-D2 proxy) mice as they moved voluntarily within a small open field. One month before testing, we prepared the mice by making injections of Flp-dependent AAV-fDIO-Chrimson and AAV-hsyn-GRAB-DA3h and an optogenetic stimulation fiber placed close by (**Figure 5**) within the mid-mediolateral dorsal caudoputamen (AP = 0.86 mm, ML = 2.0 mm, DV = 2.2 mm). During the free open-field behavior, we applied optogenetic stimulation (8 sec, 40 Hz, 10 trials with randomized inter-trial intervals of ~1.5 min) to stimulate with AAV-fDIO-Chrimson as we recorded dopamine release with DA3h. We measured the lengths of the running trajectories during the 8-sec stimulation periods and the 8-sec periods before and after the stimulation, and we compared the distance traveled and the activity levels during these times as analyzed with DeepLabCut and B-SOID (**Figure 5, Supplementary Figure 12 D and E**).

We stimulated either the putative S-D1 or putative S-D2 populations at randomly chosen times as the mice moved about. The results were consistent across the 9 Pnoc;Flp (**Figure 5A-C**) and 5 Nts;Flp mice with sufficient dopamine sensor signal (**Figure 5G-I**): stimulating the S-D1 (Pnoc;Flp) population decreased dopamine release, whereas stimulating the S-D2 (Nts-Flp) population increased dopamine release.

These recordings gave us clear evidence that the S-D1 and S-D2 pathways had near opposite effects on striatal dopamine release. Moreover, the results indicated that the S-D1 pathway decreased dopamine release, and the S-D2 pathway increased dopamine release, modulations opposite to those expected of the classical direct D1 and indirect pathways. We simultaneously measured locomotor activity during the 8-second pre-stimulation, 8-second during stimulation, and 8-second post-stimulation periods. When the S-D1 proxy Pnoc populations were stimulated, the mice decreased their movement trajectories relative to those during the pre-stimulation period (n = 8 Pnoc;Flp mice, **Figure 5D-F, Supplementary Figure 12 D and E**). When the S-D2 proxy Nts populations were stimulated, large increases in movement occurred (n = 11 Nts;Flp mice, **Figure5 J-L, Supplementary Figure 12 D and E**). These effects of stimulating the S-D1 and S-D2 populations were opposite to the classical effects on movement of the classical D1-direct (Go) and D2-indirect (No-Go) pathways[1,2,6,18].

Behavioral motifs, characterized using the B-SOiD clustering tool, identified twenty unique movement motifs from video recordings of the mice annotated by DeepLabCut. The average frequency of these motifs, calculated in frames per second, showed variable usage between stimulation-on and stimulation-off periods (**Figure 5M-Q**). The analysis of motif usage indicated that a significant shift occurred during stimulation periods compared to off periods, with opposing effects observed between the Pnoc and Nts groups that we interpret as indicating an alteration in behavioral states due to stimulation. With Pnoc-targeted activation, there was a reduction in time spent in mobility, and along an increase in sniffing, rearing and grooming (see motifs 1, 5, and 19 in **Figure 5N**). Conversely, Nts-targeted activation resulted in the opposite effect, increasing mobility and decreasing sniffing, rearing and grooming activities. (**Figure 5M and N**). Kinematic analyses complemented these findings by quantifying head and body twist angular velocities, as well as moving speeds. Both head and body twist velocities, as well as movement speeds, were significantly and differentially modulated by stimulation: stimulation of the Pnoc (proxy S-D1) population decreased both angular velocity and speed, whereas stimulation of the Nts (proxy D-2) population increased these movement parameters (**Figure 5O-Q**). These measurements of the active behavior of the putative S-D1 and S-D2 populations indicate a notable difference in the influence of the S-D1 and S-D2 SPN populations within the caudoputamen.

Dynamics of dopamine release in relation to the activities of S-D1 and S-D2-enriched SPN populations during probabilistic decision-making in a T-maze

We examined striatal neural population activity and dopamine release simultaneously in 5 Pnoc;Flp (proxy S-D1) mice and 6 Nts;Flp (proxy S-D2) mice that performed a well-learned T-maze task requiring them to turn right or left to receive a reward with a 75% probability for arriving at the correct port. No reward was given for an incorrect choice, and there was a 5% chance of receiving an air puff. The rewarded port was switched randomly every 7 to 24 trials, with no signal provided to indicate the change. The mice were implanted and injected bilaterally with optical probes to record striatal dopamine release (DA3h) and AAV-syn_FLEX-jGCaMP8m to record striosomal SPNs' calcium transients as representative of the activity of these SPNs (**Figure 6G**). **Figure 6A and B** illustrates the placement of the optical fibers and the viral injection sites in the mid to medial dorsal striatum, and **Figure 6C-F** show the task and mice performance. The injection sites were medial in the left hemisphere and lateral in the right hemisphere (**Figure 6A and B, Supplementary Figure 11**). As the mice ran the maze task, we found that the levels of dopamine release in both the dorsomedial (DMS) and dorsolateral (DLS) striatum briefly fell at initiation port but then steadily rose to a sharp peak just at the maze turn. Levels then fell to baseline levels at the choice ports and then rose after the choice and during the maze turn in the return to the initiation port (**Figure 6H, Supplementary Figure 12**). Thus, dopamine levels were highest during the runs as the mice accelerated to the turn point and then fell as they ran to the end port. Remarkably, as the strong modulation of dopamine levels occurred in the striatum, sharply different population activities occurred in SPNs of the S-D1 Pnoc-targeted population and the S-D2 Nts-targeted population and, as measured by recording of calcium transients, in the DMS or DLS (**Figure 6H, Supplementary Figure 12**).

In the DMS, the activity of the S-D1 Pnoc population rose at the start, fell to a deep valley of low activity at the turn, rose toward the choice point and reward port, and then fell to baseline levels. The end rise at the choice ports was even larger than the rise at the initiation site (where 5 μl water was given probabilistically, 75% probability in the correct choice port, as opposed to a certain reward (3 μl) with 100% probability, at the initiation port to which the mice were required to return before starting the next trial). Raw traces of the activity of the S-D1 Pnoc-targeted and S-D2 Nts-targeted striatal neurons (**Figure 6H, Supplementary Figure 12**) indicated that the activity of the putative S-D1 cells in the DMS formed a pattern bracketing the beginning and end of the run trajectories (**Figure 6J**), highly reminiscent of the task bracketing pattern that we

originally observed in mice with tetrode recordings in the dorsal striatum of rats, mice and monkeys.

The S-D2 proxy Nts striatal population had a fluctuating fall-rise-fall pattern in the DMS, roughly opposite to the S-D1 proxy Pnoc population patterns at the beginning and end pattern. In the DLS, no such bracketing by the Pnoc population occurred. Instead, both the Pnoc and Nts populations started at very low levels and formed a broad rise and then fell to low levels at goal-reaching similar to the dopamine response (**Figure 6H**) [64].

We performed a cross-correlation analysis between the dopamine release and population activity levels of both Pnoc and Nts mice during the maze task performance to quantify the results (**Figure 6I**). In the DMS, we found that the dopamine fluctuations and Pnoc S-D1 population neuron activity exhibited an anti-correlated pattern. Conversely, in the DLS, the pattern for the Pnoc population was inverted; it showed a positive correlation with dopamine fluctuations, similar to the Nts population. The Nts population in the DMS displayed lateralization effects: there was a positive correlation with dopamine for trials with contralateral turns and a negative correlation for ipsilateral trials.

When we aligned the activity traces of Pnoc, Nts, and dopamine to the entry into the choice port, across rewarded and unrewarded trials, we observed no significant modulation in response to the outcome for either the Pnoc or Nts populations in either the DMS or DLS (**Figure 6K**). This surprising result suggests a lack of selectivity in their outcome/reinforcement response, as their activity at the outcome was nearly identical regardless of reward condition. By contrast, dopamine release levels in the DMS evidenced increased activity in rewarded trials compared to the activity in unrewarded ones, indicating a positive modulation by outcome. Also unexpectedly, in the DLS, both dopamine release levels and Nts population activity were increased (positively modulated) in unrewarded trials. This pattern of activity is better aligned with the timing of port exit rather than the outcome itself, potentially an 'end or try-again signal' or due to the action of exiting the port since animals tended to leave the port more rapidly when no reward was received (**Supplementary Figure 12B**).

We trained classifiers to predict behavior and the outcome of choices. The results of the classification model's performance in predicting various behaviors based on neural activity patterns are presented (**Figure 7A, B**). The confusion matrices in panel A illustrate the model's ability to predict task space behaviors, including initiation, left turn, right turn, left choice, and right choice, across different brain regions (DMS and DLS) and signals (Pnoc SPN activity, Nts SPN activity, and striatal dopamine). Dopamine in the DMS shows significantly higher-than-chance accuracy for initiation and contralateral turn and choice events, while Pnoc and Nts in both DMS

and DLS, and dopamine in DLS show higher-than-chance accuracy for all task events. In panel B, the confusion matrices depict the model's performance in predicting reward-related events, such as air puff, left rewarded, left unrewarded, right rewarded, and right unrewarded. Here, dopamine provides the best performance, but overall accuracy is lower compared to task event classification. Notably, dopamine shows better accuracy for predicting reward choices, whereas dopamine shows relatively poor performance in predicting task-space behaviors.

We next conducted an analysis of S-D1 and S-D2 neuronal activity patterns in relation to historical reward data derived from Q-learning algorithms, which incorporate reward history (**Figure 7C**). Trials were categorized into high-value and low-value trials. In the DMS, when the mouse turned, dopamine release in high-value trials was higher than in low-value trials ($P < 0.0001$, one-sample t-test); the S-D1 activity in high-value trials was lower than in low-value trials ($P < 0.0001$). When the mice were in the contralateral choice port, S-D1 activity in the DMS in high-value trials was higher compared to low-value trials ($P < 0.0001$). However, dopamine and S-D2 activity did not exhibit differences depending on the values ($P > 0.05$). When the mice were in the ipsilateral choice port, S-D2 activity in the DMS in high-value trials was higher compared to low-value trials ($P < 0.0001$). However, S-D1 activity did not exhibit differences depending on the values ($P > 0.05$). The results of the value encoding (**Figure 7D**) highlight the performance of the classification models in predicting action values based on neural activity and dopamine release patterns. The confusion matrices show the classification results for different brain regions (DMS and DLS) and signals (Pnoc, Nts, and dopamine), with trials categorized into high-value and low-value groups for both left and right turns. The Pnoc signal in both DMS and DLS carries action value information only for high-value contralateral actions. Nts shows poor separation of high and low-value trials, and although dopamine contains value information, its accuracy is relatively low. Overall, dopamine worked as a better predictor for value compared to S-D1 or S-D2.

DISCUSSION

Our findings identify a set of direct and indirect pathways that arise in striosomes of the dorsal striatum and target the dopamine-containing neurons of the substantia nigra. This pair of pathways echoes the organization of the canonical direct and indirect motor pathways of the basal ganglia in having both direct and indirect access to its target destinations. These circuits originate in the striosome compartment of the striatum instead of the matrix compartment, the origin of the canonical direct and indirect pathways, and the striosomal circuits terminate in the dopamine-containing SNpc instead of the pallidonigral output nuclei of the basal ganglia. Evidence across rodent and non-human species suggests that striosomes might be particularly important for

energizing or engaging task-related behavior [65], for decisions involving conflicting and motivationally challenging approach or avoidance in situations combining favorable and unfavorable options [66–69], and for behavioral challenges present along the anxiety-depression and repetitive behavior-addiction axes [66,68,70,71]. Our findings thus raise the possibility that the basal ganglia have in place two major direct-indirect systems to exert control over behavior: one targeting the classic motor output nuclei of the striatum modulating action and the other targeting the nigral dopamine-containing neurons that modulate mood and the motivation to act, and likely influence the classical direct-indirect circuits. Further, these findings provide a framework for aligning the two great organizational features of the striatum, dividing the striatum into a direct-indirect pathway system and an apparently orthogonal striosome-matrix system. These organizational systems come together in the view proposed here, a finding that suggests an elegant evolution of circuit design in the forebrain.

We are aware that there are many other circuits in the complex basal ganglia connectome. For instance, the projection from striosomal cells to border GPi cells that project to and are reciprocally connected with the lateral habenula [24,32,72] a node in GPi output circuits that has been implicated in depression. Some (but not all) neurons so far recorded in the lateral habenula have characteristic firing patterns that are the opposite to those of most dopamine-containing cells [73,74], but more nearly resemble those of the lateral SNpc dopamine cells [75–77]. The lateral habenula itself receives striosomal input [78,79]. The conclusion supported by our findings here is that there are, in parallel, matrix-derived and striosome-derived direct and indirect pathways differentially targeting motor output (matrix) and dopamine neurons (striosomes). This model raises the possibility that evolution devised a way to coordinate the different functional manifolds of the two compartmental systems, one centered on motor control and the other on modulating mood and motivational modulation of physical and cognitive action.

Our work builds on pioneering studies on different segments of the pathways delineated here. Fujiyama and colleagues [34,40] and Kita and Kitai [55] found striatal neurons projecting to the zone of the pallidum likely corresponding to the GPe here demonstrated as a central, striosome-recipient zone of the GPe. The identity of these SPNs was not known. Gittis and colleagues [28] and Nelson and colleagues [80] described a pallidal input to nigral dopamine neurons, not identifying the GPe cells of origin with respect to their striatal inputs, but with identification of their projection to the cell bodies of the dopamine neurons. Work now even suggests that all GPe cells could receive D1 as well as the traditionally recognized D2 inputs due to extensive collateralization of the classic D1 direct pathway [21]. Exhaustive reviews of the connectivity of the pallidum have now further enriched understanding of the complex anatomy of the pallidum [25,29]. What we emphasize

here is evidence for synaptic throughput from D2 receptor-expressing striosomal SPNs to the central GPe zone (cGPe), marked by synaptophysin-labeled terminals onto cGPe neurons that are labeled by retrograde rabies viral injections into the SNpc of DAT-Cre mice. This indirect pathway thus is paired with the direct striosomal pathway to the dendrites and dendrons of the ventral tier dopamine-containing neurons of the SNpc [42].

Effects of the S-D1 and S-D2 pathways on dopamine release in the striatum

Our findings demonstrate contrasting characteristics of the S-D1 and the newly identified S-D2 pathway population activities in relation to dopamine release in the striatum and in their modulation during behavior in tasks involving free, uninstructed open field behavior and as well in the acquired T-maze task performance in which behavior is instructed and requires multiple points of decision-making for successful receipt of reward or, much less frequently, punishment in the form of an airpuff directed toward the mouse. The newly characterized S-D1 and S-D2 pathways, as represented by their enriched Pnoc (S-D1 proxy) and Nts (S-D2 proxy) sampled here, have largely opposing actions on striatal dopamine release, on the population activity of striatal neurons, on the in-task patterns of task-bracketing or not task-bracketing activities of these neuronal population firing, and on self-paced free locomotor movement. Yet these are time-varying relationships and differ for the more medial and more lateral parts of the dorsal striatum. For example, the task-bracketing pattern for the Pnoc SPNs in the DMS is not apparent for the DLS Pnoc populations examined simultaneously alongside the DMS Pnoc neurons. These DMS-DLS differences extend much previous work on differences between signaling in the DMS and DLS neurons unmarked with respect to their striosomal or matrix origins [81–89], thus indicating that topographic constraints are a general feature of striatal circuits. We did not sample a range of anterior-posterior locations, important for future investigation.

The striosomal direct and indirect pathways are parts of the nigro-striato-nigral loop

The nigro-striato-nigral loop is central to nearly all work on the basal ganglia related to disorders of mood and movement including neurodegenerative diseases, as witnessed by Parkinson's disease and Huntington's disease [90–92], and by a range of neuropsychiatric conditions [93–98] and to many studies of learning and normal adaptive behavioral control [99–101]. Here we introduce a new view of control pathways that can affect levels of dopamine in the striatum, which is the target of the nigrostriatal pathway and the site of origin of the striatonigral pathway. Remarkably, despite the relatively small total volume of the striosomal system relative to that of the matrix around it, the striosomes appear to have a strong influence on the nigrostriatal dopamine system and thus

on corticostriatal and other inputs to the striatum [71,102] and interneuronal circuits of the striatum [103,104] that are modulated by dopamine, likely across compartments. It is thought that striosomes are by far the predominant source of striatal input to the SNpc [42,80,105], though there are indications [106] even in our unpublished work that this may neglect some inputs from the matrix. The S-D1 pathway to the SNpc has already been implicated in the effects of psychomotor stimulants [107–110], opioid receptor-mediated negative affect [111], and likely on the craving induced by fentanyl withdrawal [111]. Further, this S-D1 pathway to the striosome-dendron bouquets is associated with the expression of endocannabinoid CB-1 receptors [112], and constitutive deletion of these receptors negatively affects the bouquet system [102]. There is a pressing need now to discover more about the striosomal control in different contexts and in different normal and abnormal conditions. We are in progress in trying to contribute to this effort.

The S-D2 circuit emphasizes an understudied target of potential dopamine D2 receptor actions and therapeutic significance

A rich body of pharmacologic work and pioneering therapeutic treatments of basal ganglia disorders target D2 receptors [113–116]. Here, we present evidence of a previously unrecognized D2 circuit arising from SPNs in striosomes that targets a specialized central region of the external pallidum that we here call the core region of the GPe (cGPe) by reference to the mouse GPe. The S-D2 SPN cell type has explicitly been singled out by single-nucleus RNA-sequencing (snRNA-seq) as the most vulnerable cell type in the brains of Huntington's disease mouse model mutants [117], a disease in which striosomes can be differentially affected in patients exhibiting mood symptoms [118,119]. It is possible that this vulnerability could affect the S-D2 indirect pathway identified here, leading to altered modulation of dopamine functions as well as cortico-striatal and thalamo-striatal function. More generally, effects on this indirect S-D2 circuit and its extension to dopamine-containing nigral neurons could account for some of the effects, including unwanted side effects, of a broad range of D2 agonist or antagonist treatments in neurology and psychiatry. It will be of great interest for further work to approach this issue. More highly targeted therapies directed at the S-D2 or M-D2 pathways could improve treatment efficacy, if the differential functions of striosomes and matrix as we have so far found in mice [65,68,69,111] hold true within the D2 population and also holds true in humans.

Opposing pathways

The classical direct-indirect model heavily relies on the clinical symptomatology of neurodegenerative disorders such as Parkinson's disease and Huntington's disease [1,2,6]. Namely,

in the dopamine-depleted state, lower dopamine tone decreases activity in the Go (D1) pathway, leading to bradykinesia. In Huntington's disease, preferential depletion of the No-Go (D2) pathway disinhibits motor commands, resulting in hyperkinesia. Supporting this standard model, there is accumulating experimental evidence indicating that the function of the classic direct pathway is to disinhibit motor neurons, for example, to release motor commands by inhibiting omnipause neurons in the motor output nuclei of basal ganglia [120,121]. By contrast, the function of the indirect pathway remains obscure: for example, how it inhibits unwanted or irrelevant movements (as by targeted coactivation [18,122]), and how its deficits are manifested as cholera, tics or dystonia. On top of the ongoing debate over the canonical model, here we showed the striosomal system can exhibit the opposite effects, whereby S-D1 suppresses and S-D2 facilitates locomotion and associated movements. How does the preferential depletion of S-D2 [117] contribute to early-stage symptoms of Huntington's disease? One possibility is that this relates to deficits in incentive motives for actions (e.g., apathy and depression) or psychiatric symptoms (e.g., psychosis, delusions) observed years before the clinical onset of Parkinson's disease and Huntington's disease [123–125]. Furthermore, our results suggest that the striosomal and matrix systems work oppositely within the same direct or indirect pathway. Clearly, the standard model of basal ganglia networks awaits update.

Timing in the striosomal circuits targeting dopamine-containing neurons of the substantia nigra

Evidence from the work of several laboratories suggests that the GPe pathway to the SNpc dopamine neurons terminates on the cell bodies of these neurons [28,33,106]. It is reasonable to guess that these connections include the S-D2 pathway inputs identified here. This situation could pose a potentially important way that the S-D1 and S-D2 pathways could operate, given that the S-D1 pathway terminates mainly on the descending dendrites of ventral tier SNpc neurons, including dendrons of the striosome-dendron bouquets and much less the cell bodies of the parent dopamine-containing neurons, as well as the still mysterious 'posterior cell cluster' neurons as they are currently denominated. Different timing of these somatic S-D2 and dendritic S-D1 inputs could be critical to the functions of the nigrostriatal control circuits, in coordination with timed inputs from the cerebellum [154]. Striosomal direct-indirect circuits with different lags could dynamically adjust in the correlations between S-D1 and S-D2 effects in relation to dopamine release.

Task-bracketing and inverse task-bracketing

In analyzing the probabilistic decision-making task, we found a remarkable inverse relationship between the activity of the S-D1 and S-D2 population activities in the DMS. For presumed driving of contralateral striatal function, the putative S-D1 population activity peaked at the beginning and end of the runs, including the entire out-back run sequence, whereas the S-D2 population mainly peaked at the turn. Opposite effects present for task-bracketing by populations of neurons in the striatum were first noted in tetrode recording patterns in rats running a cued two-arm maze with random baiting of the right or left end-arms [126–132] and then in recordings in the macaque prefrontal cortex [133], with multiple subsequent studies confirming this patterning in rats and mice [132,134–137] and in macaque striatum [138]. These tasks did not include a rewarded return to the initiation site, and recordings were made unilaterally. In the tetrode studies [127], the task-bracketing was found in the DLS, but not in the DMS, for which the activity instead resembled the S-D2 recordings in the DLS (gradual rise and fall) and for which the decline appeared to exert a permissive role in allowing behavioral expression of the bracketing. These recordings did not differentiate either D1- and D2-expressing populations or striosomal and matrix sub-populations. There was a strong potential influence of striatal PV-expressing interneurons, which peaked mid-run like to dopamine signals recorded here; these had the inverse of the S-D1 task-bracketing patterns [135].

Our study demonstrates the efficacy of using neural activity patterns to predict behavior and decision outcomes. We trained classifiers to distinguish between task-space behaviors and reward-related events, demonstrating distinct neural signatures across different brain regions and signals. Notably, dopamine in the DMS exhibited significantly higher-than-chance accuracy for initiating actions and making contralateral choices, whereas Pnoc and Nts signals in both DMS and DLS exhibited robust predictive power across all task events. However, the predictive accuracy of dopamine for reward-related events, although the best among the signals, was overall lower compared to its ability to predict task events. Neither Pnoc nor Nts striosomal populations showed significant predictive power for reward-related outcomes. Further analysis of S-D1 and S-D2 neuronal activity patterns and dopamine release patterns indicated that the encoding of action value was primarily present in the dopamine signals but not in the Pnoc and Nts striosomal population signals. These results clearly differentiate the population encoding on the part of striosomal S-D1 and S-D2 populations and the encoding by dopamine release recorded in the same striatal subdivisions. Task events preceding reward can be decoded by the S-D1 and S-D2 population activities, but it is the dopamine release that can be used to decode outcome value. Further analysis of the activity of single S-D1 and S-D2 cells comparable to those, almost all of which were without identification of the striosomal neuronal subtypes[152], should clarify potential outcome encoding by the striosomal SPNs.

Evolutionary perspective evoked by the current findings

Our evidence points to a similar circuit design of the classic direct-indirect basal ganglia pathways and the striosomal direct-indirect pathways delineated here. The many overlapping and bridging collateral innervations in the GPe and elsewhere could be seen as diluting the "direct" and "indirect" pathway concept beyond usefulness [7,21,22,40]. But this is not so when attention is given to the direct targeting and indirect targeting of some of these pathways at their terminations, whether within the motor output stations of the canonical pathways or within the dopamine neuron destinations of the S-D1 and S-D2 pathways. We have scarcely any full accounting of even the anatomy of these pathways in different species. But as markers become available, including ATAC-seq-based enhancers [139,140], it will be possible to test their relationship in detail. Certainly, the snRNA-seq data available suggest conservation of S-D1 and S-D2 identities from mouse to human, though with many different mRNAs expressed across these species [117,141]. We note that in the human brain, there are three distinguishable segments of the pallidum. How these relate to our findings is unclear but of obvious interest. We also note that very little is known about the posterior cell cluster, defined as a major target of the S-D1 pathway along with the striosome-dendron bouquet system [42]. And important also are the frequently found contrasts between the DMS and DLS in rodents. These have possible, but not definitely identified, correlates in, respectively, parts of the caudate nucleus and putamen of primates, including humans. The rules of the partitioning are not yet clear but are likely driven by functional needs.

Future work and limitations to be addressed

Our experiments represent an initial stage of characterizing the direct S-D1 and newly identified indirect S-D2 pathways, and they both leave many questions for future work and expose weaknesses in our ability to characterize these here in satisfyingly complete detail.

We used proxies for the S-D1 and S-D2 populations, because we could not use direct labeling of the S-D1 and S-D2 populations given that the direct and indirect matrix pathways also terminate in or pass through the GPe. But these proxies are not perfect. Pnoc-Cre targets only ~40% of S-D1 neurons (**Supplementary Figure 4**) and the Nts-Cre expression pattern includes the scattered, unclustered neurons that occupy the dorsolateral calbindin-poor crescent. We do know that some of the non-Pnoc neurons express *prodynorphin* (*Pdyn*), reported to be associated with reward and appetitive responses, that others express *Tshz1*, reported to be related to punishment and avoidant behavior, that Pnoc neurons and some express both of these. Pnoc-Cre targeted neurons here used as proxies for the D1 direct striosomal pathway to the SNpc (S-

D1) are not seen to exclusively overlap with either *Pdyn* or *Tshz1* labeled S-D1 neurons. We have some supporting anatomical evidence for the S-D1 and S-D2 from the enhancer distributions illustrated, but further work needs to be done to decrease these uncertainties. We do not yet know the relationship between our findings for enhanced populations of striosomal and matrix striatal neurons, and the many current studies done without this compartmental differentiation other than that the matrix population, volumetrically, exceeds that of the striosomal system in most parts of the striatum and might therefore dominate the results.

Despite our attempt to sample striatal sites in both DMS and DLS, our coverage of the dorsal striatum was limited. We did not survey anteroposterior and dorsoventral sites, or all of the dorsal striatum as a whole. Nevertheless, the differences between the DMS and DLS sites that we did sample gave strong evidence adding to many other lines of evidence [81–89] that local topographic specializations are of paramount importance in analyzing the striatum, just as they are in analyzing its largest input source, the cerebral cortex [142–145].

We also acknowledge that there are many other circuits that can influence the striatum and its interactions with the nigral dopamine system, for example the circuits that link striatum with the cerebellum [154].

We have presented an initial delineation and characterization of the S-D1 and S-D2 striosomal direct and indirect pathways paralleling the canonical M-D1 and M-D2 pathways, but we have not yet made adequate comparisons between these pairs of direct-indirect pathways for all but a few observations. It will be of great interest to test the range of specializations of these two parallel sets of basal ganglia circuits. Experiments with chemogenetic manipulation (DREAADs) should be especially useful, and we intend to employ these. We also have not yet developed a computational model of how the striosome-derived and matrix-derived direct and indirect pathways could operate together (or in time-varying opposition) in tasks involving both motoric and evaluative demands, or the use of different body parts. The evolutionary constraints potentially leading to this pairing of striosome and matrix pathways also remain to be addressed.

The work presented here is thus a first demonstration of the parallel S-D1/S-D2 and M-D1/M-D2 organization of the striatum that should lead to fundamentally revised models of basal ganglia function. It is hoped that this work could benefit the clinic and the millions of individuals affected by disorders referable to basal ganglia dysfunction.

Materials and Methods

Mouse husbandry

All procedures were approved by the Committee on Animal Care at the Massachusetts Institute of Technology, which is AAALAC accredited. Supplementary Table 1 summarizes the mouse lines used. Experimental mice were female and male and maintained on a standard 12/12 h light/dark cycle with free access to food and water. P172 mice were evaluated at age 3-5 weeks. The other mice were evaluated at ages ranging from 2-10 months of age. Table 1 describes the various transgenic mice used.

Generation of AT1-tdTomato BAC transgenic mice

The BAC containing AGTR1 (RP24-63B19) was obtained from the BACPAC Resource Center at CHORI. Plasmids for cloning and recombineering were obtained from The Rockefeller University and Jonathan Ting in the laboratory of Guoping Feng. Two flanking sequences for homologous recombination consisted each of 500 basepairs, one upstream of the ATG start codon and the other beginning in the following intron, in order to remove the first coding exon and prevent overexpression. The iCre-P2A-TdTomato expression cassette was amplified from pAAV-EF1a-iCre-P2A-TdTomato. PCR-amplified and gel-purified Homology Box A and iCre-P2A-TdTomato were inserted into iTV vector by In-Fusion (Clontech) and transformed into DH10B bacteria. In-Fusion was then performed between the iTV-iCre-P2A-TdTomato-Box A and homology box B and the resulting vector was linearized and purified for homologous recombination. The Agtr1 BAC was transformed into el250 bacteria and selected on chloramphenicol-media plates from which colonies were picked and grown overnight in LB-Lennox at 32°C. 400 ml of culture was transferred to 20 ml of LB-Lennox and placed at 32°C until A600=~0.4. Cells were then transferred to Eppendorf tubes and heat shocked at 42°C for 15 minutes with occasional shaking. The bacteria were cooled for 5 minutes on wet ice and then centrifuged at 10,000xg for 15s. Washes with cold 10% glycerol were performed twice and the cells were resuspended in the remaining volume. Linearized iTV-iCre-P2A-TdTomato-Boxes vector was electroporated (1.75 kV, 25 uF and 200 Ohms) into the Agtr1-BAC bacteria, put on ice for 2 minutes, resuspended in 1 ml of LB-Lennox, and incubated at 32°C for 2h. Cells were then pelleted at 4000 rpm for 4 minutes, plated onto LB-agar chloramphenicol/kanamycin plates and incubated at 32°C overnight. Colonies were picked and grown overnight in 5ml of LB, glycerol stocks made and a columnless Qiagen miniprep was performed. Bacteria was streaked out onto chloramphenicol kanamycin LB-agar plates from the glycerol stocks of positive clones. Colonies were selected and grown in 1 ml LB + chloramphenicol/kanamycin at 32°C for 6-8h with addition of arabinose during the last hour to induce Cre expression and removal of the neomycin cassette. Bacteria were plated and colony PCR was used to identify neomycin-negative clones that were inoculated into 5 mL LB (Miller)

with chloramphenicol and grown for 8 hours and 32°C. This culture was added to 200 mL LB (Miller), grown overnight and used for DNA preparation with the Nucleobond Xtra BAC kit. Approximately 7 mg BAC DNA was then linearized with NotI. The linearized DNA was then run on PFGE in a single well. The next day, the sides of the gel were stained and the unstained was aligned and the appropriate sized band was excised. The gel slice was cut in half length-wise and put into Spectra/Por Dialysis tubing (MWCO:6-8,000) to which 500 ml TE was added. The clamped tubing was put into a pulsed field gel electrophoresis box perpendicular to the flow of the current and run under the following settings: 35s initial, 35s final and a run time of 8h. After 8 hours the tubing was rotated 180° and run for another 6 minutes. The eluate was removed from the tubing and then run over a column prepared as follows: add water to the column, add 1.5 mL G50 sephadex beads to column, fill column with 1x TE. Samples were collected in 2-drop fractions and 5 ml of each fraction was run on an agarose to find the 5 most concentrated fractions, which were then combined. Microinjection buffer (100 mM NaCl, 10 mM Tris HCl, 0.1 mM EDTA, pH7.4) was filtered through a 0.2um syringe filter and put into a beaker. A spot dialysis disc (0.025 um VSWP) was placed on top of the microinjection buffer and then sample was put on the disc. The sample was left to dialyze overnight at 4°C. AT1-BAC-tdTomato DNA (0.5 – 1 ng/ml) with polyamines added 1 week prior, was given to the MIT transgenic facility for C57B6/N pronuclear injection. Multiple founder mouse lines were screened for optimal expression of tdTomato in histological brain sections.

Generation of rabies viruses

Cloning of AAV genome plasmids pAAV-syn-FLEX-splitTVA-EGFP-tTA (Addgene 100798) and pAAV-TREtight-mTagBFP2-B19G (Addgene 100799) has been described [146]. These genomes were packaged in serotype 1 AAV capsids by, and are available for purchase from, Addgene (catalog numbers 100798-AAV1, and 100799-AAV1) and diluted in Dulbecco's phosphate-buffered saline (DPBS) (Fisher, 14-190-250) by factors of 1:200 and 1:10, respectively, to final titers (determined by Addgene by qPCR) of 8.5 × 10^10 gc/ml and 1.6 × 10^12 gc/ml, respectively, then combined in a 50/50 ratio by volume as described 56 before injection. EnvA-enveloped rabies virus RVΔG-4mCherry (EnvA) [147] was produced as described previously [148–150] but using helper plasmids pCAG-B19N (Addgene #59924), pCAG-B19P (Addgene #59925), pCAG-B19G (Addgene #59921), pCAG-B19L (Addgene #59922), and pCAG-T7pol (Addgene #59926) for the rescue step [150], with a final titer of 1.70 × 10^10 infectious units/ml as determined by infection of TVA-expressing cells as described previously [148].

Striatal cell type enhancer discovery

The DLX2.0 enhancer is a 3x concatenated core of the hDLX enhancer and has been previously described in terms of neocortical GABAergic cell type specificity and rapid onset of expression in human ex vivo brain slice cultures [140,141]. Here we describe for the first time the unique enrichment of transgene expression driven by the DLX2.0 enhancer in striosomes of the dorsal striatum region following mouse in vivo stereotaxic injection. The striosome enrichment pattern is not observed follow intravenous virus administration using PHP.eB serotype in mice (data not shown). Striatal brain region and cell type specific enhancers 452h and 444h were identified from Roussos lab Brain Open Chromatin Atlas (BOCA) resource [155], a publicly available human postmortem bulk dataset using assay for transposase accessible chromatin with RNA sequencing (ATAC-seq) profiling. The BOCA resource covers various cortical brain regions, amygdala, thalamus, hippocampus, and striatum brain regions and clustering of neuronal vs non-neuronal cell types. We identified putative enhancers based on differential chromatin accessibility in putamen and nucleus accumbens regions of the human striatum relative to other brain regions, as well as proximity to known marker genes for major striatal medium spiny neuron types (e.g., DRD2 as a marker gene for indirect pathway medium spiny neurons).

Enhancer AAV cloning

Candidate enhancers were PCR amplified from human genomic DNA and cloned using standard restriction enzyme digestion and ligation into AAV expression vectors upstream of a minimal beta-globin promoter (minBG) and mTFP1, bright monomeric teal fluorescent protein that is well tolerated in neurons. The resultant AAV plasmids were rAAV-452h-minBG-mTFP1-WPRE3-BGHpA (Addgene plasmid #191708, alias AiP12700) and rAAV-444h-minBG-mTFP1-WPRE3-BGHpA (Addgene plasmid #191729, alias AiP12965). To investigate Cre- and Flp- dependent intersectional strategies for striosome labeling, we additionally constructed rAAV-DLX2.0-DIO-SYFP2 (plasmid AiP14533) and rAAV-DLX2.0-FlpO-WPRE3-BGHpA (plasmid AiP4532) vector designs by standard subcloning.

Virus production

We prepared endotoxin free maxiprep DNA for packaging AAV plasmids into PHP.eB serotypes AAV particles. For initial enhancer-AAV screening by intravenous delivery in mouse we generated small-scale crude AAV preps by transfecting 15 µg maxiprep enhancer-reporter DNA,15 µg PHP.eB cap plasmid, and 30 µg pHelper plasmid into one 15-cm dish of confluent HEK-293T cells using PEI-Max. At one day post-transfection the medium was changed to 1% fetal bovine

serum, and after 3 days the cells and supernatant were collected, freeze-thawed 3x to release AAV particles, treated with benzonase (1 µL) for 1 hr to degrade free DNA, then clarified (3000g 10min) and concentrated to approximately 150 µL by using an Amicon Ultra-15 centrifugal filter unit at 5000g for 30-60 min (NMWL 100 kDa, Sigma #Z740210-24EA). For large-scale gradient preps for intraparenchymal injection into mouse brain, we instead transfected 10 x 15-cm plates of HEK-293T cells and purified the cell lysates by iodixanol gradient centrifugation. We titered both crude and gradient AAV preps by digital droplet PCR.

Stereotactic injections with viruses

AAV9-CMV-Flex-synaptophysin-mCherry (1 ml, 2X1013vg/ml, purchased from Dr. Rachael Neve) was injected into the dorsal striatum (AP:1.2, ML:1.4, DV:-2.0) of one AT1-Cre-tdTomato line F mice and 5 weeks later the brain was harvested and processed for immunolabeling with dopamine transporter (DAT). The mCherry fluorescence was imaged directly so as to minimize cross-detection of AT1-tdTomato, which is relatively weak.

PV-Cre or DAT-Cre heterozygous mice or double transgenic PV-Cre;P172-mCitrine (hemizygous) and DAT-Cre; P172-mCitrine (hemizygous) were kept under deep anesthesia with a continuous flow of 2% isoflurane (Southmedic Inc.) in an oxygen mixture, delivered by a nose-cone attached to a stereotax. Mice were given intranigral injections of a mixture of pAAV-syn-FLEX-splitTVA-EGFP-tTA and pAAV-TREtight-mTagBFP2-B19G in 0.4 ml DPBS, via NanoFil microsyringe (World Precision Instruments) at the following stereotactic coordinates: AP:-2.7 ML:+/-1.7, DV:-3.7 to target the ventral SNc in DAT-Cre mice, and AP:-2.8, ML:+/-1.7, DV: -4.1 to target the ventral SNr in PV-Cre mice. Rabies virus, in 0.4 ml DPBS, was injected into the same site 7 days later and brains were perfused 7 days after rabies injection. Stereotactic coordinates were modified slightly in single-transgenic mice that were older, to account for their larger brain size (< 4-week old mice are necessary for P172-mCitrine transgene imaging).

Tissue preparation, immunolabeling and microscopy

Mice were anesthetized with Euthasol (Virbac AH Inc.; pentobarbital sodium and phenytoin sodium) or isoflurane and then trans-cardially perfused with 0.9% saline, followed by 4% (wt/vol) paraformaldehyde in 0.1 M NaKPO4 buffer solution (PBS). Brains were then dissected, post-fixed for 90 min, stored in 20% (vol/vol) glycerin sinking solution overnight or longer, and cut into transverse 30 µm sections on a freezing microtome. Sections were stored in 0.1% sodium azide in 0.1 M PBS made from NaKPO4 until use.

Free-floating sections were rinsed 3 times for 2 min each in 0.01 M PBS with 0.2% Triton X-100 and then were blocked for 20 min in TSA Blocking Reagent (Perkin Elmer). Sections were incubated with primary antibodies (Supplementary Table 2) suspended in TSA Blocking Reagent overnight at 4°C on a shaker. Following primary incubation, sections were rinsed 3 times for 2 min each in 0.01 M PBS with 0.2% Triton X-100 and were incubated in Alexa Fluor secondary antibodies (Thermo Fisher Scientific) (Table S2) suspended in TSA Blocking Reagent for 2 h at room temperature. Following secondary incubation, sections were rinsed 3 times for 2 min each in 0.1 M PBS. For confocal microscopy, sections were mounted on subbed glass slides and coverslipped with ProLong antifade reagent with DAPI (Thermo Fisher Scientific).

A Zeiss Axiozoom microscope was used to obtain wide-field images with standard epifluorescence filter sets for DAPI (365 excitation, 395 beamsplitter, 445/50 emission), eGFP/AF488 (470/40 excitation, 495 beam splitter, 525/50 emission), tdTomato/AF546 (550/25 excitation, 570 beamsplitter, 605/70 emission) and Cy5/AF647 (640/30 excitation, 660 beamsplitter, 690/50 emission). Confocal imaging was performed with a Zeiss LSM510 with diode lasers (473, 559, 653 nm) for excitation. Images were collected with a 10x 0.4 NA objective and a 60X silicon oil 1.3 NA objective lens. Optical sectioning was optimized according to the microscope software. Images were processed and analyzed with Fiji software. Maximum intensity projection images were generated from optical sections using Image J. Background was subtracted and contrast was adjusted for presentation. Figures were prepared with Photoshop and Adobe Illustrator 6.0.

Cell counting in transgenic mice

Two female and two male mice were used for each mouse line and three coronal sections, taken from the anterior, mid-level and caudal regions, were evaluated for each mouse. Neurons were counted in all of the MOR1-identified striosomes that were dorsal to the anterior commissure. A composite image of the 3 channels GFP (green), tdTomato (red) and MOR1 (cyan) was created in the Fiji software. Individual and merged channels were viewed with the channels menu and the brightness and contrast of the image was adjusted as necessary with the brightness/contrast menu. To divide the dorsal striatum into medial and lateral sides, a horizontal line was drawn across the widest part of the striatum with the straight line tool. A vertical line was drawn to bisect the striatum and then it was traced (pink) with the pen tool. The cyan channel only was viewed and the MOR1 striosomes were outlined (teal) with the pen tool. To define the area of the matrisomes, the striosomes were outlined with the freehand selections tool and the selected area was moved to an area next to the striosomes. For each mouse line, cells were counted in the

following categories: GFP labeled cells in the MOR1 striosome, GFP labeled cells in the matrix, GFP and tdTomato double labeled cells in the total MOR1 striosome and matrix, GFP single labeled cells in the total MOR1 striosome and matrix, double labeled cells in the MOR1 striosome, GFP single labeled cells in the MOR1 striosome, double labeled cells in the matrix, GFP single labeled cells in the matrix, double labeled cells in the matrisomes, tDTomato labeled cells in the MOR1 striosome, and tDTomato labeled cells in the matrisome (P172) or matrix (AT1LineF).

Photometry recordings

Calcium activity was recorded utilizing GCaMP8s and the red-shifted DA sensor DA3h with two-color bundle-imaging fiber photometry system (Doric lenses). This setup allowed for the sequential recording of fiber photometry fluorescence data at a sampling rate of 10 Hz across three distinct channels: a reference channel (400-410 nm), a green channel (460-490 nm), and a red channel (555-570 nm). Video recordings of mouse behavior were synchronized with photometry signals, capturing the xy-coordinates of five body parts: the tip of the tail, the base of the tail, the center of the body, the neck and the snout/head, using DeepLabCut software. Both video and photometry frames, alongside task events or optogenetic stimulation, were timestamped, employing Bonsai software, which interfaced with external hardware via an Arduino microcontroller operating on the Firmata-plus protocol.

The preprocessing of photometry recordings involved scaling the 400-410 nm control signal to the 460-490 nm neuronal activity signal or 555-570 nm DA sensor signal via linear least-squares regression, followed by subtraction to eliminate motion and autofluorescence-related artifacts. The baseline fluorescence of the activity signal was estimated over time using a least-squares regression line applied to the scaled control signal. This corrected activity signal was then normalized against the raw baseline estimate, resulting in a $\Delta F/F$ trace that was adjusted for photobleaching, motion, and autofluorescence.

Open field

In the open field, mice subjected to overnight water deprivation freely explored a 30x30 cm arena for 15 minutes, allowing evaluation of locomotor activity. The floor, made of clear transparent acrylic, facilitated video capture from below using a high-resolution Oryx 10GigE camera (Flir), recording at 30 Hz synchronized with fiber photometry data, capturing both neural activity, dopamine release, and behavioral patterns. This approach enabled correlating locomotor behaviors with neural and dopamine dynamics. Movement was analyzed with DeepLabCut [157], where 1000 frames from all sessions were manually labeled to identify the tip of the tail, the base

of the tail, the center of the body, the neck and snout. After applying DeepLabCut to the videos, we converted video coordinates in pixels to coordinates in centimeters through a transform using the dimensions of the arena. Optogenetic stimulation of Chrimson was delivered using a 593 nm laser at 40 Hz. The duration of the stimulation was 8 seconds, repeated for 10 trials with a randomized inter-trial interval (ITI) of 1.5 minutes. Trajectory lengths for each mouse during pre-stimulation, stimulation, and post-stimulation periods were calculated to determine overall displacement. The analysis compared these displacements to identify changes in movement patterns related to the optogenetic stimulation. Speed of movement was assessed across experimental phases and categorized into activity levels: immobile (<2 cm/sec), mobile (2-6 cm/sec), and running (>6 cm/sec). Time spent in each activity level was quantified across optogenetic manipulation phases: pre-, during, and post-stimulation.

Behavioral motif analysis

Behavioral motifs were identified using B-SOiD [156], a tool for clustering behavior into short-length movement motifs. For clustering, video recordings were preprocessed with DeepLabCut [157], which annotated six body parts: snout, tail base, left front paw, right front paw, left hind paw, and right hind paw. We then calculated the average motif usage frequency (in frames per second) for both the stimulation-on and stimulation-off periods. The stimulation-on period was defined as the time during which optical stimulation was delivered (8 seconds per instance, ten times per session), while the stimulation-off period was determined from 8 seconds before to the start of each stimulation. We evaluated changes in motif usage between these conditions using a two-tailed t-test and computed the ratio of motif usage between the stimulation-off and on periods. Motif usage ratios were visualized using box plots generated with a Python library, displaying quartiles of the dataset and extending whiskers to show the distribution, excluding outliers determined by the 1.5 inter-quartile range rule. Motifs that were absent during sessions for certain mice were excluded from the analysis for those specific individuals, leading to some of the plots that do not include all the mice (n = 8 for Pnoc, n = 11 for Nts).

Kinematic analysis

Kinematic data were calculated from the body parts coordination data, which was annotated by DeepLabCut. Movement speed was calculated using the center of body coordinate. Body twist angle was defined as the angle between the "tail base to center of body" and "center of body to neck" vectors. Similarly, head twist angle was measured between the "center of body to neck" and "neck to snout" vectors. We aggregated kinematic data from all mice in the Pnoc and Nts

groups to plot the total distribution density of each variable. Angular velocities were histogrammed in 0.2 degree/sec bins from 0 to 20 degrees/sec (100 bins in total), smoothed over 5 bins to enhance visual clarity. Movement speed were histogrammed in 1 frame/sec bins from 0 to 1000 frames/sec (1000 bins in total), smoothed over 50 bins. All the histograms were then converted to distribution densities by normalizing the area under the curve to be 1. We calculated average head-twist and body-twist angular velocities, and movement speeds for each mouse, separating data according to motif. We then compared these kinematic variables between stimulation-off and -on periods to assess the effects of light stimulation on mouse movement kinetics, using a two-tailed t-test. The results were visually represented in box plots with swarm plots detailing the ratio of each kinematic variable between the stimulation-on and -off periods (n = 8 for Pnoc, n = 11 for Nts).

T-maze probabilistic 2-choice switching task

This task is a modified version of the probabilistic 2-choice switching task [151], implemented in a T-maze to spatially and temporally extend the action selection process, thereby facilitating the identification of action value encoding in neural signals. In this adapted version, mice were trained to choose between two options with reinforcement outcomes that intermittently swapped without warning. Notably, a 3μl sucrose reward was introduced at the initiation port, and an air puff was administered in 5% of incorrect choices as a form of negative reinforcement. This setup aimed to encourage a "win-stay, lose-switch" strategy, requiring mice to adjust their choices in response to changing reinforcement outcomes. Specifically, one port had a 75% chance of providing a sucrose reward, while the other was non-reinforced. The reinforcement schedule for these ports was subject to random switches every 7-24 rewarded trials. Video data were collected and processed with Bonsai software, enabling real-time detection of corridor end zone entries. The system was automated through two Arduino microcontrollers managing the water spouts and interfacing with Bonsai via the Firmata protocol. High-resolution video frames from a FLIR-Oryx 10GigE camera were synchronized with the photometry setup, recording at 30 frames per second. This setup facilitated the simultaneous recording of neuronal activity and dopamine release at a 10 Hz sampling rate across three channels: a reference (400-410 nm), green (460-490 nm), and red (555-570 nm). Behavior and action value were analyzed using a Q-learning model for each animal individually, assessing adjustments in decision-making strategies in response to dynamic changes in reinforcement.

Action value estimation using Q-learning

Behavior and action value were analyzed using a Q-learning model for each animal individually, assessing adjustments in decision-making strategies in response to dynamic changes in reinforcement. To calculate the action values for different choices made during the task, we utilized a Q-learning model. This model allowed us to update the estimated value of each option based on reinforcement outcomes. We used the following update rule for action values:

$$Q_p(t+1) = Q_p(t) + \alpha(R(t) - W_{airpuff}A(t) - Q_p(t)$$

where Qp(t): Current action value of choosing port p at time t, α: Learning rate, which controls how quickly the values are updated, R(t): Outcome received at time t (1 for a reward, 0 for an omission, $W_{airpuff}$: Penalty associated with receiving an airpuff, A(t): Binary indicator of whether an airpuff trial occurred. We then used a logistic function to calculate the probability of choosing the right port:

$$P_r(t) = \frac{1}{1 + exp\,(-\beta\big(Q_r(t) - Q_l(t)\big) + b}$$

where β : parameter controlling the slope of the function and the explore-exploit trade-off, b: static bias toward one side.

We first estimated the parameters ,Wairpuff, and b for each animal individually by minimizing the negative log-likelihood:

$$argmin_{\alpha, W_{airpuff}, \beta, b} \sum_{sessions} \sum_{t} - logP_p(t|\alpha, W_{airpuff}, \beta, b)$$

The parameters were optimized using the downhill simplex algorithm implemented through the scipy.optimize.fmin function in python. However, we observed a significant number of outliers in the Wairpuff values, likely due to the limited number of trials in each session. To address this, we recalculated the mean value of Wairpuff across sessions and use that as a default Wairpuff, subsequently only refitted the parameters , and b using adjusted mean of Wairpuff.

Signal analysis

Signal data were analyzed using custom scripts developed in MATLAB. Five key events were identified for analysis: Trial Start, Initiation Port Exit, Turn, Choice Port Entry, and Choice Port Exit. For each event, we calculated the median inter-event intervals from successive pairs. These intervals were used to define a symmetric time window centered on each event, extending from half the median interval before the event to half the median interval after the event. These windows were then combined, allowing for a comprehensive visualization of all trials, accommodating variations in inter-event intervals. This approach facilitated a detailed examination of the temporal dynamics across different trial phases.

Task bracketing index

The Task Bracketing Index was calculated by first isolating segments of each trial, spanning from initiation to choice. The index was then derived by measuring the mean signal value at the beginning and end segments of the trial—each defined as 25% of the total trial length—and subtracting the mean signal value of the central segment, which comprises the remaining 50% of the trial.

Cross-correlation

For each trial, we compared the signal activity of one signal (e.g., neuronal signal Pnoc, Nts) against another signal (e.g., DA release) using the MATLAB crosscorr function. We computed the cross-correlation coefficient across various time lags, ranging from -1 second to +1 second. The cross-correlation coefficients were plotted against the lag values, with positive lags indicating that the first signal leads the second, and negative lags indicating that the second signal leads the first.

LSTM classifier

We developed Long Short-Term Memory (LSTM) classifiers to categorize task space and choice space events, similar to our CNN approach. The LSTM model was constructed using the Keras Sequential API and included the following layers: an LSTM layer with 32 units and return_sequences=True, a dropout layer with a 0.3 dropout rate, another LSTM layer with 32 units and return_sequences=False, another dropout layer with a 0.3 dropout rate, a dense layer with 16 units and ReLU activation with L2 regularization (0.01), and a softmax output layer for classification. The model was compiled using the Adam optimizer and the sparse categorical cross-entropy loss function, with accuracy as the performance metric.

Value classification

To investigate the neural encoding of action values, we categorized trials into three distinct groups based on the absolute values of the action values, using the first (Q1) and third (Q3) quartiles in each session as thresholds. Trials were classified as high-value when the absolute action values exceeded the Q3 threshold and as low-value when the absolute action values fell below the Q1 threshold. This classification was performed individually for each session to ensure an accurate reflection of the session-specific distribution of action values.

We used a total of 6 seconds of data from each signal, spanning from -3s to 3s relative to the middle region of interest (ROI), as input. The data was then categorized into four classes: High-value left turn trials, High-value right turn trials, Low-value left turn trials, and Low-value right turn trials. For classification, we employed the same CNN and LSTM models described previously. The classification models were developed on a per-animal basis by merging all sessions from a single animal, as individual sessions contained insufficient data to train the classifiers effectively.

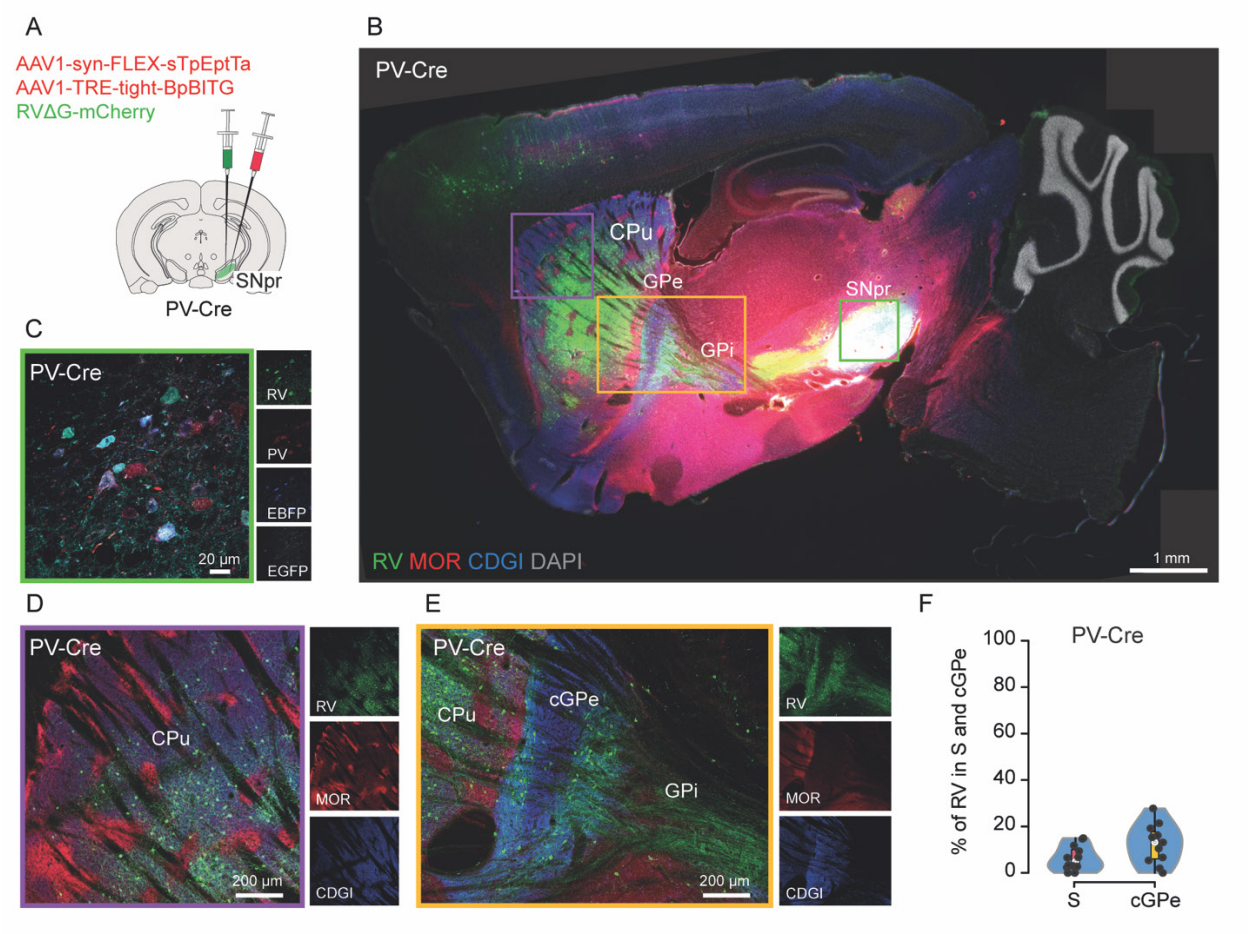

Figure. 1: Distribution of RVΔG-labeled neurons targeting PV neurons in SNpr.
A. Illustration of the injection site, a combination of AAV1-syn-FLEX-sTpEptTa and AAV1-TRE-tight-BpBITG followed by EnvA-pseudotyped mCherry-expressing rabies virus (RVΔG) were injected into the SNpr of PV-Cre mice, 21 days apart.
B. Representative sagittal section depicting RVΔG-mCherry (green) labeled neurons counterstained with anti-MOR1 (striosome marker, red), anti-CDGI (matrix marker, blue) and DAPI (gray) staining. RVΔG-mCherry labeled presynaptic neurons (green) are located preferentially in the matrix and the shGPe.
C. SNpr injection site (orange box in b), depicting starter neurons co-expressing the RVΔG-mCherry (green), PV (red) together with EBFP and EGFP from the two helper viruses.
D. Striatal region (magenta box in B), showing that presynaptic neurons projecting to SNpr-PV cells are localized preferentially in matrix.
E. GPe region (yellow box in B), showing that presynaptic neurons projecting to SNpr-PV cells are localized preferentially in the shell MOR1-poor/CDGI-rich zone.
F. Quantification of RV labeled neurons targeting PV neurons in the SNpr. CPu: n = 1434 neurons / 12 sections / 3 PV-cre, GPe: n = 305 neurons / 11 sections / 3 PV-cre.

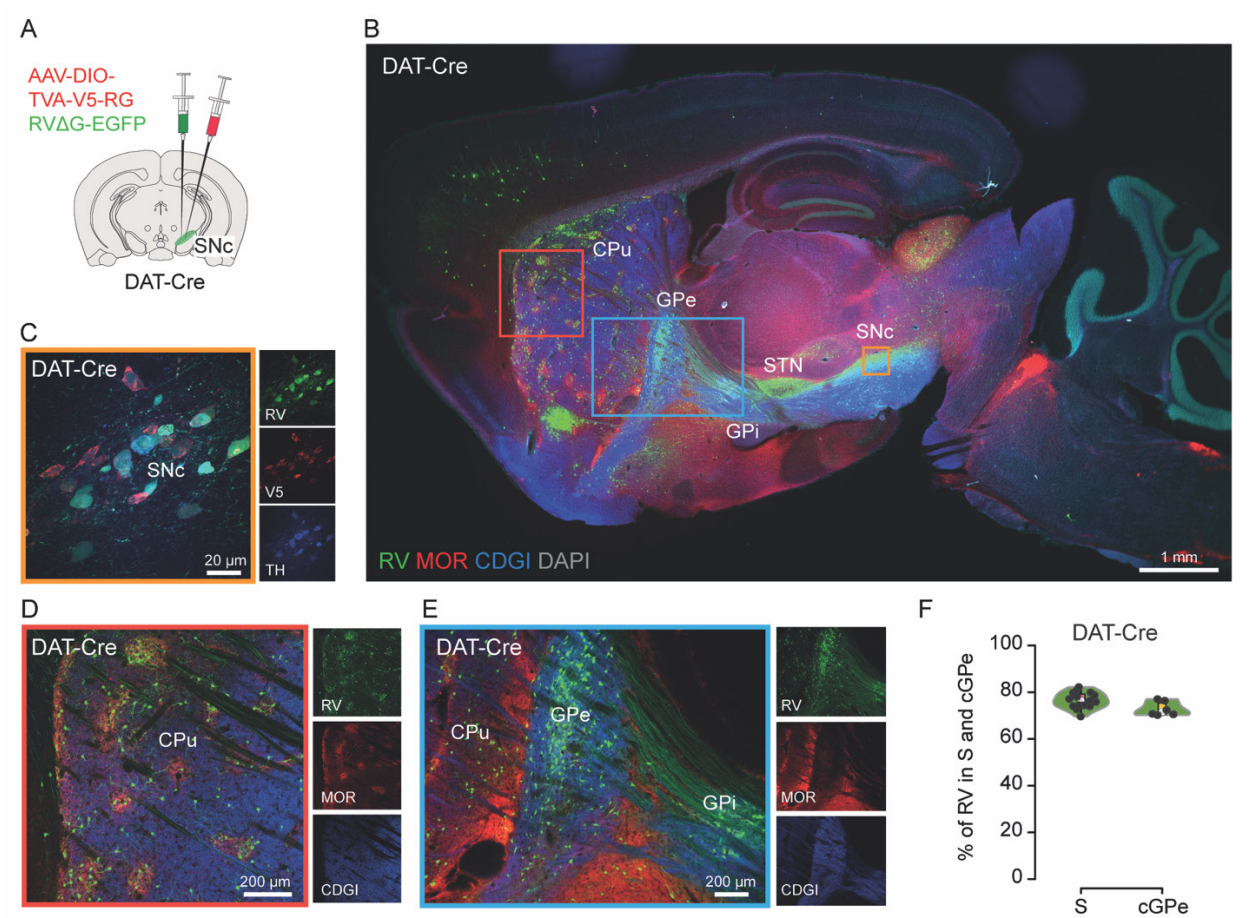

Figure. 2: Distribution of RVΔG-labeled neurons targeting DA neurons in SNpc.
A. Illustration of the injection site, Cre-dependent TVA-V5-RVG (V5) and EnvA-pseudotyped EGFP-expressing rabies virus (RV) were injected into the SNpc of DAT-Cre mice, 21 days apart.
B. Representative sagittal section depicting RV-EYFP labeled neurons counterstained with anti-MOR1 (striosome marker, red), anti-CDGI (matrix marker, blue) and DAPI (gray) staining. RV-EYFP labeled presynaptic neurons (green) are located preferentially in striosomes and cGPe.
C. SNpc injection site (orange box in B), depicting starter neurons co-expressing the RV (green), V5 (red) and tyrosine hydroxylase (TH, blue).
D. Striatal region (red box in B), showing that presynaptic neurons projecting to DA cells are localized preferentially in striosomes.
E. GPe region (blue box in B), showing that presynaptic neurons projecting to DA cells are localized preferentially in the central MOR1-rich/CDGI-poor zone.
F. f, Quantification of RV labeled neurons targeting DA neurons in the SNpc CPu: n = 1544 neurons / 15 sections / 4 DAT-cre, GPe: n = 658 neurons / 6 sections / 3 DAT-cre.

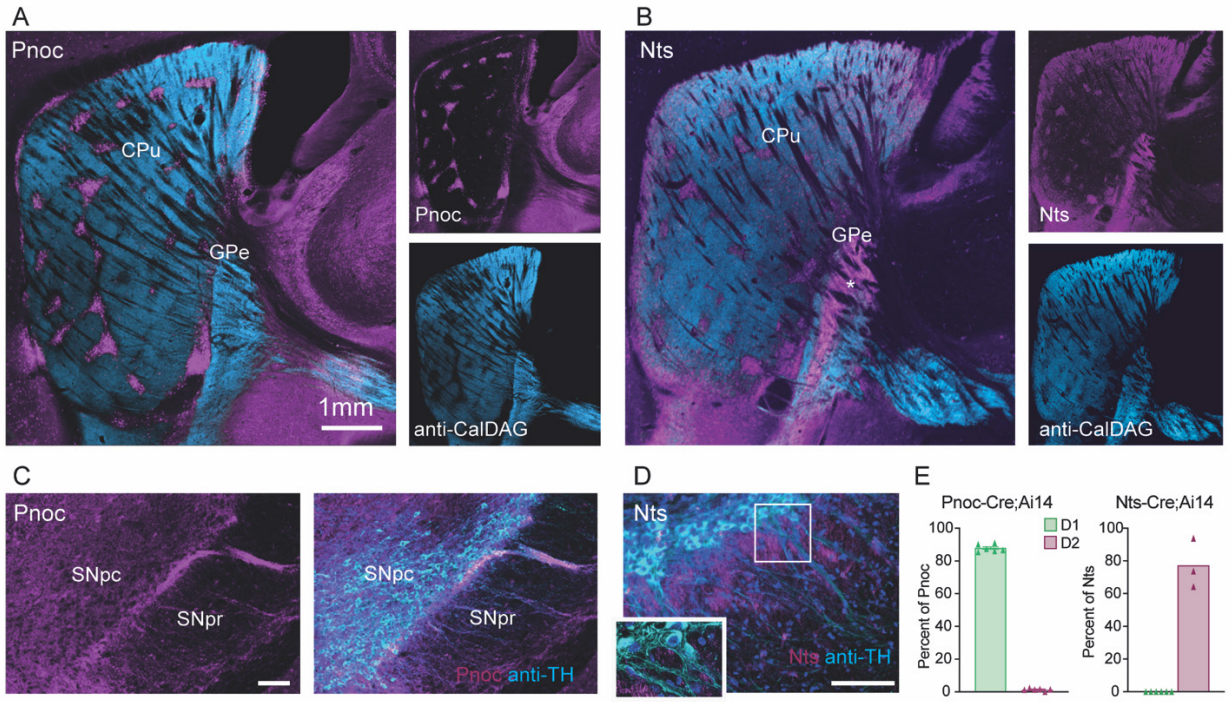

Figure. 3: Striosomal S-D1 and S-D2 populations form a parallel pathway to dopamine
A. Representative sagittal section from Pnoc-Cre;Ai14-tdTomato (magenta) transgenic mouse brain immunolabeled for CalDAG-GEFI (cyan).
B. Representative sagittal section from Nts-Cre;Ai14-tdTomato (magenta) transgenic mouse brain immunolabeled for CalDAG-GEFI (cyan).
C. Pnoc-Cre;Ai14 immunolabeled for the dopamine transporter (cyan, right column) to identify dopaminergic cell bodies and descending dendrites. labeling of the striosome dendron bouquet was found in all 4 mice used for cell counts.
D. Nts-Cre;Ai14 line F, immunolabeled for the dopamine transporter (cyan, right column) to identify dopaminergic cell bodies and descending dendrites. Lack of Nts-Cre;Ai14-tdTomato labeling of the striosome dendron bouquet was found in all 3 mice used for cell counts. Cell nuclei are stained with DAPI (blue). Scale bars are 1mm in A-D and 100 μm in C and D.
E. Plots showing the percent of striosome-marker positive sSPNs that are double-labeled for D1 or D2/A2a reporters in mice for striosome marker Pnoc-Cre;Ai14 and Nts-Cre. n = 4 for Pnoc-Cre;Ai14, n = 2 mice for Nts-Cre;Ai14;D1-GFP and n = 1 mouse for Nts-Cre;Ai14;D2-GFP. For each mouse, three coronal sections, taken from the anterior, mid-level and caudal regions, were evaluated. Counts were made only for cells within striosomes identified by MOR1.

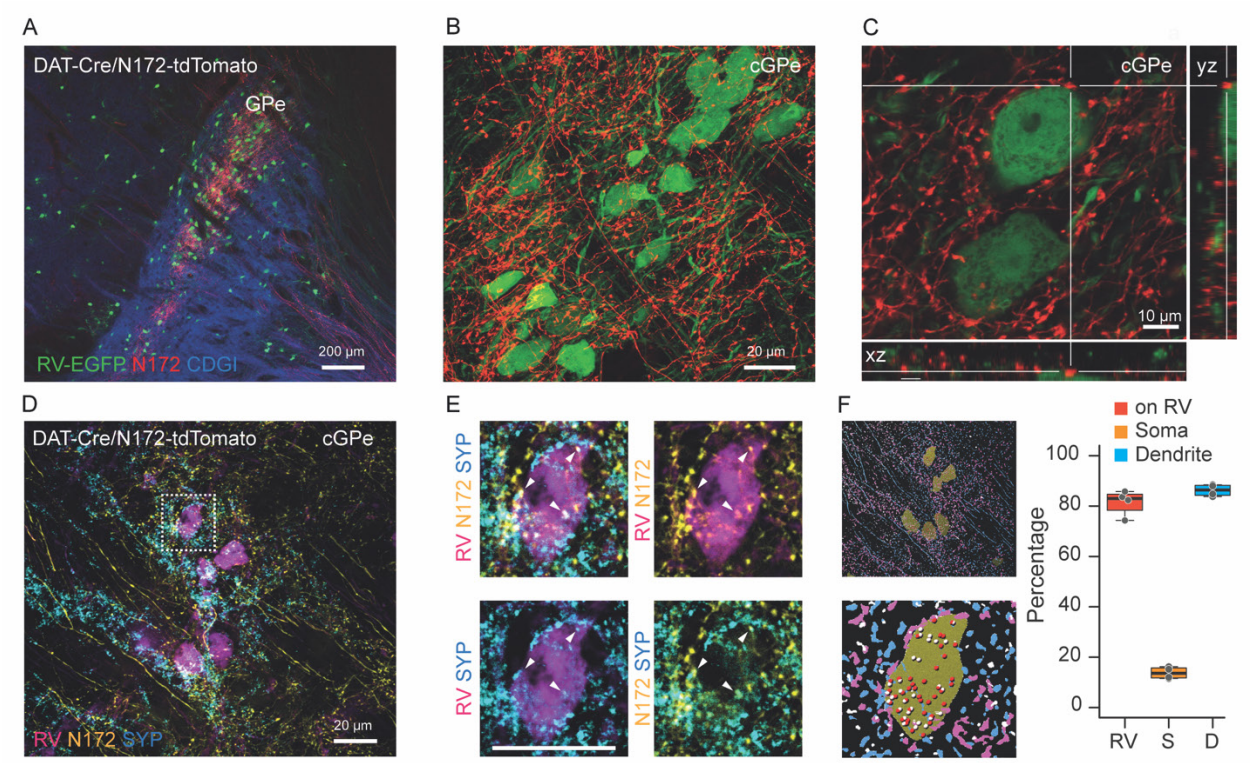

Figure. 4: Striosomal SPNs target DA-projecting cGPe neurons.

A. Terminals from striosomal N172-tdTomato neurons (red) on SNpc-DA-targeting cGPe neurons (RV-EGFP-labeled neurons, green).

B and C. Enlargements of cGPe depicting terminals from N172 striosomal neurons on SNpc-targeting cGPe neurons. xz and yz position of relevant Z-stack marked with white bars.

D. Representative image showing synaptophysin (SYP) positive (blue) N172 striosomal neuron terminals (yellow) on SNpc-targeting cGPe neurons (magenta).

E. Magnification of the indicated cell (square) in D.

F. Quantification of colocalized terminals. RV: percentage of N172+/SYP+ found on RV processes; S: percentage of N172+/SYP+/RV+ on cell body; D: percentage of N172+/SYP+/RV+ on dendrites.

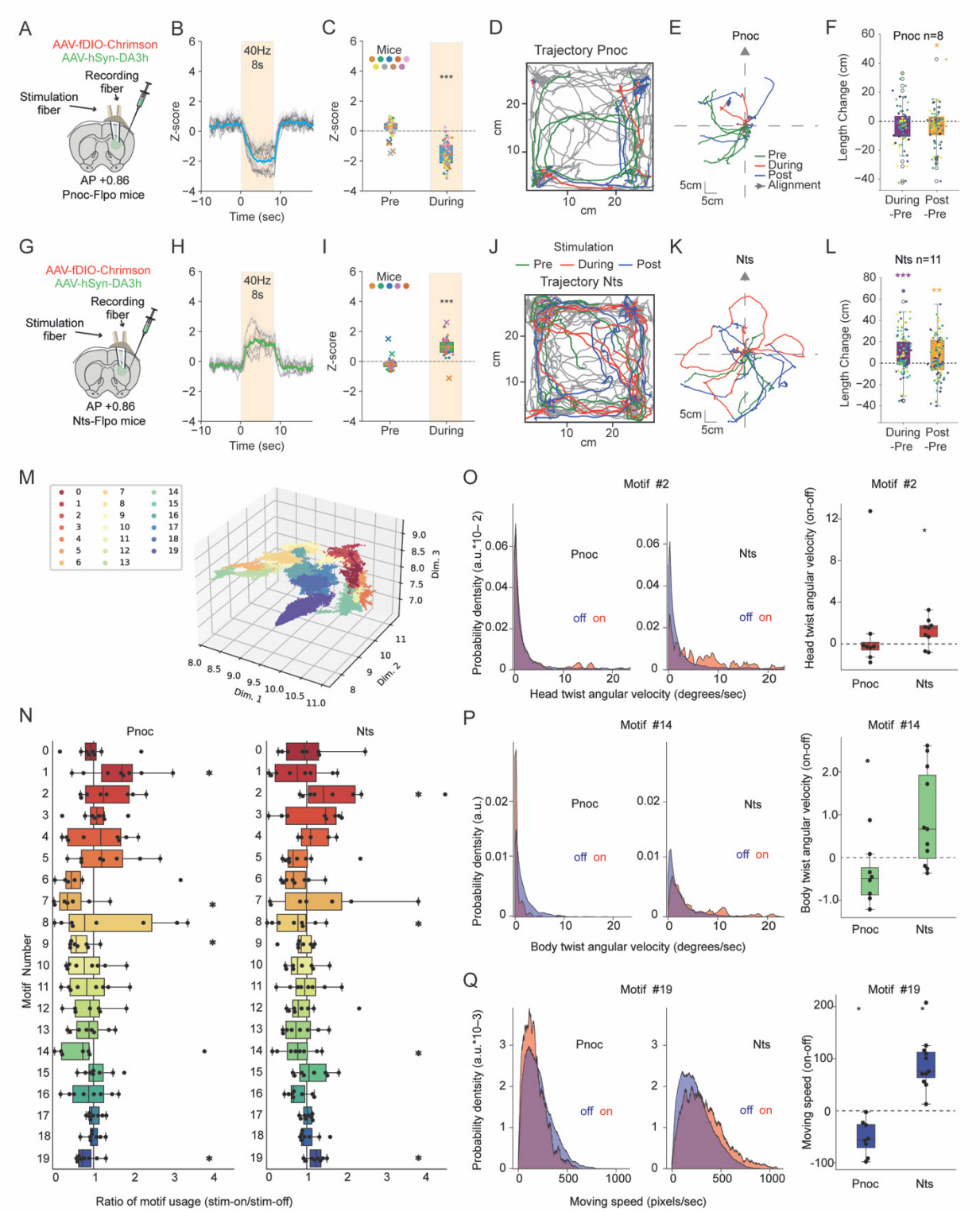

Figure 5. S-D1 S-D2 effects on dopamine release and motor kinematics.

A. Schematic of protocol for targeting S-D1 for optogenetic stimulation.

B. Average dopamine response to optogenetic stimulation (8sec train at 40Hz, 10 trials) of S-D1 (Pnoc) SPNs.

C. Average response before and during the stimulation of S-D1.
D. Behavioral effects of optogenetic manipulation of S-D1 SPNs in self-paced actions. Trajectory of mice in an open field box (14-14cm). The periods before, during and after the optogenetic stimulation are labeled with green, red and blue respectively.
E. Traces around the optogenetic stimulation for 10 trials reoriented to the direction of the base of the tail to the neck for S-D1 SPNs stimulation.
F. Difference of distance run during and after the optogenetic stimulation compared to the equivalent time period before the stimulation of S-D1 SPNs.
G. Schematic of protocol for targeting S-D2.
H. Average dopamine response to optogenetic stimulation (8sec train at 40Hz, 10 trials) of S-D2 (Nts) SPNs.
I. Average response before and during the stimulation of S-D2.
J. Behavioral effects of optogenetic manipulation of S-D2 SPNs in self-paced actions. Trajectory of mice in an open field box (14-14cm). The periods before, during and after the optogenetic stimulation are labeled with green, red and blue respectively.
K. Traces around the optogenetic stimulation for 10 trials reoriented to the direction of the base of the tail to the neck for S-D2 SPNs stimulation.
L. Difference of distance run during and after the optogenetic stimulation compared to the equivalent time period before the stimulation of S-D2 SPNs.
M. Visualization of behavioral motif clusters in three-dimensional space using UMAP. Twenty unique motifs were identified through the B-SOiD clustering analysis and are represented in a color-coded format, with each color representing a different behavioral motif cluster.
N. Box plots and swarm plots illustrating the ratio of motif usage between periods of stimulation-on and stimulation-off for each mouse. Average motif usage rates, measured in frames per second, were calculated separately for each condition and analyzed for statistical differences using a two-tailed t-test across different conditions (n = 8 for Pnoc, n = 11 for Nts; *$p < 0.05$).
O. (Left): Distribution density of head twist angular velocity, defined by the angle between the direction from the center of the body to the neck and from the neck to the snout. Data were aggregated from all mice and analyzed separately for periods of stimulation-on and stimulation-off. (Right): Box plots and swarm plots illustrating the ratio of average angular velocities during stimulation-on versus stimulation-off periods. These ratios were calculated for each mouse, and two conditions were statistically compared (n = 8 mice for Pnoc, n = 11 mice for Nts; *$p < 0.05$ by two-tailed t-test).
P. (Left): Distribution density of body twist angular velocity, calculated from the angle between the tail base to the center of the body and from the center of the body to the neck. (Right): Box plots and swarm plots compare the ratios of average angular velocities during stimulation-on versus stimulation-off periods for each mouse, and two conditions were statistically compared (n = 8 mice for Pnoc, n = 11 mice for Nts; *$p < 0.05$ by two-tailed t-test).
Q. (Left): Distribution density of moving speed, quantified by tracking the center of the body. (Right): Box plots and swarm plots of the ratio of average moving speeds during the stimulation-on versus stimulation-off periods for each mouse, and two conditions were statistically compared (n = 8 mice for Pnoc, n = 11 mice for Nts; *$p < 0.05$ by two-tailed t-test).

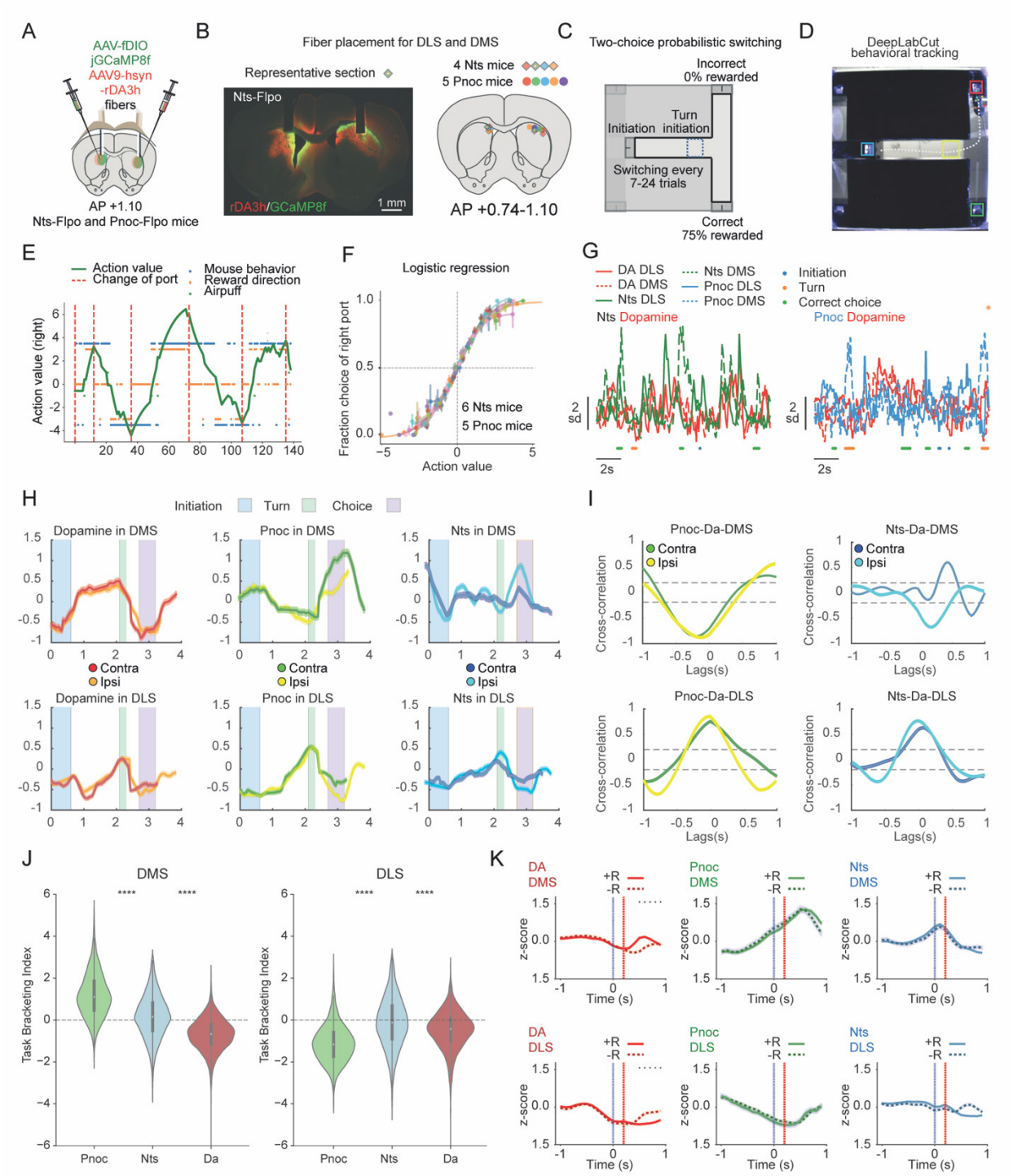

Figure. 6. Simultaneous imaging of dopamine (DA) release and S-D1 (Pnoc) or S-D2 (Nts) neuronal activity during a two-choice probabilistic switching task.

A. Overview of the approach for simultaneous imaging of DA release and neuronal activity in DMS and DLS.

B. A representative brain section showing fiber placement for simultaneous imaging of DA release and Nts neuron activity in the right DLS and left DMS.

C. Diagram of the Two-choice Probabilistic Switching Task, outlining the task structure.

D. A representative frame from behavior recording annotated with DeepLabCut (DLC)-based tracking, illustrating the analytical approach to movement tracking.
E. Example of mouse behavior in an expert session (blue circles) versus the fitted trial-by-trial Q-learning model (green trace). Dashed orange lines mark task switches, orange circles denote reward direction delivery, and blue circles indicate the actual choices made by mice. Example includes 140 trials.
F. The fraction of choices for the right port plotted against the relative action value (Q-learning), illustrating decision-making strategies.
G. Representative photometry traces showing activity of Nts, Pnoc, and DA during the task, capturing the dynamics of neuronal and neurotransmitter responses.
H. Temporal dynamics of Nts, Pnoc, and DA activity (average from all mice all sessions) during ipsilateral and contralateral choice trials in the DMS (upper) and DLS (lower) normalized for time. The shaded areas indicate the initiation, turn, and choice phases of the trial.
I. Cross-correlation analysis between Pnoc or Nts neuron activity and DA signaling in the DMS (upper) or DLS (lower). Pnoc (S-D1) and DA signals show an anticorrelated relationship with a prominent inverse peak for DMS and positive peak in DLS at a negative lag, suggesting dopamine fluctuations precede changes in S-D1 neuron firing rates by approximately 0.2 seconds.
Cross-correlation analysis between Nts (S-D2, right) neuron activity and DA signaling in the DMS and DLS, indicating a positive correlation for contralateral choice trials and for both ipsilateral and contralateral choice trials in DLS and a negative correlation with ipsilateral choice trials in DMS. Peaks in the Nts neuron activity lead the increases in DA levels in DLS and lags in the DMS, with a lag time of around 0.4 seconds.
J. Task bracketing index for Pnoc (S-D1), Nts (S-D2) and DA. Pnoc has a positive bracketing index in the DMS and negative in the DLS where DA has a negative bracketing index for both. No bracketing index found in Nts neuron activity.
K. Pnoc and Nts activity do not dissociate rewarded and unrewarded outcomes. DA shows a positive reward response only in the DMS.

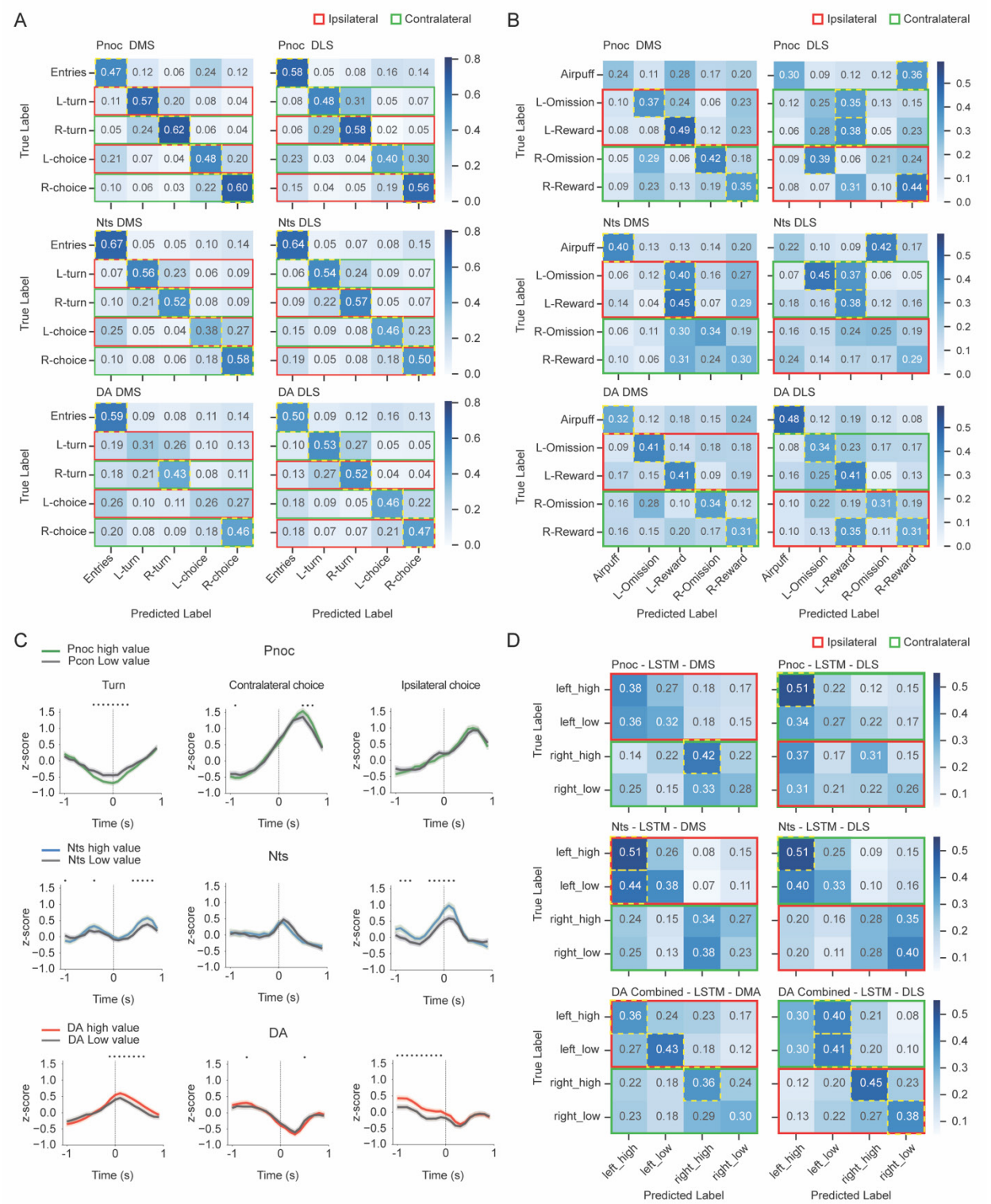

Figure 7: Classification performance of neural activity patterns in predicting task behaviors, reward outcomes, and action values across DMS and DLS and Pnoc (S-D1), Nts (S-D2) and dopamine signals

A: Confusion matrices show the accuracy of an LSTM model in classifying task space events: initiation, left turn, right turn, left choice, and right choice. The top row represents Pnoc, the middle

row represents Nts, and the bottom row represents dopamine. Each column represents different brain regions: DMS (left) and DLS (right). Red squares indicate ipsilateral events relative to the recording site, and green squares indicate contralateral events. Dashed yellow squares highlight task events identified with significantly higher accuracy than chance. Values are averaged across all animals. This panel demonstrates that, except for dopamine in the DMS, all signals show higher-than-chance accuracy for all task events (diagonal). Dopamine in the DMS shows significantly higher-than-chance accuracy for initiation and only for contralateral turn and choice events.

B: Confusion matrices showing the accuracy of an LSTM model in classifying outcomes at choice ports: air puff, left rewarded, left unrewarded, right rewarded, and right unrewarded. The same color coding and highlighting are used as in panel A. This panel demonstrates that dopamine provides the best performance, but overall accuracy is lower compared to task events classification in panel A.

C: Average signals of Pnoc, Nts, and dopamine during turn, contralateral choice, and ipsilateral choice, split by high and low action value trials as calculated with a Q-learning model. This panel demonstrates significant differences in amplitude at different time points between high and low value trials across all signals.

D: Confusion matrices using the same method and color coding as previous panels for classifying left high value choice, left low value choice, right high value choice, and right low value choice. This panel shows that the Pnoc (S-D1) signal in both DMS and DLS carries action value information only for high value contralateral actions. Nts (S-D2) shows poor separation of high and low value trials, and although dopamine contains value information, its accuracy is relatively low.

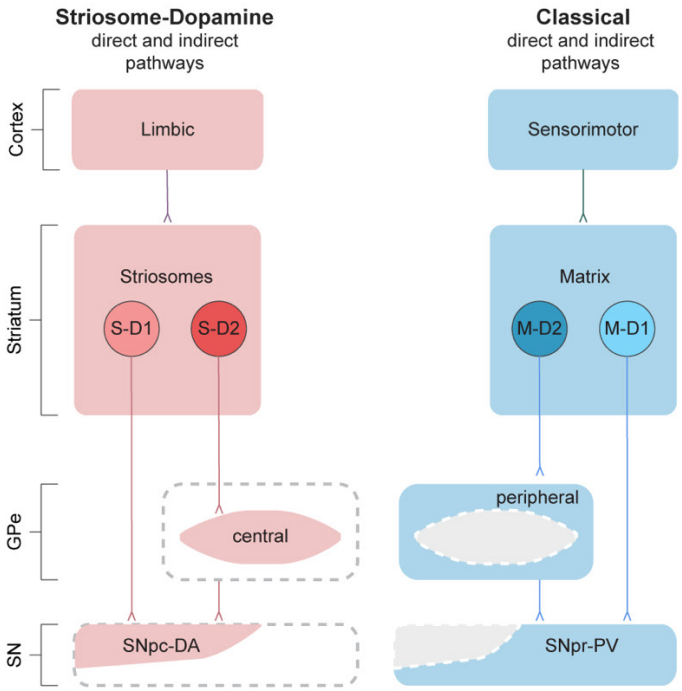

Figure. 8: [Model] Parallel pathway model for striatal output pathways.
The striosome and matrix compartments form parallel D1-direct and D2-indirect pathways to the SNpc and SNpr, respectively. SNpr-DA: substantia nigra pars reticulata parvalbumin positive neurons, SNpc: substantia nigra pars compacta dopaminergic neurons, GPe: external globus pallidus, S-D1: striosomal direct pathway, S-D2: striosomal indirect pathway, M-D1: matrix direct pathway, M-D2: matrix indirect pathway

References

1. Albin, R.L., Young, A.B., and Penney, J.B. (1989). The functional anatomy of basal ganglia disorders. Trends Neurosci. *12*, 366–375.

2. DeLong, M.R. (1990). Primate models of movement disorders of basal ganglia origin. Trends Neurosci. *13*, 281–285.

3. Crossman, A.R. (1989). Neural mechanisms in disorders of movement. Comp. Biochem. Physiol. A Comp. Physiol. *93*, 141–149.

4. Bateup, H.S., Santini, E., Shen, W., Birnbaum, S., Valjent, E., Surmeier, D.J., Fisone, G., Nestler, E.J., and Greengard, P. (2010). Distinct subclasses of medium spiny neurons differentially regulate striatal motor behaviors. Proc. Natl. Acad. Sci. U. S. A. *107*, 14845–14850.

5. Alexander, G.E., and Crutcher, M.D. (1990). Functional architecture of basal ganglia circuits: neural substrates of parallel processing. Trends Neurosci. *13*, 266–271.

6. Mink, J.W. (2003). The Basal Ganglia and involuntary movements: impaired inhibition of competing motor patterns. Arch. Neurol. *60*, 1365–1368.

7. Kawaguchi, Y., Wilson, C.J., and Emson, P.C. (1990). Projection subtypes of rat neostriatal matrix cells revealed by intracellular injection of biocytin. J. Neurosci. *10*, 3421–3438.

8. Oldenburg, I.A., and Sabatini, B.L. (2015). Antagonistic but Not Symmetric Regulation of Primary Motor Cortex by Basal Ganglia Direct and Indirect Pathways. Neuron *86*, 1174–1181.

9. Nishi, A., Snyder, G.L., and Greengard, P. (1997). Bidirectional regulation of DARPP-32 phosphorylation by dopamine. J. Neurosci. *17*, 8147–8155.

10. Greengard, P., Allen, P.B., and Nairn, A.C. (1999). Beyond the dopamine receptor: the DARPP-32/protein phosphatase-1 cascade. Neuron *23*, 435–447.

11. Gerfen, C.R., Engber, T.M., Mahan, L.C., Susel, Z., Chase, T.N., Monsma, F.J., Jr, and Sibley, D.R. (1990). D1 and D2 dopamine receptor-regulated gene expression of striatonigral and striatopallidal neurons. Science *250*, 1429–1432.

12. Mink, J.W., and Thach, W.T. (1991). Basal ganglia motor control. III. Pallidal ablation: normal reaction time, muscle cocontraction, and slow movement. J. Neurophysiol. *65*, 330–351.

13. Mink, J.W. (1996). The basal ganglia: focused selection and inhibition of competing motor programs. Prog. Neurobiol. *50*, 381–425.

14. Nambu, A., Tokuno, H., Hamada, I., Kita, H., Imanishi, M., Akazawa, T., Ikeuchi, Y., and Hasegawa, N. (2000). Excitatory cortical inputs to pallidal neurons via the subthalamic nucleus in the monkey. J. Neurophysiol. *84*, 289–300.

15. Hikosaka, O., Takikawa, Y., and Kawagoe, R. (2000). Role of the basal ganglia in the

control of purposive saccadic eye movements. Physiol. Rev. *80*, 953–978.

16. Vicente, A.M., Galvão-Ferreira, P., Tecuapetla, F., and Costa, R.M. (2016). Direct and indirect dorsolateral striatum pathways reinforce different action strategies. Curr. Biol. *26*, R267–R269.

17. Isomura, Y., Takekawa, T., Harukuni, R., Handa, T., Aizawa, H., Takada, M., and Fukai, T. (2013). Reward-modulated motor information in identified striatum neurons. J. Neurosci. *33*, 10209–10220.

18. Cui, G., Jun, S.B., Jin, X., Pham, M.D., Vogel, S.S., Lovinger, D.M., and Costa, R.M. (2013). Concurrent activation of striatal direct and indirect pathways during action initiation. Nature *494*, 238–242.

19. Surmeier, D.J., Mercer, J.N., and Chan, C.S. (2005). Autonomous pacemakers in the basal ganglia: who needs excitatory synapses anyway? Curr. Opin. Neurobiol. *15*, 312–318.

20. Gatev, P., Darbin, O., and Wichmann, T. (2006). Oscillations in the basal ganglia under normal conditions and in movement disorders. Mov. Disord. *21*, 1566–1577.

21. Okamoto, S., Sohn, J., Tanaka, T., Takahashi, M., Ishida, Y., Yamauchi, K., Koike, M., Fujiyama, F., and Hioki, H. (2020). Overlapping Projections of Neighboring Direct and Indirect Pathway Neostriatal Neurons to Globus Pallidus External Segment. iScience *23*, 101409.

22. Parent, A., Sato, F., Wu, Y., Gauthier, J., Lévesque, M., and Parent, M. (2000). Organization of the basal ganglia: the importance of axonal collateralization. Trends Neurosci. *23*, S20–S27.

23. Graybiel, A.M., and Ragsdale, C.W., Jr (1978). Histochemically distinct compartments in the striatum of human, monkeys, and cat demonstrated by acetylthiocholinesterase staining. Proc. Natl. Acad. Sci. U. S. A. *75*, 5723–5726.

24. Wallace, M.L., Saunders, A., Huang, K.W., Philson, A.C., Goldman, M., Macosko, E.Z., McCarroll, S.A., and Sabatini, B.L. (2017). Genetically Distinct Parallel Pathways in the Entopeduncular Nucleus for Limbic and Sensorimotor Output of the Basal Ganglia. Neuron *94*, 138–152.e5.

25. Courtney, C.D., Pamukcu, A., and Chan, C.S. (2023). Cell and circuit complexity of the external globus pallidus. Nat. Neurosci. *26*, 1147–1159.

26. Mallet, N., Micklem, B.R., Henny, P., Brown, M.T., Williams, C., Bolam, J.P., Nakamura, K.C., and Magill, P.J. (2012). Dichotomous organization of the external globus pallidus. Neuron *74*, 1075–1086.

27. Lilascharoen, V., Wang, E.H.-J., Do, N., Pate, S.C., Tran, A.N., Yoon, C.D., Choi, J.-H., Wang, X.-Y., Pribiag, H., Park, Y.-G., et al. (2021). Divergent pallidal pathways underlying distinct Parkinsonian behavioral deficits. Nat. Neurosci. *24*, 504–515.

28. Mastro, K.J., Bouchard, R.S., Holt, H.A.K., and Gittis, A.H. (2014). Transgenic mouse lines subdivide external segment of the globus pallidus (GPe) neurons and reveal distinct GPe output pathways. J. Neurosci. *34*, 2087–2099.

29. Dong, J., Hawes, S., Wu, J., Le, W., and Cai, H. (2021). Connectivity and Functionality of the Globus Pallidus Externa Under Normal Conditions and Parkinson's Disease. Front. Neural Circuits *15*, 645287.

30. Wickersham, I.R., Lyon, D.C., Barnard, R.J.O., Mori, T., Finke, S., Conzelmann, K.-K., Young, J.A.T., and Callaway, E.M. (2007). Monosynaptic restriction of transsynaptic tracing from single, genetically targeted neurons. Neuron *53*, 639–647.

31. Ährlund-Richter, S., Xuan, Y., van Lunteren, J.A., Kim, H., Ortiz, C., Pollak Dorocic, I., Meletis, K., and Carlén, M. (2019). A whole-brain atlas of monosynaptic input targeting four different cell types in the medial prefrontal cortex of the mouse. Nat. Neurosci. *22*, 657–668.

32. Lazaridis, I., Tzortzi, O., Weglage, M., Märtin, A., Xuan, Y., Parent, M., Johansson, Y., Fuzik, J., Fürth, D., Fenno, L.E., et al. (2019). A hypothalamus-habenula circuit controls aversion. Mol. Psychiatry *24*, 1351–1368.

33. Kita, H., and Kitai, S.T. (1994). The morphology of globus pallidus projection neurons in the rat: an intracellular staining study. Brain Res. *636*, 308–319.

34. Fujiyama, F., Nakano, T., Matsuda, W., Furuta, T., Udagawa, J., and Kaneko, T. (2016). A single-neuron tracing study of arkypallidal and prototypic neurons in healthy rats. Brain Struct. Funct. *221*, 4733–4740.

35. Oh, Y.-M., Karube, F., Takahashi, S., Kobayashi, K., Takada, M., Uchigashima, M., Watanabe, M., Nishizawa, K., Kobayashi, K., and Fujiyama, F. (2017). Using a novel PV-Cre rat model to characterize pallidonigral cells and their terminations. Brain Struct. Funct. *222*, 2359–2378.

36. Celada, P., Paladini, C.A., and Tepper, J.M. (1999). GABAergic control of rat substantia nigra dopaminergic neurons: role of globus pallidus and substantia nigra pars reticulata. Neuroscience *89*, 813–825.

37. Chang, H.T., Wilson, C.J., and Kitai, S.T. (1981). Single neostriatal efferent axons in the globus pallidus: a light and electron microscopic study. Science *213*, 915–918.

38. Wu, Y., Richard, S., and Parent, A. (2000). The organization of the striatal output system: a single-cell juxtacellular labeling study in the rat. Neurosci. Res. *38*, 49–62.

39. Lévesque, M., and Parent, A. (2005). The striatofugal fiber system in primates: a reevaluation of its organization based on single-axon tracing studies. Proc. Natl. Acad. Sci. U. S. A. *102*, 11888–11893.

40. Fujiyama, F., Sohn, J., Nakano, T., Furuta, T., Nakamura, K.C., Matsuda, W., and Kaneko, T. (2011). Exclusive and common targets of neostriatofugal projections of rat striosome neurons: a single neuron-tracing study using a viral vector. Eur. J. Neurosci. *33*, 668–677.

41. Labouesse, M.A., Torres-Herraez, A., Chohan, M.O., Villarin, J.M., Greenwald, J., Sun, X., Zahran, M., Tang, A., Lam, S., Veenstra-VanderWeele, J., et al. (2023). A non-canonical striatopallidal Go pathway that supports motor control. Nat. Commun. *14*, 6712.

42. Crittenden, J.R., Tillberg, P.W., Riad, M.H., Shima, Y., Gerfen, C.R., Curry, J., Housman,

D.E., Nelson, S.B., Boyden, E.S., and Graybiel, A.M. (2016). Striosome-dendron bouquets highlight a unique striatonigral circuit targeting dopamine-containing neurons. Proc. Natl. Acad. Sci. U. S. A. *113*, 11318–11323.

43. Gong, S., Zheng, C., Doughty, M.L., Losos, K., Didkovsky, N., Schambra, U.B., Nowak, N.J., Joyner, A., Leblanc, G., Hatten, M.E., et al. (2003). A gene expression atlas of the central nervous system based on bacterial artificial chromosomes. Nature *425*, 917–925.

44. Shima, Y., Sugino, K., Hempel, C.M., Shima, M., Taneja, P., Bullis, J.B., Mehta, S., Lois, C., and Nelson, S.B. (2016). A Mammalian enhancer trap resource for discovering and manipulating neuronal cell types. Elife *5*, e13503.

45. Erbs, E., Faget, L., Scherrer, G., Matifas, A., Filliol, D., Vonesch, J.-L., Koch, M., Kessler, P., Hentsch, D., Birling, M.-C., et al. (2015). A mu-delta opioid receptor brain atlas reveals neuronal co-occurrence in subcortical networks. Brain Struct. Funct. *220*, 677–702.

46. Parker, K.E., Pedersen, C.E., Gomez, A.M., Spangler, S.M., Walicki, M.C., Feng, S.Y., Stewart, S.L., Otis, J.M., Al-Hasani, R., McCall, J.G., et al. (2019). A Paranigral VTA Nociceptin Circuit that Constrains Motivation for Reward. Cell *178*, 653–671.e19.

47. Leinninger, G.M., Opland, D.M., Jo, Y.-H., Faouzi, M., Christensen, L., Cappellucci, L.A., Rhodes, C.J., Gnegy, M.E., Becker, J.B., Pothos, E.N., et al. (2011). Leptin action via neurotensin neurons controls orexin, the mesolimbic dopamine system and energy balance. Cell Metab. *14*, 313–323.

48. Madisen, L., Zwingman, T.A., Sunkin, S.M., Oh, S.W., Zariwala, H.A., Gu, H., Ng, L.L., Palmiter, R.D., Hawrylycz, M.J., Jones, A.R., et al. (2010). A robust and high-throughput Cre reporting and characterization system for the whole mouse brain. Nat. Neurosci. *13*, 133–140.

49. Kawasaki, H., Springett, G.M., Toki, S., Canales, J.J., Harlan, P., Blumenstiel, J.P., Chen, E.J., Bany, I.A., Mochizuki, N., Ashbacher, A., et al. (1998). A Rap guanine nucleotide exchange factor enriched highly in the basal ganglia. Proc. Natl. Acad. Sci. U. S. A. *95*, 13278–13283.

50. Crittenden, J.R., Dunn, D.E., Merali, F.I., Woodman, B., Yim, M., Borkowska, A.E., Frosch, M.P., Bates, G.P., Housman, D.E., Lo, D.C., et al. (2010). CalDAG-GEFI down-regulation in the striatum as a neuroprotective change in Huntington's disease. Hum. Mol. Genet. *19*, 1756–1765.

51. Gerfen, C.R., Paletzki, R., and Heintz, N. (2013). GENSAT BAC cre-recombinase driver lines to study the functional organization of cerebral cortical and basal ganglia circuits. Neuron *80*, 1368–1383.

52. Liu, F.C., and Graybiel, A.M. (1992). Heterogeneous development of calbindin-D28K expression in the striatal matrix. J. Comp. Neurol. *320*, 304–322.

53. Sgobio, C., Wu, J., Zheng, W., Chen, X., Pan, J., Salinas, A.G., Davis, M.I., Lovinger, D.M., and Cai, H. (2017). Aldehyde dehydrogenase 1-positive nigrostriatal dopaminergic fibers exhibit distinct projection pattern and dopamine release dynamics at mouse dorsal striatum. Sci. Rep. *7*, 5283.

54. Azcorra, M., Gaertner, Z., Davidson, C., He, Q., Kim, H., Nagappan, S., Hayes, C.K., Ramakrishnan, C., Fenno, L., Kim, Y.S., et al. (2023). Unique functional responses differentially map onto genetic subtypes of dopamine neurons. Nat. Neurosci. *26*, 1762–1774.

55. Kita, H., and Kita, T. (2001). Number, origins, and chemical types of rat pallidostriatal projection neurons. J. Comp. Neurol. *437*, 438–448.

56. Miyamoto, Y., Katayama, S., Shigematsu, N., Nishi, A., and Fukuda, T. (2018). Striosome-based map of the mouse striatum that is conformable to both cortical afferent topography and uneven distributions of dopamine D1 and D2 receptor-expressing cells. Brain Struct. Funct. *223*, 4275–4291.

57. Smith, Y., and Bolam, J.P. (1989). Neurons of the substantia nigra reticulata receive a dense GABA-containing input from the globus pallidus in the rat. Brain Res. *493*, 160–167.

58. Connelly, W.M., Schulz, J.M., Lees, G., and Reynolds, J.N.J. (2010). Differential short-term plasticity at convergent inhibitory synapses to the substantia nigra pars reticulata. J. Neurosci. *30*, 14854–14861.

59. Hegeman, D.J., Hong, E.S., Hernández, V.M., and Chan, C.S. (2016). The external globus pallidus: progress and perspectives. Eur. J. Neurosci. *43*, 1239–1265.

60. Saunders, A., Macosko, E.Z., Wysoker, A., Goldman, M., Krienen, F.M., de Rivera, H., Bien, E., Baum, M., Bortolin, L., Wang, S., et al. (2018). Molecular Diversity and Specializations among the Cells of the Adult Mouse Brain. Cell *174*, 1015–1030.e16.

61. Wu, B., Zhang, S., Guo, Z., Wang, G., Zhang, G., Xie, L., Lou, J., Chen, X., Wu, D., Bergmeier, W., et al. (2018). RAS P21 Protein Activator 3 (RASA3) Specifically Promotes Pathogenic T Helper 17 Cell Generation by Repressing T-Helper-2-Cell-Biased Programs. Immunity *49*, 886–898.e5.

62. Johansen, K.H., Golec, D.P., Okkenhaug, K., and Schwartzberg, P.L. (2023). Mind the GAP: RASA2 and RASA3 GTPase-activating proteins as gatekeepers of T cell activation and adhesion. Trends Immunol. *44*, 917–931.

63. Johansen, K.H., Golec, D.P., Huang, B., Park, C., Thomsen, J.H., Preite, S., Cannons, J.L., Garçon, F., Schrom, E.C., Courrèges, C.J.F., et al. (2022). A CRISPR screen targeting PI3K effectors identifies RASA3 as a negative regulator of LFA-1-mediated adhesion in T cells. Sci. Signal. *15*, eabl9169.

64. Kubota, Y., Liu, J., Hu, D., DeCoteau, W.E., Eden, U.T., Smith, A.C., and Graybiel, A.M. (2009). Stable encoding of task structure coexists with flexible coding of task events in sensorimotor striatum. J. Neurophysiol. *102*, 2142–2160.

65. Friedman, A., Hueske, E., Drammis, S.M., Toro Arana, S.E., Nelson, E.D., Carter, C.W., Delcasso, S., Rodriguez, R.X., Lutwak, H., DiMarco, K.S., et al. (2020). Striosomes Mediate Value-Based Learning Vulnerable in Age and a Huntington's Disease Model. Cell *183*, 918–934.e49.

66. Amemori, S., Graybiel, A.M., and Amemori, K.-I. (2021). Causal Evidence for Induction of Pessimistic Decision-Making in Primates by the Network of Frontal Cortex and Striosomes.

Front. Neurosci. *15*, 649167.

67. Amemori, S., Amemori, K.-I., Yoshida, T., Papageorgiou, G.K., Xu, R., Shimazu, H., Desimone, R., and Graybiel, A.M. (2020). Microstimulation of primate neocortex targeting striosomes induces negative decision-making. Eur. J. Neurosci. *51*, 731–741.

68. Friedman, A., Homma, D., Bloem, B., Gibb, L.G., Amemori, K.-I., Hu, D., Delcasso, S., Truong, T.F., Yang, J., Hood, A.S., et al. (2017). Chronic Stress Alters Striosome-Circuit Dynamics, Leading to Aberrant Decision-Making. Cell *171*, 1191–1205.e28.

69. Friedman, A., Homma, D., Gibb, L.G., Amemori, K.-I., Rubin, S.J., Hood, A.S., Riad, M.H., and Graybiel, A.M. (2015). A Corticostriatal Path Targeting Striosomes Controls Decision-Making under Conflict. Cell *161*, 1320–1333.

70. Graybiel, A.M. (2008). Habits, rituals, and the evaluative brain. Annu. Rev. Neurosci. *31*, 359–387.

71. Graybiel, A.M., and Matsushima, A. (2023). Striosomes and Matrisomes: Scaffolds for Dynamic Coupling of Volition and Action. Annu. Rev. Neurosci. *46*, 359–380.

72. Hong, S., and Hikosaka, O. (2008). The globus pallidus sends reward-related signals to the lateral habenula. Neuron *60*, 720–729.

73. Hikosaka, O. (2010). The habenula: from stress evasion to value-based decision-making. Nat. Rev. Neurosci. *11*, 503–513.

74. Matsumoto, M., and Hikosaka, O. (2007). Lateral habenula as a source of negative reward signals in dopamine neurons. Nature *447*, 1111–1115.

75. Matsumoto, M., and Hikosaka, O. (2009). Two types of dopamine neuron distinctly convey positive and negative motivational signals. Nature *459*, 837–841.

76. Steinberg, E.E., Gore, F., Heifets, B.D., Taylor, M.D., Norville, Z.C., Beier, K.T., Földy, C., Lerner, T.N., Luo, L., Deisseroth, K., et al. (2020). Amygdala-Midbrain Connections Modulate Appetitive and Aversive Learning. Neuron *106*, 1026–1043.e9.

77. Menegas, W., Akiti, K., Amo, R., Uchida, N., and Watabe-Uchida, M. (2018). Dopamine neurons projecting to the posterior striatum reinforce avoidance of threatening stimuli. Nat. Neurosci. *21*, 1421–1430.

78. Hong, S., Amemori, S., Chung, E., Gibson, D.J., Amemori, K.-I., and Graybiel, A.M. (2019). Predominant Striatal Input to the Lateral Habenula in Macaques Comes from Striosomes. Curr. Biol. *29*, 51–61.e5.

79. Rajakumar, N., Elisevich, K., and Flumerfelt, B.A. (1993). Compartmental origin of the striato-entopeduncular projection in the rat. J. Comp. Neurol. *331*, 286–296.

80. McGregor, M.M., McKinsey, G.L., Girasole, A.E., Bair-Marshall, C.J., Rubenstein, J.L.R., and Nelson, A.B. (2019). Functionally Distinct Connectivity of Developmentally Targeted Striosome Neurons. Cell Rep. *29*, 1419–1428.e5.

81. Yin, H.H., Mulcare, S.P., Hilário, M.R.F., Clouse, E., Holloway, T., Davis, M.I., Hansson, A.C., Lovinger, D.M., and Costa, R.M. (2009). Dynamic reorganization of striatal circuits

during the acquisition and consolidation of a skill. Nat. Neurosci. *12*, 333–341.

82. Lerner, T.N., Shilyansky, C., Davidson, T.J., Evans, K.E., Beier, K.T., Zalocusky, K.A., Crow, A.K., Malenka, R.C., Luo, L., Tomer, R., et al. (2015). Intact-Brain Analyses Reveal Distinct Information Carried by SNc Dopamine Subcircuits. Cell *162*, 635–647.

83. Lee, J., Wang, W., and Sabatini, B.L. (2020). Anatomically segregated basal ganglia pathways allow parallel behavioral modulation. Nat. Neurosci. *23*, 1388–1398.

84. van Elzelingen, W., Warnaar, P., Matos, J., Bastet, W., Jonkman, R., Smulders, D., Goedhoop, J., Denys, D., Arbab, T., and Willuhn, I. (2022). Striatal dopamine signals are region specific and temporally stable across action-sequence habit formation. Curr. Biol. *32*, 1163–1174.e6.

85. Mohebi, A., Wei, W., Pelattini, L., Kim, K., and Berke, J.D. (2024). Dopamine transients follow a striatal gradient of reward time horizons. Nat. Neurosci. *27*, 737–746.

86. Ambrosi, P., and Lerner, T.N. (2022). Striatonigrostriatal circuit architecture for disinhibition of dopamine signaling. Cell Rep. *40*, 111228.

87. Dhawale, A.K., Wolff, S.B.E., Ko, R., and Ölveczky, B.P. (2021). The basal ganglia control the detailed kinematics of learned motor skills. Nat. Neurosci. *24*, 1256–1269.

88. Muñoz, B., Fritz, B.M., Yin, F., and Atwood, B.K. (2018). Alcohol exposure disrupts mu opioid receptor-mediated long-term depression at insular cortex inputs to dorsolateral striatum. Nat. Commun. *9*, 1318.

89. Hilario, M., Holloway, T., Jin, X., and Costa, R.M. (2012). Different dorsal striatum circuits mediate action discrimination and action generalization. Eur. J. Neurosci. *35*, 1105–1114.

90. Dexter, D.T., Carayon, A., Javoy-Agid, F., Agid, Y., Wells, F.R., Daniel, S.E., Lees, A.J., Jenner, P., and Marsden, C.D. (1991). Alterations in the levels of iron, ferritin and other trace metals in Parkinson's disease and other neurodegenerative diseases affecting the basal ganglia. Brain *114 (Pt 4)*, 1953–1975.

91. Marsden, C.D. (1982). Basal ganglia disease. Lancet *2*, 1141–1147.

92. Gerfen, C.R., and Surmeier, D.J. (2011). Modulation of striatal projection systems by dopamine. Annu. Rev. Neurosci. *34*, 441–466.

93. Howes, O.D., and Kapur, S. (2009). The dopamine hypothesis of schizophrenia: version III--the final common pathway. Schizophr. Bull. *35*, 549–562.

94. Brisch, R., Saniotis, A., Wolf, R., Bielau, H., Bernstein, H.-G., Steiner, J., Bogerts, B., Braun, K., Jankowski, Z., Kumaratilake, J., et al. (2014). The role of dopamine in schizophrenia from a neurobiological and evolutionary perspective: old fashioned, but still in vogue. Front. Psychiatry *5*, 47.

95. Menon, V., Palaniyappan, L., and Supekar, K. (2023). Integrative Brain Network and Salience Models of Psychopathology and Cognitive Dysfunction in Schizophrenia. Biol. Psychiatry *94*, 108–120.

96. Kegeles, L.S., Abi-Dargham, A., Frankle, W.G., Gil, R., Cooper, T.B., Slifstein, M., Hwang,

D.-R., Huang, Y., Haber, S.N., and Laruelle, M. (2010). Increased synaptic dopamine function in associative regions of the striatum in schizophrenia. Arch. Gen. Psychiatry *67*, 231–239.

97. Abi-Dargham, A., Rodenhiser, J., Printz, D., Zea-Ponce, Y., Gil, R., Kegeles, L.S., Weiss, R., Cooper, T.B., Mann, J.J., Van Heertum, R.L., et al. (2000). Increased baseline occupancy of D2 receptors by dopamine in schizophrenia. Proc. Natl. Acad. Sci. U. S. A. *97*, 8104–8109.

98. Piantadosi, S.C., Manning, E.E., Chamberlain, B.L., Hyde, J., LaPalombara, Z., Bannon, N.M., Pierson, J.L., K Namboodiri, V.M., and Ahmari, S.E. (2024). Hyperactivity of indirect pathway-projecting spiny projection neurons promotes compulsive behavior. Nat. Commun. *15*, 4434.

99. Packard, M.G., and Knowlton, B.J. (2002). Learning and memory functions of the Basal Ganglia. Annu. Rev. Neurosci. *25*, 563–593.

100. Schultz, W. (2016). Dopamine reward prediction-error signalling: a two-component response. Nat. Rev. Neurosci. *17*, 183–195.

101. Liljeholm, M., and O'Doherty, J.P. (2012). Contributions of the striatum to learning, motivation, and performance: an associative account. Trends Cogn. Sci. *16*, 467–475.

102. Crittenden, J.R., Yoshida, T., Venu, S., Mahar, A., and Graybiel, A.M. (2022). Cannabinoid Receptor 1 Is Required for Neurodevelopment of Striosome-Dendron Bouquets. eNeuro *9*. 10.1523/ENEURO.0318-21.2022.

103. Gittis, A.H., and Kreitzer, A.C. (2012). Striatal microcircuitry and movement disorders. Trends Neurosci. *35*, 557–564.

104. Assous, M., Kaminer, J., Shah, F., Garg, A., Koós, T., and Tepper, J.M. (2017). Differential processing of thalamic information via distinct striatal interneuron circuits. Nat. Commun. *8*, 15860.

105. Matsushima, A., and Graybiel, A.M. (2022). Combinatorial Developmental Controls on Striatonigral Circuits. Cell Rep. *38*, 110272.

106. Evans, R.C., Twedell, E.L., Zhu, M., Ascencio, J., Zhang, R., and Khaliq, Z.M. (2020). Functional Dissection of Basal Ganglia Inhibitory Inputs onto Substantia Nigra Dopaminergic Neurons. Cell Rep. *32*, 108156.

107. Graybiel, A.M., Moratalla, R., and Robertson, H.A. (1990). Amphetamine and cocaine induce drug-specific activation of the c-fos gene in striosome-matrix compartments and limbic subdivisions of the striatum. Proc. Natl. Acad. Sci. U. S. A. *87*, 6912–6916.

108. Moratalla, R., Vallejo, M., Elibol, B., and Graybiel, A.M. (1996). D1-class dopamine receptors influence cocaine-induced persistent expression of Fos-related proteins in striatum. Neuroreport *8*, 1–5.

109. Canales, J.J., and Graybiel, A.M. (2000). Patterns of gene expression and behavior induced by chronic dopamine treatments. Ann. Neurol. *47*, S53–S59.

110. Moratalla, R., Vickers, E.A., Robertson, H.A., Cochran, B.H., and Graybiel, A.M. (1993).

Coordinate expression of c-fos and jun B is induced in the rat striatum by cocaine. J. Neurosci. *13*, 423–433.

111. Wang, W., Xie, X., Zhuang, X., Huang, Y., Tan, T., Gangal, H., Huang, Z., Purvines, W., Wang, X., Stefanov, A., et al. (2023). Striatal μ-opioid receptor activation triggers direct-pathway GABAergic plasticity and induces negative affect. Cell Rep. *42*, 112089.

112. Davis, M.I., Crittenden, J.R., Feng, A.Y., Kupferschmidt, D.A., Naydenov, A., Stella, N., Graybiel, A.M., and Lovinger, D.M. (2018). The cannabinoid-1 receptor is abundantly expressed in striatal striosomes and striosome-dendron bouquets of the substantia nigra. PLoS One *13*, e0191436.

113. Seeman, P., and Lee, T. (1975). Antipsychotic drugs: direct correlation between clinical potency and presynaptic action on dopamine neurons. Science *188*, 1217–1219.

114. Creese, I., Burt, D.R., and Snyder, S.H. (1996). Dopamine receptor binding predicts clinical and pharmacological potencies of antischizophrenic drugs. J. Neuropsychiatry Clin. Neurosci. *8*, 223–226.

115. Howes, O., McCutcheon, R., and Stone, J. (2015). Glutamate and dopamine in schizophrenia: an update for the 21st century. J. Psychopharmacol. *29*, 97–115.

116. McCutcheon, R.A., Abi-Dargham, A., and Howes, O.D. (2019). Schizophrenia, Dopamine and the Striatum: From Biology to Symptoms. Trends Neurosci. *42*, 205–220.

117. Matsushima, A., Pineda, S.S., Crittenden, J.R., Lee, H., Galani, K., Mantero, J., Tombaugh, G., Kellis, M., Heiman, M., and Graybiel, A.M. (2023). Transcriptional vulnerabilities of striatal neurons in human and rodent models of Huntington's disease. Nat. Commun. *14*, 282.

118. Tippett, L.J., Waldvogel, H.J., Thomas, S.J., Hogg, V.M., van Roon-Mom, W., Synek, B.J., Graybiel, A.M., and Faull, R.L.M. (2007). Striosomes and mood dysfunction in Huntington's disease. Brain *130*, 206–221.

119. Hedreen, J.C., Berretta, S., and White, C.L., Iii (2024). Postmortem neuropathology in early Huntington disease. J. Neuropathol. Exp. Neurol. *83*, 294–306.

120. Hikosaka, O., and Wurtz, R.H. (1985). Modification of saccadic eye movements by GABA-related substances. II. Effects of muscimol in monkey substantia nigra pars reticulata. J. Neurophysiol. *53*, 292–308.

121. Keller, E.L. (1974). Participation of medial pontine reticular formation in eye movement generation in monkey. J. Neurophysiol. *37*, 316–332.

122. Mink, J.W., and Thach, W.T. (1993). Basal ganglia intrinsic circuits and their role in behavior. Curr. Opin. Neurobiol. *3*, 950–957.

123. Poewe, W. (2008). Non-motor symptoms in Parkinson's disease. Eur. J. Neurol. *15 Suppl 1*, 14–20.

124. Sharma, S., Moon, C.S., Khogali, A., Haidous, A., Chabenne, A., Ojo, C., Jelebinkov, M., Kurdi, Y., and Ebadi, M. (2013). Biomarkers in Parkinson's disease (recent update). Neurochem. Int. *63*, 201–229.

125. Julien, C.L., Thompson, J.C., Wild, S., Yardumian, P., Snowden, J.S., Turner, G., and Craufurd, D. (2007). Psychiatric disorders in preclinical Huntington's disease. J. Neurol. Neurosurg. Psychiatry *78*, 939–943.

126. Jog, M.S., Kubota, Y., Connolly, C.I., Hillegaart, V., and Graybiel, A.M. (1999). Building neural representations of habits. Science *286*, 1745–1749.

127. Thorn, C.A., Atallah, H., Howe, M., and Graybiel, A.M. (2010). Differential dynamics of activity changes in dorsolateral and dorsomedial striatal loops during learning. Neuron *66*, 781–795.

128. Desrochers, T.M., Jin, D.Z., Goodman, N.D., and Graybiel, A.M. (2010). Optimal habits can develop spontaneously through sensitivity to local cost. Proc. Natl. Acad. Sci. U. S. A. *107*, 20512–20517.

129. Barnes, T.D., Mao, J.-B., Hu, D., Kubota, Y., Dreyer, A.A., Stamoulis, C., Brown, E.N., and Graybiel, A.M. (2011). Advance cueing produces enhanced action-boundary patterns of spike activity in the sensorimotor striatum. J. Neurophysiol. *105*, 1861–1878.

130. Smith, K.S., Virkud, A., Deisseroth, K., and Graybiel, A.M. (2012). Reversible online control of habitual behavior by optogenetic perturbation of medial prefrontal cortex. Proc. Natl. Acad. Sci. U. S. A. *109*, 18932–18937.

131. Smith, K.S., and Graybiel, A.M. (2013). A dual operator view of habitual behavior reflecting cortical and striatal dynamics. Neuron *79*, 361–374.

132. Smith, K.S., and Graybiel, A.M. (2016). Habit formation coincides with shifts in reinforcement representations in the sensorimotor striatum. J. Neurophysiol. *115*, 1487–1498.

133. Fujii, N., and Graybiel, A.M. (2003). Representation of action sequence boundaries by macaque prefrontal cortical neurons. Science *301*, 1246–1249.

134. Barnes, T.D., Kubota, Y., Hu, D., Jin, D.Z., and Graybiel, A.M. (2005). Activity of striatal neurons reflects dynamic encoding and recoding of procedural memories. Nature *437*, 1158–1161.

135. Martiros, N., Burgess, A.A., and Graybiel, A.M. (2018). Inversely Active Striatal Projection Neurons and Interneurons Selectively Delimit Useful Behavioral Sequences. Curr. Biol. *28*, 560–573.e5.

136. Jin, X., and Costa, R.M. (2010). Start/stop signals emerge in nigrostriatal circuits during sequence learning. Nature *466*, 457–462.

137. Geddes, C.E., Li, H., and Jin, X. (2018). Optogenetic Editing Reveals the Hierarchical Organization of Learned Action Sequences. Cell *174*, 32–43.e15.

138. Desrochers, T.M., Amemori, K.-I., and Graybiel, A.M. (2015). Habit Learning by Naive Macaques Is Marked by Response Sharpening of Striatal Neurons Representing the Cost and Outcome of Acquired Action Sequences. Neuron *87*, 853–868.

139. Graybuck, L.T., Daigle, T.L., Sedeño-Cortés, A.E., Walker, M., Kalmbach, B., Lenz, G.H., Morin, E., Nguyen, T.N., Garren, E., Bendrick, J.L., et al. (2021). Enhancer viruses for

combinatorial cell-subclass-specific labeling. Neuron *109*, 1449–1464.e13.

140. Mich, J.K., Graybuck, L.T., Hess, E.E., Mahoney, J.T., Kojima, Y., Ding, Y., Somasundaram, S., Miller, J.A., Kalmbach, B.E., Radaelli, C., et al. (2021). Functional enhancer elements drive subclass-selective expression from mouse to primate neocortex. Cell Rep. *34*, 108754.

141. Lee, H., Fenster, R.J., Pineda, S.S., Gibbs, W.S., Mohammadi, S., Davila-Velderrain, J., Garcia, F.J., Therrien, M., Novis, H.S., Gao, F., et al. (2020). Cell Type-Specific Transcriptomics Reveals that Mutant Huntingtin Leads to Mitochondrial RNA Release and Neuronal Innate Immune Activation. Neuron *107*, 891–908.e8.

142. Berretta, S., Robertson, H.A., and Graybiel, A.M. (1992). Dopamine and glutamate agonists stimulate neuron-specific expression of Fos-like protein in the striatum. J. Neurophysiol. *68*, 767–777.

143. Parthasarathy, H.B., and Graybiel, A.M. (1997). Cortically driven immediate-early gene expression reflects modular influence of sensorimotor cortex on identified striatal neurons in the squirrel monkey. J. Neurosci. *17*, 2477–2491.

144. Manning, E.E., Dombrovski, A.Y., Torregrossa, M.M., and Ahmari, S.E. (2019). Impaired instrumental reversal learning is associated with increased medial prefrontal cortex activity in Sapap3 knockout mouse model of compulsive behavior. Neuropsychopharmacology *44*, 1494–1504.

145. Märtin, A., Calvigioni, D., Tzortzi, O., Fuzik, J., Wärnberg, E., and Meletis, K. (2019). A Spatiomolecular Map of the Striatum. Cell Rep. *29*, 4320–4333.e5.

146. Liu, K., Kim, J., Kim, D.W., Zhang, Y.S., Bao, H., Denaxa, M., Lim, S.-A., Kim, E., Liu, C., Wickersham, I.R., et al. (2017). Lhx6-positive GABA-releasing neurons of the zona incerta promote sleep. Nature *548*, 582–587.

147. Kohara, K., Pignatelli, M., Rivest, A.J., Jung, H.-Y., Kitamura, T., Suh, J., Frank, D., Kajikawa, K., Mise, N., Obata, Y., et al. (2014). Cell type-specific genetic and optogenetic tools reveal hippocampal CA2 circuits. Nat. Neurosci. *17*, 269–279.

148. Wickersham, I.R., Sullivan, H.A., and Seung, H.S. (2010). Production of glycoprotein-deleted rabies viruses for monosynaptic tracing and high-level gene expression in neurons. Nat. Protoc. *5*, 595–606.

149. Wickersham, I.R., and Sullivan, H.A. (2015). Rabies viral vectors for monosynaptic tracing and targeted transgene expression in neurons. Cold Spring Harb. Protoc. *2015*, 375–385.

150. Chatterjee, S., Sullivan, H.A., MacLennan, B.J., Xu, R., Hou, Y., Lavin, T.K., Lea, N.E., Michalski, J.E., Babcock, K.R., Dietrich, S., et al. (2018). Nontoxic, double-deletion-mutant rabies viral vectors for retrograde targeting of projection neurons. Nat. Neurosci. *21*, 638–646.

151. Tai, L.-H., Lee, A.M., Benavidez, N., Bonci, A., and Wilbrecht, L. (2012). Transient stimulation of distinct subpopulations of striatal neurons mimics changes in action value. Nat. Neurosci. *15*, 1281–1289.

152. Weglage M, Wärnberg E, Lazaridis I, Calvigioni D, Tzortzi O, Meletis K. Complete representation of action space and value in all dorsal striatal pathways. Cell Rep. 2021 Jul 27;36(4):109437.

153. He M, Tucciarone J, Lee S, Nigro MJ, Kim Y, Levine JM, Kelly SM, Krugikov I, Wu P, Chen Y, Gong L, Hou Y, Osten P, Rudy B, Huang ZJ. Strategies and Tools for Combinatorial Targeting of GABAergic Neurons in Mouse Cerebral Cortex. Neuron. 2016 Sep 21;91(6):1228-1243.

154. Yoshida J, Oñate M, Khatami L, Vera J, Nadim F, Khodakhah K. Cerebellar Contributions to the Basal Ganglia Influence Motor Coordination, Reward Processing, and Movement Vigor. J Neurosci. 2022 Nov 9;42(45):8406-8415.

155. Fullard JF, Hauberg ME, Bendl J, Egervari G, Cirnaru MD, Reach SM, Motl J, Ehrlich ME, Hurd YL, Roussos P. An atlas of chromatin accessibility in the adult human brain. Genome Res. 2018 Aug;28(8):1243-1252.

156. Hsu AI, Yttri EA. B-SOiD, an open-source unsupervised algorithm for identification and fast prediction of behaviors. Nat Commun. 2021 Aug 31;12(1):5188.

157. Mathis A, Mamidanna P, Cury KM, Abe T, Murthy VN, Mathis MW, Bethge M. DeepLabCut: markerless pose estimation of user-defined body parts with deep learning. Nat Neurosci. 2018 Sep;21(9):1281-1289.

158. Hueske E, Stine C, Yoshida T, Crittenden JR, Gupta A, Johnson JC, Achanta AS, Loftus J, Mahar A, Hul D, Azocar J, Gray RJ, Bruchas MR, Graybiel AM. Developmental and adult striatal patterning of nociceptin ligand marks striosomal population with direct dopamine projections. bioRxiv [Preprint]. 2024 May 15:2024.05.15.594426.

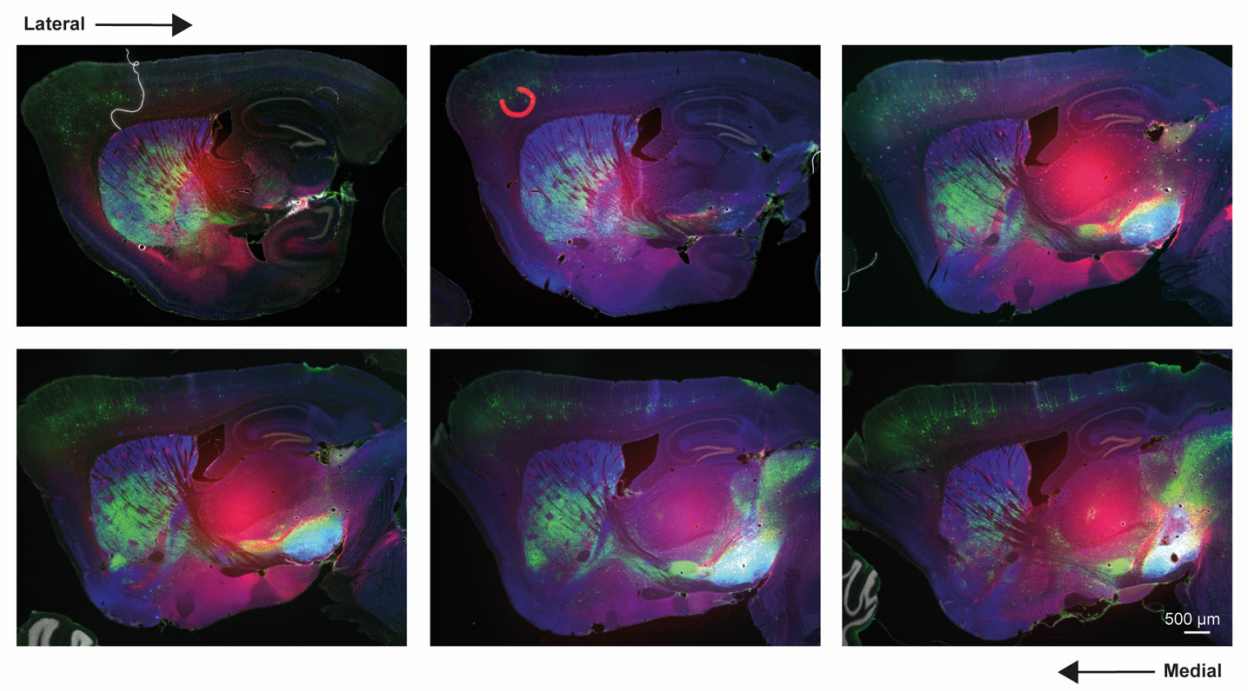

Supplementary Figure 1. Images of series of sagittal sections from a PV-Cre mouse with retrograde monosynaptic labeling of PV cells in SNpr
RV-mCherry-labeled neurons (green) counterstained for anti-MOR1 (striosome marker, red), anti-CDGI (matrix marker, blue) and DAPI (gray).

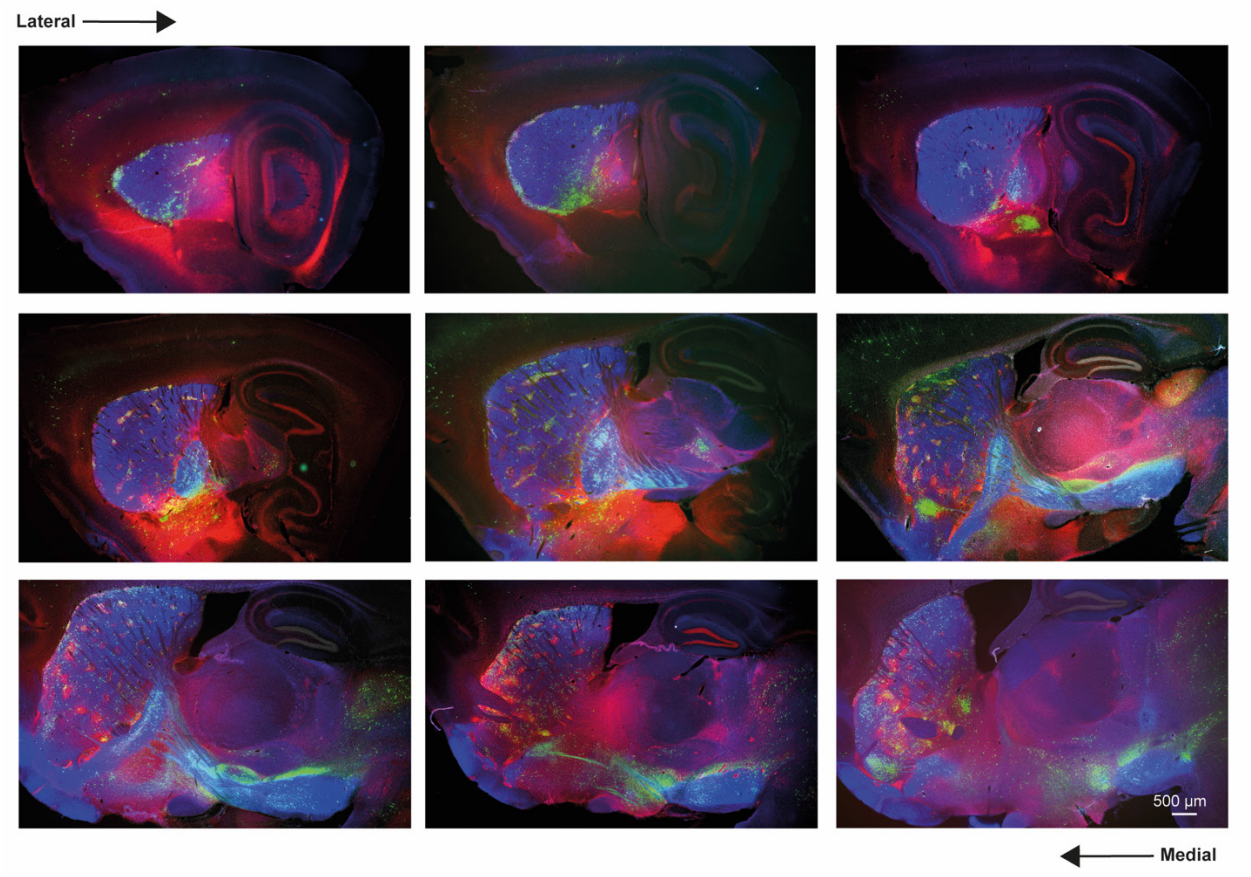

Supplementary Figure 2. Images of series of sagittal sections from a DAT-Cre mouse with retrograde monosynaptic labeling of dopamine cells in SNpc
RV-EYFP-labeled neurons (green) counterstained for anti-MOR1 (striosome marker, red), anti-CDGI (matrix marker, blue) and DAPI (gray).

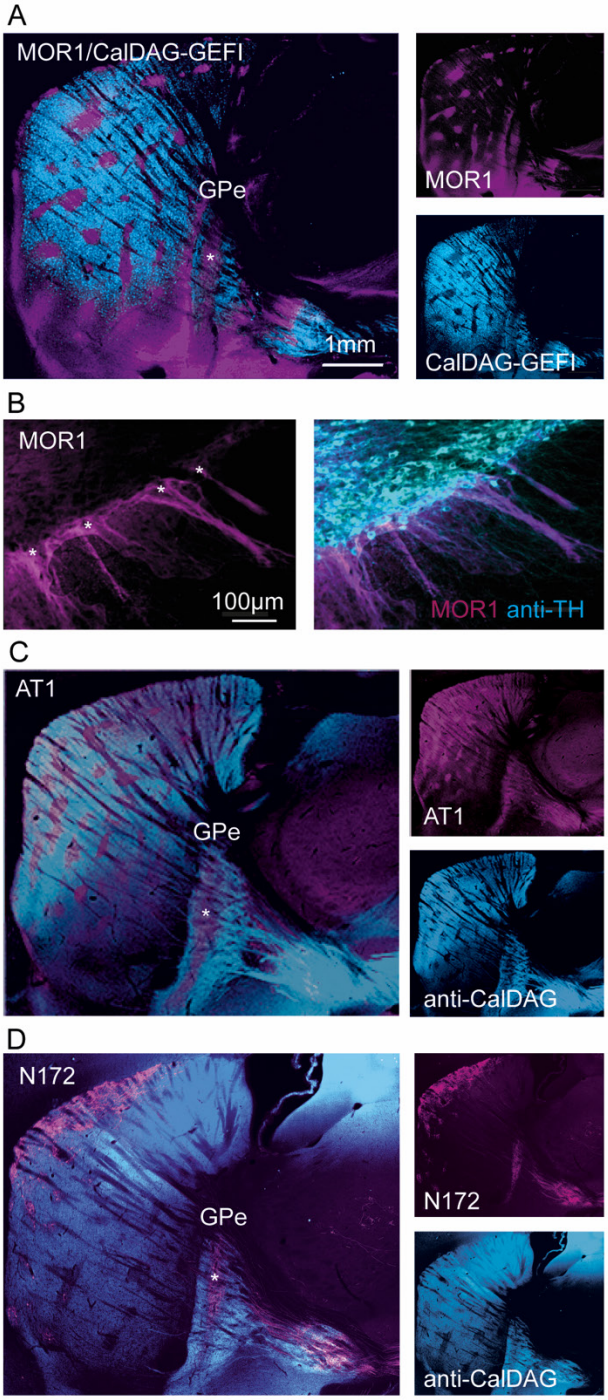

Supplementary Figure 3. Striosomal and matrix neurons target different regions of the globus pallidus

A. Representative sagittal brain section from double-transgenic mice carrying MOR1-mCherry knock-in transgene (magenta) and the CalDAG-GEFI-GFP BAC (cyan).

B. Coronal hemisections through the anterior SNpc of MOR1-mCherry line in immunolabeled for the striosome reporter (magenta, left) and the dopamine transporter (cyan, right) to identify dopaminergic cell bodies and descending dendrites. Asterisks designate the tops of striosome-dendron bouquets.
C. Representative sagittal section from AT1-tdTomato (magenta) transgenic mouse brain immunolabeled for CalDAG-GEFI (cyan).
D. Representative sagittal section from P172-mCitrine (magenta) transgenic mouse brain immunolabeled for CalDAG-GEFI (cyan).

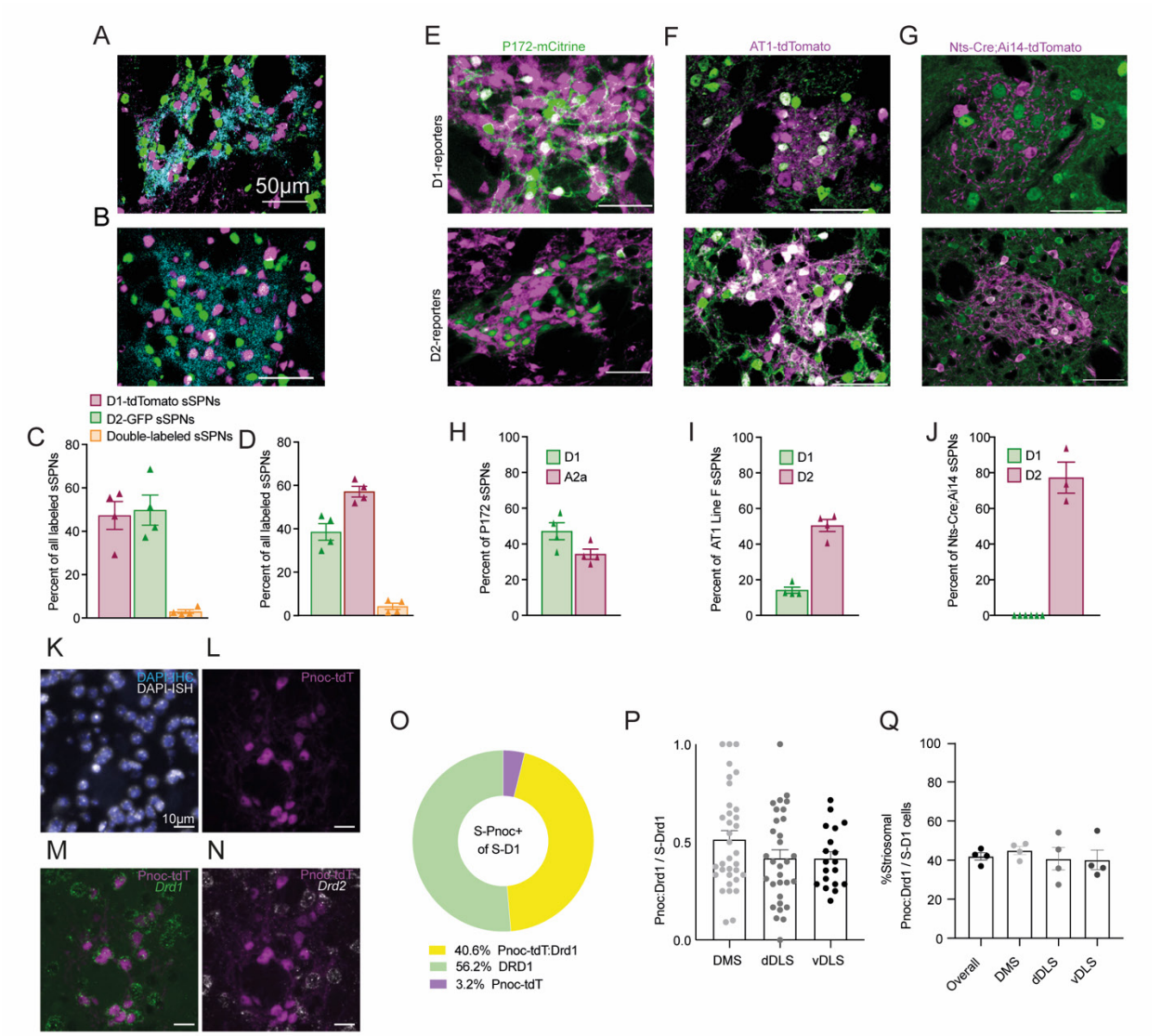

Supplementary Figure 4. Characterization of striosomal lines

A-D. Striosomes contain similar proportions of neurons expressing the D1 or D2 dopamine receptor subtype. Striatal sections from D1-tdTomato;D2-GFP double-transgenic (A) and D1-GFP;A2a-Cre;Ai14-tdTomato triple-transgenic mice (B) were immunolabeled for tdTomato, GFP, and the striosome marker MOR1 (cyan). Within striosomes, counts for cells with the D1 and D2 markers were similar. The fluorescence for D1-tdTomato was stronger than for D1-GFP, and higher numbers of D1-type neurons were observed in (c) than in (d), consistent with previous reports {Shuen, 2008, 18337395}. Error bars show SEM. Two male and 2 female mice for each genotype. Three coronal sections (anterior, mid-level and caudal regions) were evaluated for each mouse. Neurons were counted in all of the MOR1-identified striosomes that were dorsal to the anterior commissure.

E-G. Striosome lines show differential reporter expression in D1 (top) and D2 (bottom) striosomal SPNs. Representative images of striosomes used to measure reporter expression in D1 and D2 striosomal SPNs are shown for mice labeled for P172-mCitrine striosomal SPNs (green, E), AT1-tdTomato soma-targeting line F (magenta, F) and Nts-Cre and Ai14-tdTomato sSPNs (magenta, G). Double-labeled cells appear white.

H-J. Plots showing the percent of SPNs positive for striosome marker that are double-labeled for D1 or D2/A2a reporters in mice for striosome marker P172-mCitrine (H), AT1-tdTomato (I) or Nts-Cre (J). For H and I, n = 4 mice for each double-transgenic genotype, balanced for sex. For J, n = 2 mice for Nts-Cre;Ai14;D1-GFP and n = 1 mouse for Nts-Cre;Ai14;D2-GFP. For each mouse, three coronal sections, taken from the anterior, mid-level and caudal regions, were evaluated. Counts were made only for cells within striosomes identified by MOR1 (for clarity, not shown).
K. Sequential immunostaining (IHC) and *in situ* hybridization (ISH) protocols were performed on the same brain sections and resulting images aligned according to DAPI-IHC (blue) and DAPI-ISH (white) signals**.**
L. Striosomal Pnoc;Ai14-tdTomato neurons detected by clusters of striatal tdTomato expressing cells.
M and N. *Drd1* (M, green) and *Drd2* (N, white) signals were labeled by ISH.
O. Striosomal Pnoc;Ai14 tdTomato reporter-expressing neurons labeled by ISH for *Drd1* accounted for 40% of all striosomal *Drd1* neurons.
P. Variation in the proportion of striosomal *Drd1*-labeled neurons expressing Pnoc reporter, tdTomato, is shown across individual striosomes (dots) in the DMS, dorsal DLS (dDLS) and ventral DLS (vDLS).
Q. Data averaged across mice (4 sections from 4 mice; 22, 19, 21, 23 striosomes per section; 500.5 ± 64 striosomal cells per section), shown as mean ± SEM.

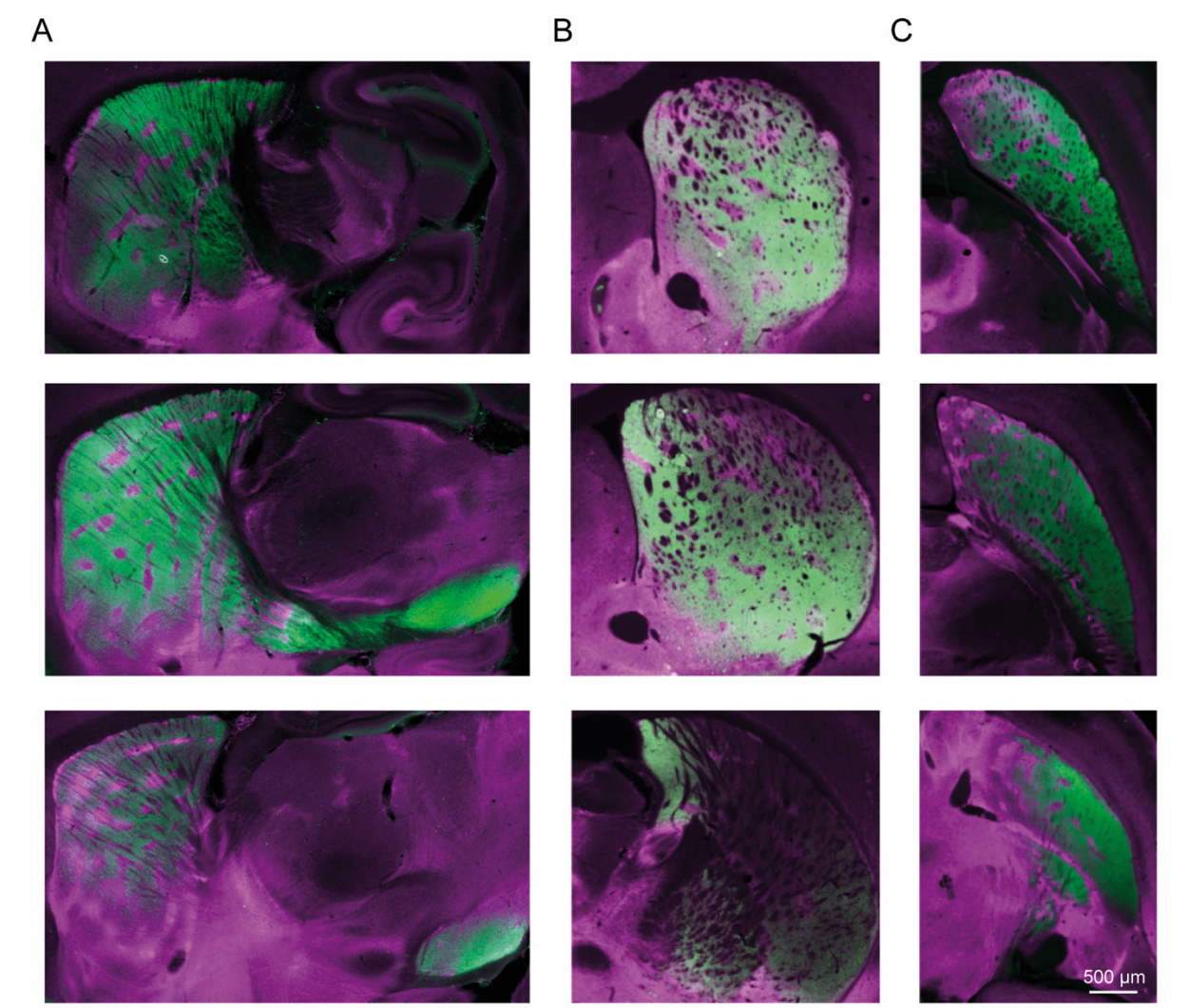

Supplementary Figure 5. Projection pattern of MOR1-mCherry/ CalDAG-GEFI-GFP
Images of sagittal (A), coronal (B) and para-horizontal (C) sections at three levels (from top to bottom, lateral to medial in A, anterior to posterior in B and dorsal to ventral in C) through the striatum of double-transgenic mice carrying MOR1-mCherry knock-in transgene (magenta) and the CalDAG-GEFI-GFP BAC, immunolabeled for mCherry (magenta) and GFP (green).

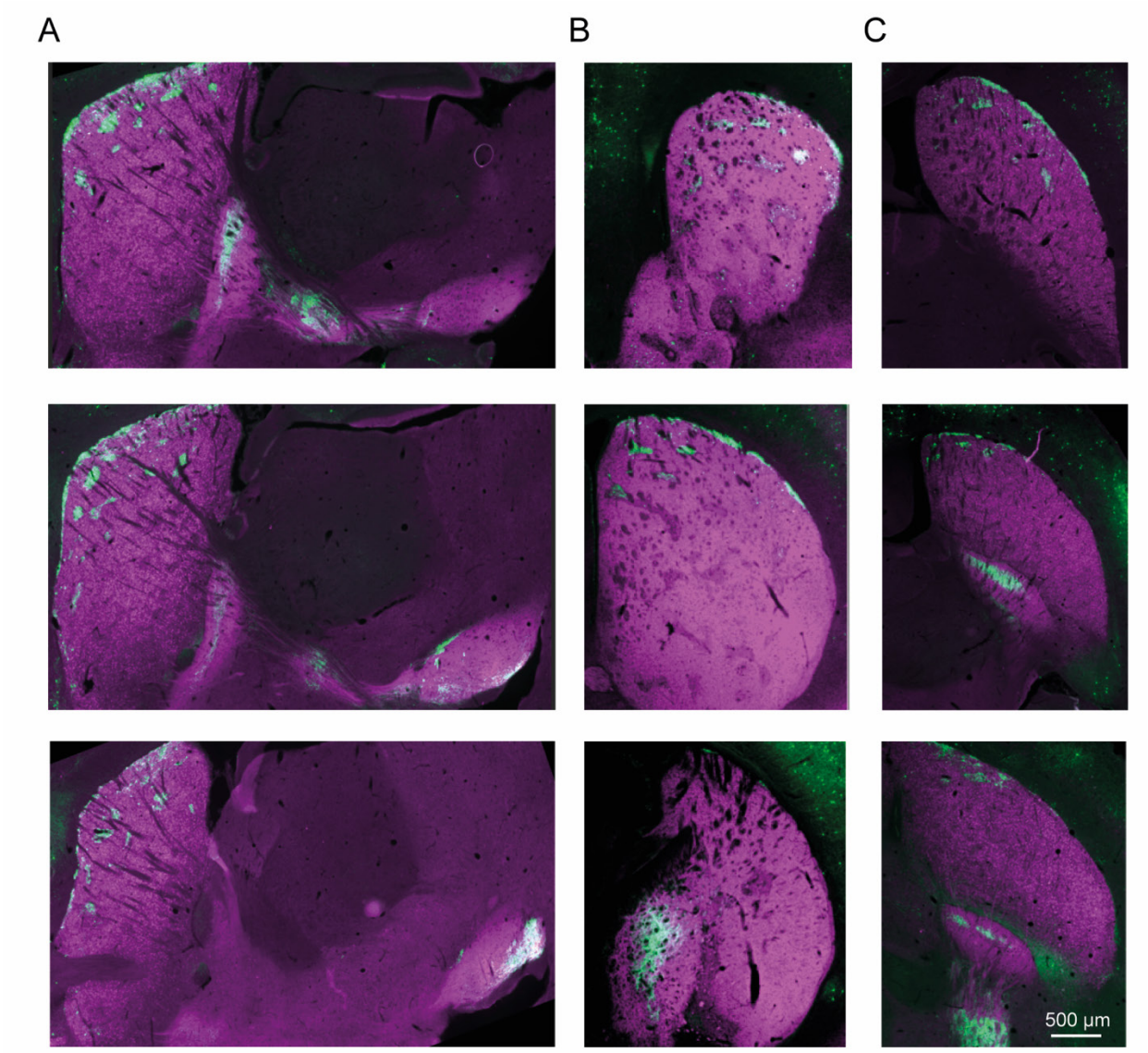

Supplementary Figure 6. Projection pattern of P172-mCitrine
Images of sagittal (A), coronal (B) and para-horizontal (C) sections at three striatal levels described in Supplementary Figure 5 from P172-mCitrine mice, immunolabeled for mCitrine (green) and CalDAG-GEFI (cyan).

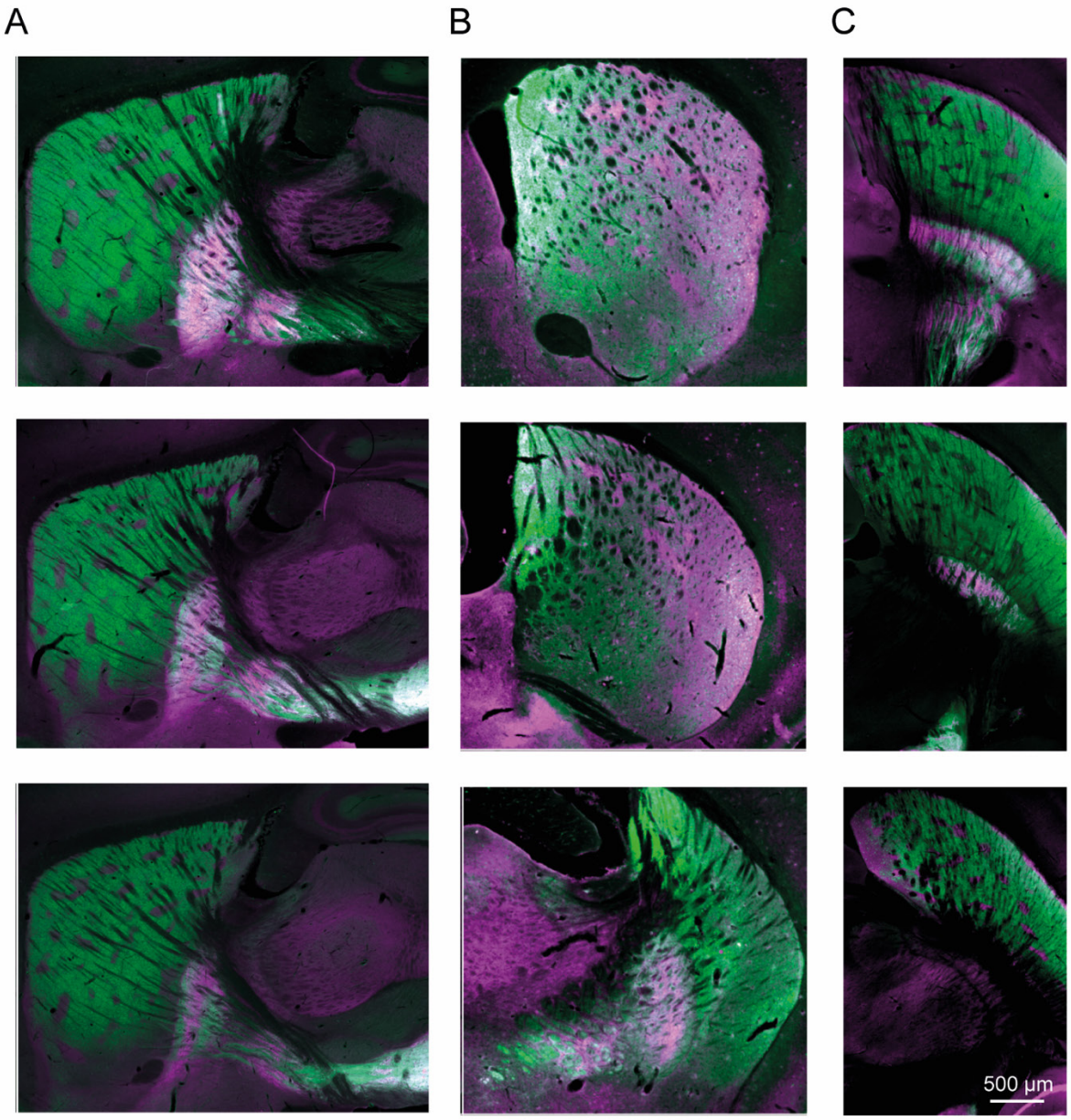

Supplementary Figure 7. Projection pattern of AT1-tdTomato
Images of striatal sections described in Supplementary Figure 5 from double-transgenic mice carrying BACs for AT1-tdTomato axon-targeting line 14 and CalDAG-GEFI-GFP, immunolabeled for tdTomato (magenta) and GFP (green).

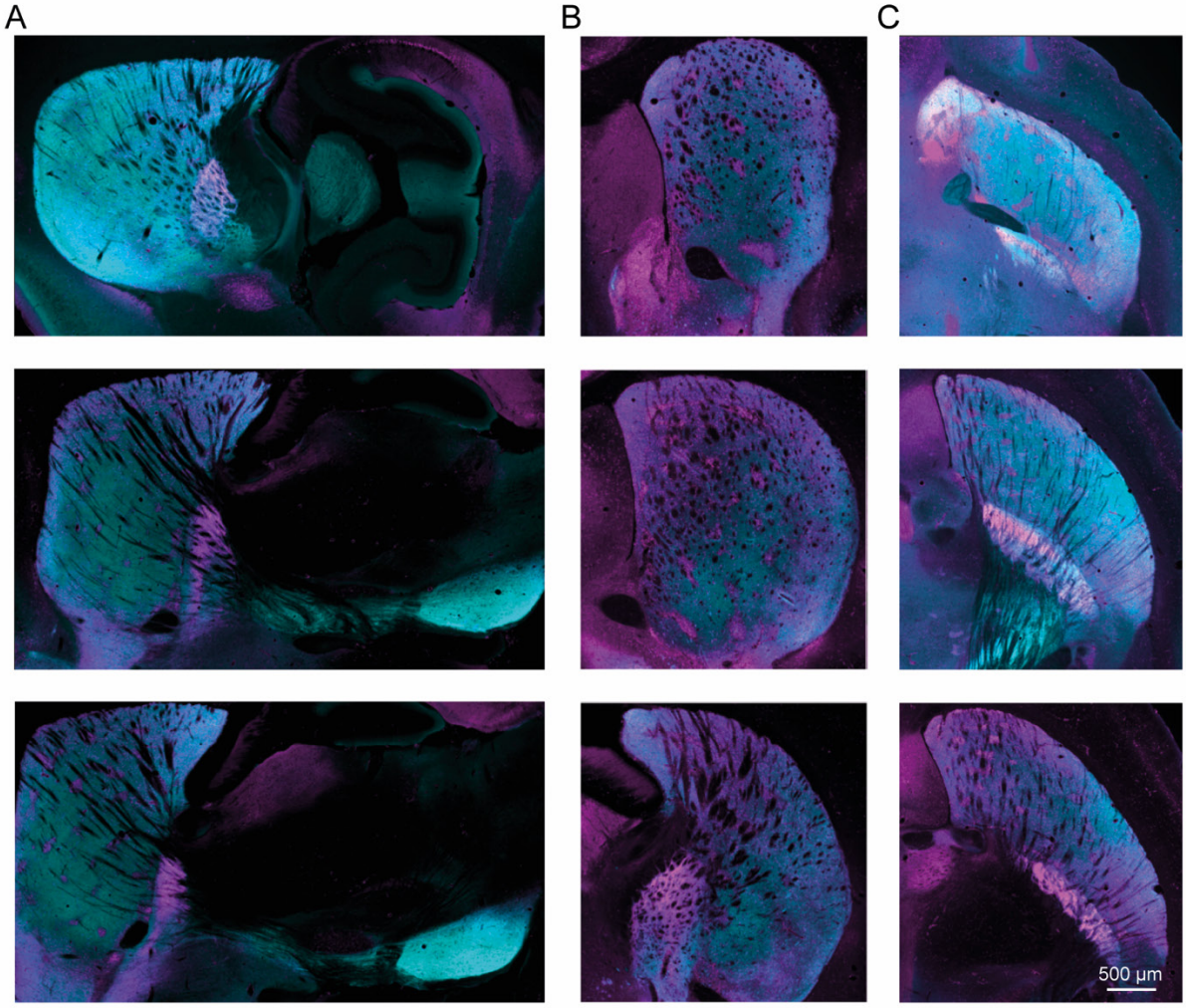

Supplementary Figure 8. Projection pattern of Nts-Cre/Ai14-tdTomato
Images of striatal sections described in Supplementary Figure 5 from double-transgenic mice carrying the Nts-Cre knock-in transgene and Cre-dependent Ai14-tdTomato (magenta), immunolabeled for mCherry (magenta) and CalDAG-GEFI (cyan).

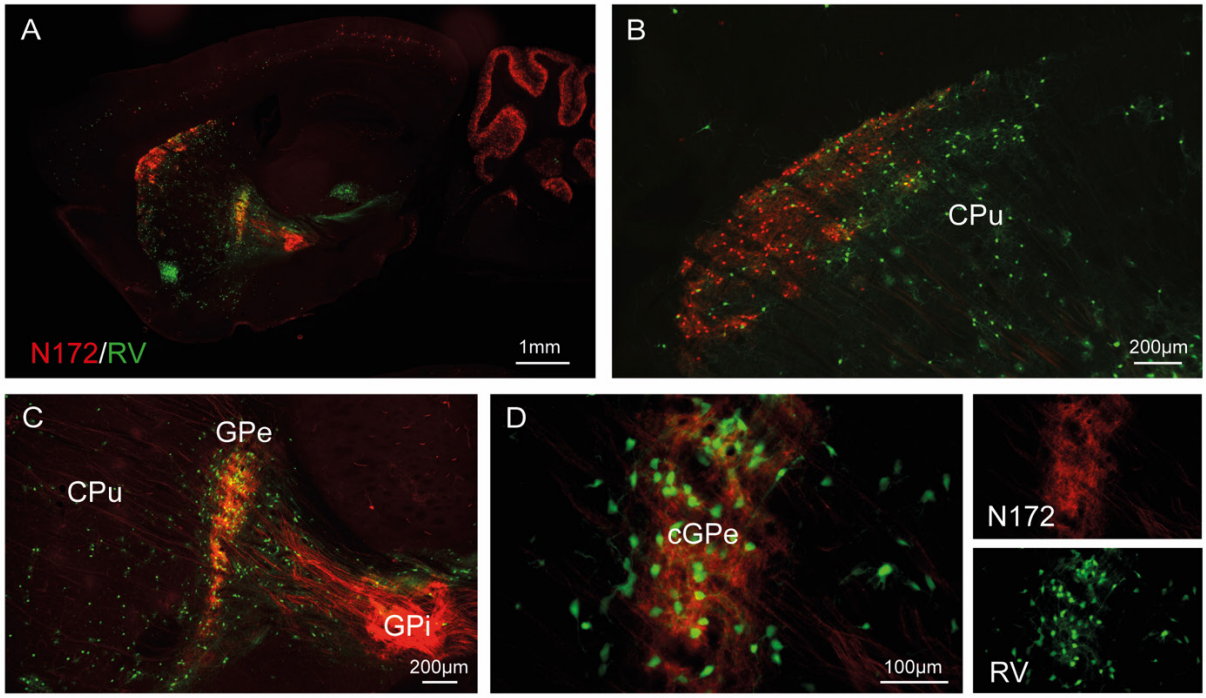

Supplementary Figure 9. RV tracing in N172-tdTomato/DAT-Cre mice

A-D. Rabies-expressing SNpc-dopamine-targeting GPe neurons coinciding with striosomal D2/N172-labeled terminals in the cGPe zone. Sagittal sections from two N172-tdTomato/DAT-Cre transgenic mice that received injections of rabies-EGFP and Cre-dependent helper AAVs into the SNpc. Retrogradely infected neurons as defined by co-labeling for the striosomal SPN markers P172-mCitrine (red) (B enlargement of CPu). Retrogradely infected neurons are also strikingly enriched in the cGPe defined by striosomal SPN neuropil in red (C and D enlargement of GPe).

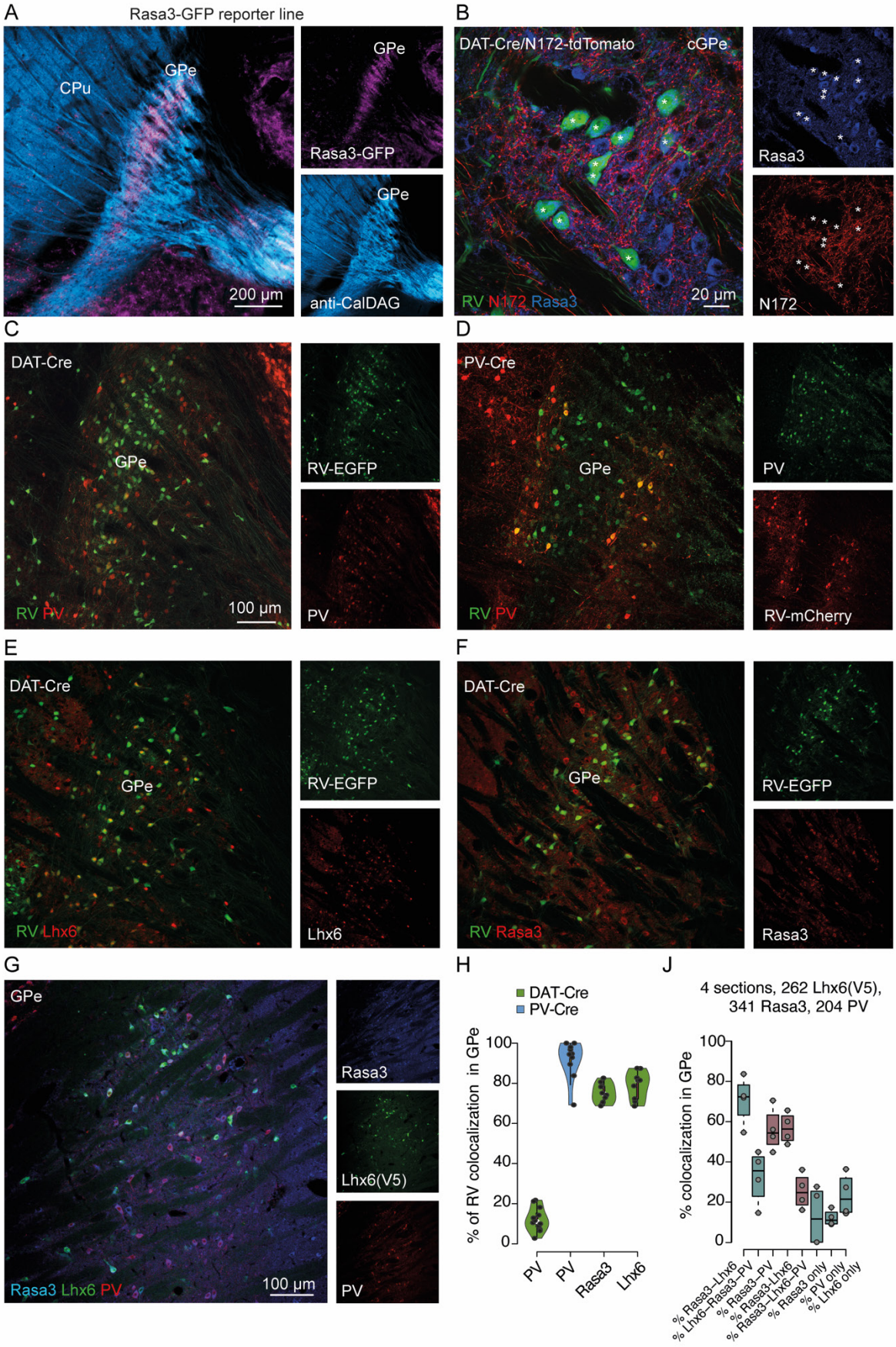
A
Rasa3-GFP reporter line
CPu
GPe
200 µm
GPe
Rasa3-GFP
GPe
anti-CalDAG
B
DAT-Cre/N172-tdTomato
cGPe
RV N172 Rasa3
20 µm
Rasa3
N172
C
DAT-Cre
GPe
RV PV
100 µm
RV-EGFP
PV
D
PV-Cre
GPe
RV PV
PV
RV-mCherry
E
DAT-Cre
GPe
RV Lhx6
RV-EGFP
Lhx6
F
DAT-Cre
GPe
RV Rasa3
RV-EGFP
Rasa3
G
GPe
Rasa3 Lhx6 PV
100 µm
Rasa3
Lhx6(V5)
PV
H
DAT-Cre
PV-Cre
% of RV colocalization in GPe
100
80
60
40
20
0
PV
PV
Rasa3
Lhx6
J
4 sections, 262 Lhx6(V5),
341 Rasa3, 204 PV
% colocalization in GPe
100
80
60
40
20
0
% Rasa3–Lhx6
% Lhx6–Rasa3–PV
% Rasa3–PV
% Rasa3–Lhx6
% Rasa3–Lhx6–PV
% Rasa3 only
% PV only
% Lhx6 only

Supplementary Figure 10. Rasa3-GFP and central zone dopamine-projecting neuron characterization

A. Sagittal section from a Rasa3-GFP BAC transgenic mouse brain shows preferential distribution of GFP-positive cells (magenta) in the cGPe, relative to the pGPe that is targeted by matrix SPN axons immunolabeled for CalDAG-GEFI (cyan).

B. Dopamine-projecting cGPe neurons, targeted by N172 striosomal terminals, are Rasa3/Lhx6 positive.

C-F. Representative images of RV-labeled neurons and colocalization with PV (C), Lhx6 (E) and Rasa3 (F) in DAT-Cre tracing and colocalization with PV in PV-Cre tracing (D).

G. Representative image of Lhx6-Cre mice injected with AAV-DIO-EYFP and immunolabeled for PC and Rasa3 (quantification in J)

H, Quantification of PV, Rasa3- and Lhx6-positive RV-labeled neurons in the GPe. PV in DAT-Cre mice: 613 RV-labeled neurons in 12 sections from 3 mice. PV in PV-Cre mice: 291 RV-labeled neurons in 10 sections from 3 mice. Rasa3 in DAT-Cre mice: 1053 RV-labeled neurons in 10 sections from 3 mice. Lhx6 in DAT-Cre mice: 1029 RV-labeled neurons in 9 sections from 3 mice.

J. Quantification of PV, Rasa3 and Lhx6 colocalization in the GPe (see representative image in G).

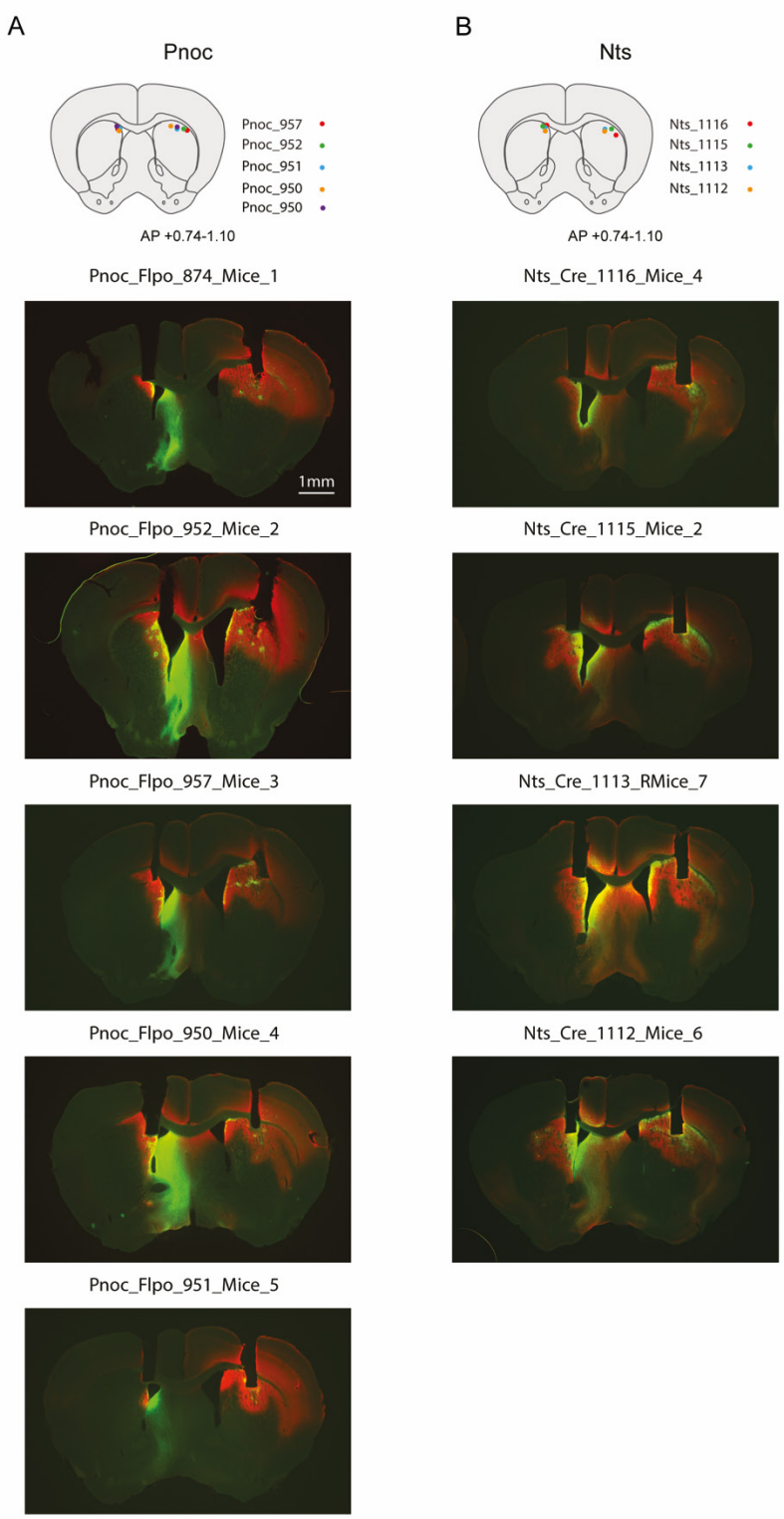

Supplementary Figure 11. Injection sites and fiber placement for the 2-choice probabilistic switching maze task

Injection sites and fiber placement of Pnoc and Nts mice included in the analysis for the 2-choice probabilistic switching maze task presented in Figure 6.

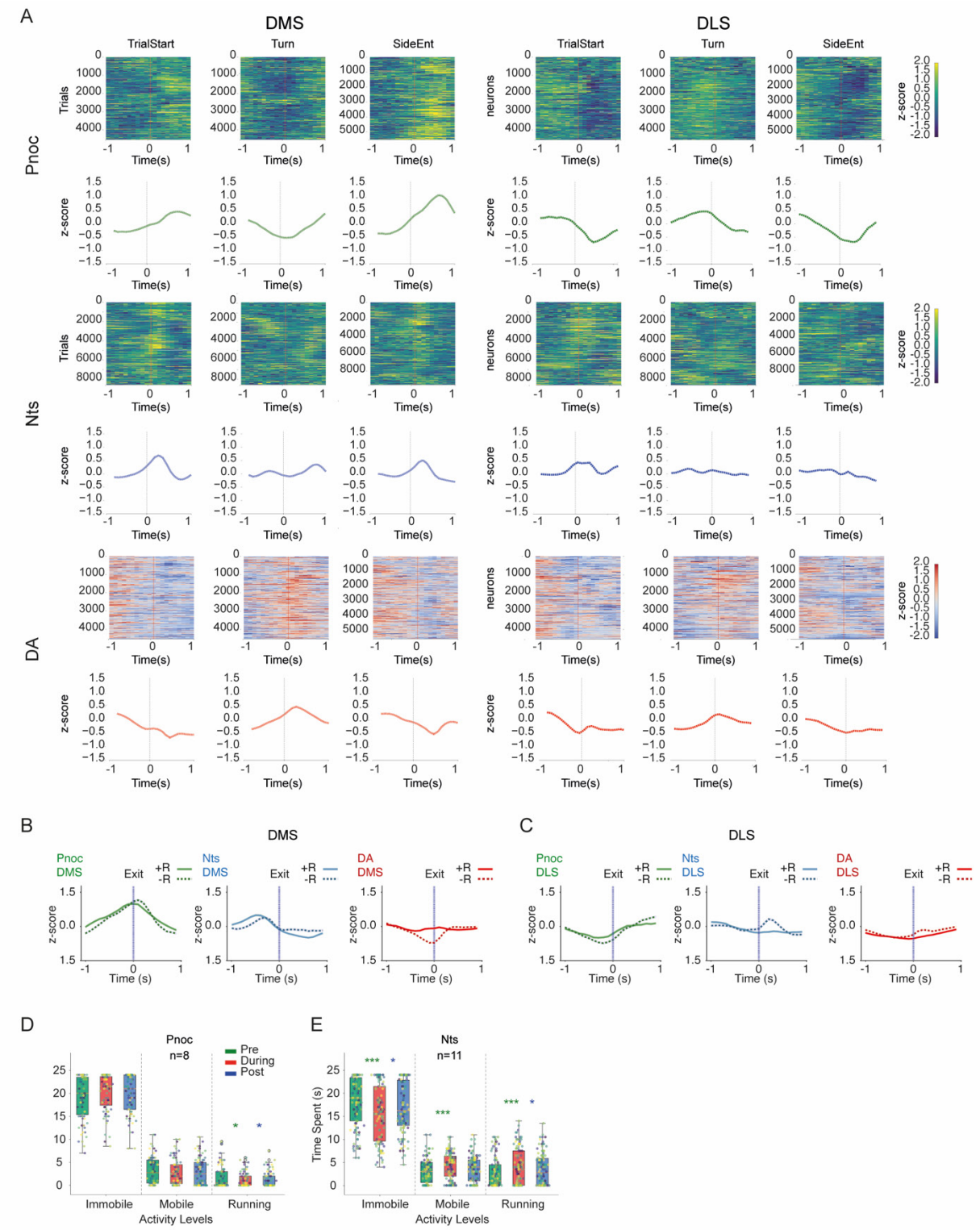

Supplementary Figure 12. Temporal dynamics of Pnoc, Nts and dopamine activity related to figure 6 and 7; Mobility score from optogenetic experiments related to Figure 5

A. Temporal dynamics of Pnoc, Nts and dopamine activity (average from all mice all sessions) during trial recorded in the DMS (left) and DLS (right). Columns correspond to different behavioral events, and rows represent different activity measures (Pnoc, Nts and dopamine).

B. Temporal dynamics of Pnoc, Nts and dopamine activity in DMS, aligned to the initiation, left and right ports exit for rewarded and unrewarded trials. Dopamine activity differentiates rewarded (+R) from unrewarded (−R) trials before the exit aligned to the reward delivery time (see Figure 6K).
C. Same as B, but for activity in DLS. Nts activity deference between rewarded and unrewarded trials aligns well to the port exit but not to the outcome delivery time.
D and E. Time spent in immobile (<2 cm/sec), mobile (2-6 cm/sec) and running (>6 cm/sec) activity levels before, during and after the ontogenetic stimulation of S-D1 (D) and S-D2 (E) SPNs.

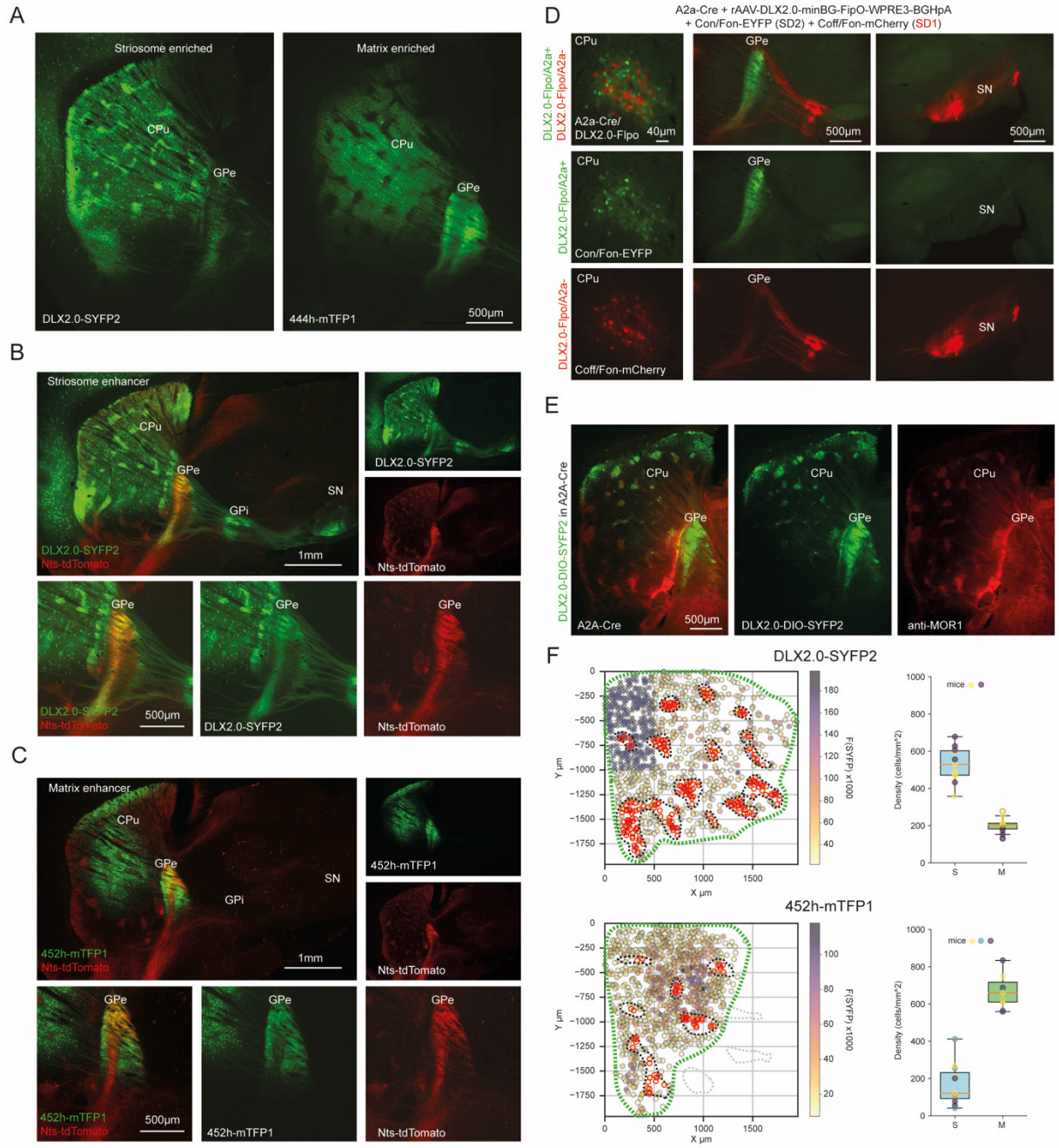

Supplementary Figure 13. Striosome and matrix targeting with enhancer viruses

A. Sagittal section demonstrating the expression pattern of DLX2.0-SYFP2 (rAAV-DLX2.0-minBglobin-SYFP2-WPRE3-BGHpA, A) and rAAV-eHGT_444h-minBglobin-mTFP1-WPRE3-BGHpA (444h-mTFP1, B). Both viruses were injected with the same volume (500 nl) and at the same coordinates (AP +0.86 mm, ML 1.6 mm, and DV 2.8 mm). Mice were perfused three weeks after injection.

B. Comparison of striosome enhancer virus expression in Nts;tdTomato mice. Top panels show representative sagittal section depicting the expression patterns following the intrastriatal injection of the striosomal enhancer DLX2.0-SYFP2, as described in A. The left panel illustrates the overlay of DLX2.0-SYFP2 (green) and Nts;tdTomato (red) expression patterns, and right panels show separated channels for DLX2.0-SYFP2 (green) and Nts;tdTomato (red). Bottom Panels show,

from left to right, enlarged views of the GPe with the combined fluorescence of both DLX2.0-SYFP2 (green) and Nts;tdTomato (red), followed by individual channels with DLX2.0-SYFP2 expression and Nts;tdTomato, respectively.

C. Matrix enhancer virus expression in Nts;tdTomato mice. Top panels show sagittal sections from Nts;tdTomato mice, with the same injection parameters as those in A and B. These panels highlight the expression pattern of the matrix-specific enhancer virus rAAV-eHGT_452h-minBglobin-mTFP1-WPRE3-BGHpA (452h-mTFP1, green) in relation to the striosomal Nts;tdTomato SPNs. Bottom panels show sequence of images, from left to right, depicting the overlay of the matrix enhancer 452h-mTFP1 (green) and Nts;tdTomato (red), followed by the separated green and red channels.

D. Targeted expression in D1 or D2 striosomal SPNs. Top left panel shows a representative image of specific targeting within A2a-Cre mice, achieved through an intrastriatal injection of AAV-DLX2.0-minBG-FIPO-WPRE3-BGHpA, followed by injection of intersectional viruses (Con/Fon-EYFP for striosomal D2 and Coff/Fon-mCherry for striosomal D1). This resulted in the selective labeling of striosomal D1-SPNs with mCherry (red) and striosomal D2-SPNs with EYFP (green) within the striatum. Top middle image depicts the axonal projections of both D1 and D2 striosomal neurons in the GPe, highlighting the dense terminal zones of S-D2 in the cGPe and the continuation of specifically the D1 striosomal neuron axons downstream to the GPe to the GPi, and substantia nigra (top right). Bottom panels show individual channels, which separately depict the red fluorescence of D1-SPNs and the green fluorescence of D2-SPNs.

E. Specific targeting of striosomal D2 SPNs in A2a-Cre mice following an injection of the Cre-dependent striosomal enhancer virus DLX2.0-DIO-SYFP2 (AAV-DLX2.0-minBG-cDIO-SYFP2-WPRE-HGHpA). The overlay (left) illustrates the enhancer expression (green) and anti-MOR1 immunostaining (red) to confirm specificity to striosomes, with individual channels of green fluorescence marking the expression of the Cre-dependent enhancer virus (middle) and red immunostaining for MOR1 (right).

F. Cell density analysis in striosomal (top) and matrix (bottom) regions. Left panels show 2D plot of the spatial coordinates of cells labeled with DLX2.0-SYFP2 (top) or 452h-SYFP (bottom) from a representative section. Cells are color-coded according to fluorescence intensity. Cells located within striosomal regions are highlighted in red, with boundaries delineated by black dotted lines based on MOR1 staining. Green dotted lines indicate the area used for calculating cell density. An excluded area in the dorsomedial part of the striatum is marked with 'X' due to consistently decreased striosomal specificity in DLX2.0 expression in these striosomal area. Right panels show box plots representing the density of DLX2.0-SYFP2- or 452h-SYF-labeled cells in striosomal and matrix regions.

ST1: Transgenic mouse lies

Supplementary Table 1 Transgenic mouse lines

Mouse line descriptions and references	Genotype	Genetic background
Ai14 knock-in {Madisen, 2010, 20023653} Cre-dependent tdTomato reporter inserted at ROSA26 locus	B6;129S6-Gt(ROSA)26Sortm14(CAG-tdTomato)Hze/J	Mixed C57B6J and 129S1
A2a-Cre BAC {Gong, 2007, 17855595} Cre expressed in D2-positive matrix SPNs and striosomal SPNs and vascular cells of the brain	Tg(Adora2a-cre)KG126Gsat/Mmucd	C57B6/J
AT1-tdTomato BAC (see Methods and Figs. S5-S7) tdTomato inserted downstream of the AT1 start codon and slightly enriched in D2 striosomal SPNs	Tg(AT1-tdT) Lines 14 and F	Mixed FVB/N and Swiss Webster
CalDAG-GEFI-GFP BAC {Gong, 2003, 14586460;Crittenden, 2016, 27647894} GFP enriched in D1- and D2- positive matrix SPNs (see Figs. S5-S7 and Figs. S8-S10).	Tg(Rasgrp1-EGFP)KX214Gsat/Mmcd	Mixed FVB/N and Swiss Webster
D1-GFP BAC {Gong, 2003, 14586460} GFP widely expressed in D1-positive SPNs	Tg(Drd1-EGFP)X60Gsat	C57B6/J
D1-tdTomato BAC {Shuen, 2008, 18337395} tdTomato widely expressed in D1-positive SPNs	B6.Cg-Tg(Drd1a-tdTomato)6Calak/J	C57B6/J
D2-GFP BAC {Gong, 2003, 14586460} GFP widely expressed in D2-positive SPNs	Tg(Drd2-EGFP)S118Gsat	Mixed FVB/N and Swiss Webster

DAT-Cre knock-in {Backman, 2006, 16865686} Cre expressed in dopaminergic neurons	Slc6a3$^{tm1.1(cre)Bkmn}$	C57B6/J
Lhx6-Cre BAC {Fogarty, 2007, 17928435} Cre activity is observed in a subset of GPe projection neurons	B6;CBA-Tg(Lhx6-icre)1Kess/J	C57B6/J
MOR1-mCherry knock-in {Erbs, 2015, 24623156} mCherry is fused to the Mu opioid receptor and highly enriched in D1-positive striosomal SPNs (see Figs. S8-S10).	Oprm1tm4Kff/J	Mixed C57B6 and 129
Nts-Cre knock-in {Leinninger, 2011, 21907138} IRES-Cre gene cassette inserted in the 3'UTR of the endogenous neurotensin gene drives reporter expression in D2-positive SPNs, with enrichment in striosomes (see Figs. S11-S13)	Nts$^{tm1(cre)Mgmj}$ JAX#017525	Mixed C57B6 and 129
Pnoc-Cre {Parker, 20, 31348890} *Pnoc*-IRES-Cre knock-in mice express a Cre recombinase gene inserted upstream of the stop codon of the prepronociceptin (*Pnoc*) gene	Pnoc$^{tm1.1(cre)Mrbr}$	C57BL/6J
P172-mCitrine transposon {Shima, 2016, 26999799;Crittenden, 2016, 27647894} Piggyback enhancer trap line with mCitrine fluorophore under the control of the tet-transactivator and highly enriched in D1- and D2-positive striosomal SPNs (see Figs. S2-S4)	Piggyback-Tta Line 172	C57B6/J

PV-Cre knock-in {Hippenmeyer, 2005, 15836427} Cre expressed in parvalbumin-positive neurons, including within the SNpr	Pvalb$^{tm1(cre)Arbr}$	C57B6J
Rasa3-GFP BAC {Gong, 2003, 14586460} GFP enriched in GPe projection neurons within the striosome-targeted central region	Tg(Rasa3-EGFP)LJ222Gsat	FVBN X CD1 (ICR)

ST2: Antibodies

Supplementary Table 2 Antibodies

Primary Antibody	Host	Company	Catalog no.	Concentration
CalDAG-GEFI	Rabbit	N/A see Crittenden et al., N. Med. 2004	N/A	1:5000
Calbindin	Rabbit	Synaptic Systems	214 002	1:250
Cannabinoid receptor 1	Goat	Frontier Institute	CB1-Go-Af450	1:100
Dopamine transporter	Rat	Millioire	MAB369	1:250
DsRed	Rabbit	Clontech	#632496	1:200
GFP	Chicken	Abcam	Ab13970	1:2,000
Lhx6	Mouse	Santa Cruz	Sc-271433	1:100

μ-opioid receptor 1 (MOR1)	Goat	Santa Cruz	sc-7488	1:500
Parvalbumin	Guinea pig	Synaptic Systems	195 004	1:5000
Rasa3	Rabbit	Abcam	ab153846	1:4000
Tyrosine hydroxylase	Sheep	Abcam	ab113	1:1000

Secondary Antibody	**Company**	**Catalog no.**	**Concentration**
Donkey anti-chicken IgG (H+L) Alexa Fluor 488	Thermo Fisher Scientific	A-11039	1:300
Donkey anti-rabbit IgG (H+L) Alexa Fluor 546	Thermo Fisher Scientific	A-10040	1:300
Donkey anti-goat IgG (H+L) Alexa Fluor 647	Thermo Fisher Scientific	A-21447	1:300
Goat anti-rabbit IgG (H+L) Alexa Fluor 405	Thermo Fisher Scientific	A-31556	1:300